IDEA League

Master of Science in Applied Geophysics

Research Thesis

Frequency-Domain Wideband Ground Penetrating Radar Modelling

using Finite Elements and Perfectly Matched Layers

Chaitanya Dinesh Singh

August 4, 2025

Frequency-Domain Wideband Ground Penetrating Radar Modelling

using Finite Elements and Perfectly Matched Layers

Master of Science Thesis

for the degree of Master of Science in Applied Geophysics at
Delft University of Technology
ETH Zürich
RWTH Aachen University
by

Chaitanya Dinesh Singh

August 4, 2025

Department of Geoscience & Engineering · Delft University of Technology
Institute of Geophysics · ETH Zürich
Faculty of Georesources and Materials Engineering · RWTH Aachen University

Printed in The Netherlands

IDEA LEAGUE
JOINT MASTER'S IN APPLIED GEOPHYSICS

Delft University of Technology, The Netherlands
ETH Zürich, Switzerland
RWTH Aachen, Germany

Dated: *August 4, 2025*

Supervisors:

Dr. Paula Rulff

Prof.dr.ir. E.C. Slob

Committee Members:

Dr. Paula Rulff

Prof.dr.ir. E.C. Slob

Dr. Cédric Schmelzbach

Abstract

In wideband Ground Penetrating Radar (GPR) forward modelling, a choice can be made between time and frequency domains. With time-domain approach, efficient modelling and testing with real-world cases has been done, especially through `gprMax`. With frequency-domain approach, however, this level of applicability has not been reached. To take a step in this direction, a 3D wideband-capable GPR forward simulation code has been developed.

A wealth of efficient discretization, modelling and inversion strategies exist that exploit the nuances of frequency-domain simulations to enable rapid solutions, that a time-domain approach is inherently not capable of using. Hence, the simulation code developed in this thesis, named `elfe3D_GPR`, aims to provide the means to implement and test these strategies as efficiently as possible. The development of this code is based on another open-source software, `elfe3D`, which is a 3D electromagnetic fields forward solver using edge-based finite elements developed for Controlled-Source Electromagnetism (CSEM) in Fortran. Its use of the `MUMPS` direct solver and adaptive refinement makes `elfe3D` a very strong starting point for the development of GPR simulation. Since CSEM solves for diffusive-field regime of electromagnetism, a few essential changes have been made in the boundary-value problem that `elfe3D_GPR` solves. Since the region of interest in GPR simulations is finite due to physical and computational constraints and due to the wave nature of GPR fields, appropriate absorbing boundary has also been implemented in `elfe3D_GPR` by the means of Perfectly Matched Layers (PML). The specific formulation of PML chosen is a Uniaxial-PML with an exact decay function, due to their excellent absorption performance of outgoing waves.

Once these changes were implemented in `elfe3D`, the new simulation code `elfe3D_GPR` has been extensively tested for synthetic layered and anomalous subsurface models, along with its potential for wide-band simulations. Validation has been performed against analytical solution for layered models, and the results from `empymod`. The results show promising applicability of `elfe3D_GPR` for generalized GPR forward problems, and should serve as a good basis for implementing the many frequency-domain specific modelling and inversion strategies that exist. As such, `elfe3D_GPR` is also kept open-source.

Acknowledgements

I would like to express sincerest gratitude to both of my supervisors, Prof.dr.ir. Evert Slob and Dr. Paula Rulff. Their unwavering support and guidance even in the most challenging times of my thesis has been the foundation on which I have been able to progress forward, even at times when I doubted myself. I highly appreciate their shared enthusiasm to pursue the scientific questions I have tackled, and their understanding of the subject. I thank them both for making my research experience so productive, enjoyable and insightful, while taking care of my well-being.

This research would be impossible without the unconditional love and incomparable support of my family. I am deeply grateful for them, their actions and words that have greatly shaped my world all throughout these years, and given me the chance to pursue the science that I love. The sacrifices you have made, the risks you have taken, I will never forget them.

To my dear friends, Rishi Pathak, Soham Kelkar and Janna Blaume, you have been so very instrumental to me throughout this thesis. Rishi, I cannot thank you enough for being the reason I started appreciating and understanding science as well as I do, and your selfless support in ensuring my well-being from a whole ocean afar. Soham, thank you for keeping me grounded with your refreshing perspectives and encouragement; they have brightened my days of challenging work. Janna, thank you for your incredible understanding, support and radiant enthusiasm, which have empowered me to stay focused on the many intricacies the thesis involved. To all my friends in this master's program, thank you for making me feel so welcomed and appreciated thousands of kilometres away from my home.

Finally, this work would not be possible without the many centuries of humanity's scientific pursuits. I thank the many scientists whose endless years of incredible work I have studied. I am much more grateful and appreciative of science now than I have ever been.

Delft University of Technology — Chaitanya

August 4, 2025

Table of Contents

List of Figures

List of Tables

Acronyms

GPR Ground Penetrating Radar

EM Electromagnetism / Electromagnetic

CSEM Controlled-Source Electromagnetism

PML Perfectly Matched Layers

FD Finite Differences

FE Finite Elements

FEM Finite Element Method

IE Integral Equations

1/2/3D One/Two/Three Dimensions

R.H.S. Right Hand Side

L.H.S. Left Hand Side

PDE Partial Differential Equation

BVP Boundary Value Problem

DBC Dirichlet Boundary Condition

PEC Perfect Electric Conductor

ABC Absorbing Boundary Condition

DOF Degrees of Freedom

TE Transverse Electric Mode

TM Transverse Magnetic Mode

U-PML Uniaxial PML

A-PML Anisotropic PML

SC-PML Stretched-Coordinate PML

CFS-PML Complex Frequency-Shifted PML

Chapter 1

Abstract

In wideband Ground Penetrating Radar (GPR) forward modelling, a choice can be made between time and frequency domains. With time-domain approach, efficient modelling and testing with real-world cases has been done, especially through `gprMax`. With frequency-domain approach, however, this level of applicability has not been reached. To take a step in this direction, a 3D wideband-capable GPR forward simulation code has been developed.

A wealth of efficient discretization, modelling and inversion strategies exist that exploit the nuances of frequency-domain simulations to enable rapid solutions, that a time-domain approach is inherently not capable of using. Hence, the simulation code developed in this thesis, named `elfe3D_GPR`, aims to provide the means to implement and test these strategies as efficiently as possible. The development of this code is based on another open-source software, `elfe3D`, which is a 3D electromagnetic fields forward solver using edge-based finite elements developed for Controlled-Source Electromagnetism (CSEM) in Fortran. Its use of the `MUMPS` direct solver and adaptive refinement makes `elfe3D` a very strong starting point for the development of GPR simulation. Since CSEM solves for diffusive-field regime of electromagnetism, a few essential changes have been made in the boundary-value problem that `elfe3D_GPR` solves. Since the region of interest in GPR simulations is finite due to physical and computational constraints and due to the wave nature of GPR fields, appropriate absorbing boundary has also been implemented in `elfe3D_GPR` by the means of Perfectly Matched Layers (PML). The specific formulation of PML chosen is a Uniaxial-PML with an exact decay function, due to their excellent absorption performance of outgoing waves.

Once these changes were implemented in `elfe3D`, the new simulation code `elfe3D_GPR` has been extensively tested for synthetic layered and anomalous subsurface models, along with its potential for wide-band simulations. Validation has been performed against analytical solution for layered models, and the results from `empymod`. The results show promising applicability of `elfe3D_GPR` for generalized GPR forward problems, and should serve as a good basis for implementing the many frequency-domain specific modelling and inversion strategies that exist. As such, `elfe3D_GPR` is also kept open-source.

Chapter 2

Introduction

2-1 Historic Overview

The Ground Penetrating Radar Imaging Method

Ground Penetrating Radar (GPR) is one of the key methods used for near-surface geophysical imaging (Annan, 2002, 2005; Benedetto et al., 2016; Forte & Pipan, 2017; Lombardi et al., 2022). It operates by transmitting radar frequency electromagnetic (EM) waves into the ground and recording its response to infer details about the subsurface structure (Annan, 2005). These antennas usually work in the radio wave regime - for a GPR application that is between 10 MHz and 2.5 GHz (Annan, 2005; Lombardi et al., 2022). This frequency range has been empirically established due to the nature of media and environments that GPR can be applied to, and its signal characteristics such as velocity of GPR wave, attenuation and impedance of materials it encounters (Annan, 2005). This range of frequencies has allowed GPR to be applied to many applications, such as geology, planetary science, civil engineering, archaeology, agriculture, glaciology, among others (Benedetto et al., 2016; Lombardi et al., 2022).

Simulating Electromagnetic Fields

Electromagnetic waves behave in complicated ways to media they encounter in their path of propagation (Griffiths, 2023). For GPR applications, where the subsurface consists of numerous different materials, each having a unique set of electric properties, it can easily become challenging to understand what the recorded Earth's response is informing us. Specifically, the electric permittivity ε and the electrical conductivity σ are the material properties influencing the GPR responses. The magnetic permeability μ does also affect EM wave propagation, however, there are usually no significant variations in it for geophysical media surveyed by GPR (Annan, 2005).

To ease inference efforts, computer simulation programmes have been written to evaluate how various geophysical media, or a combination thereof, respond to a multitude of GPR survey

configurations in two or three dimensions (Ding et al., 2025; Huber & Hans, 2018; Irving & Knight, 2006; Warren, Giannopoulos, & Giannakis, 2016). These programmes are built on a foundation of forward solvers - a family of computational algorithms that solve a system of equations for the solution of a mathematical formulation of one or more physical phenomena. They operate on a given discretized geometry corresponding to a region of interest, using the material properties and their variations throughout the geometry, and any other information that is known/required for the solution. For GPR, the forward solvers are built to evaluate solution of the EM wave equation that is derived from the Maxwell's equations (Ding et al., 2025; Irving & Knight, 2006; Warren, Giannopoulos, & Giannakis, 2016), or they could simplify the process based on assumptions to the wave propagation (Huber & Hans, 2018). Naturally, the region of interest for GPR simulations include the volume of subsurface whose GPR response needs to be understood.

There exist multiple approaches to forward simulations of wave problems, which can be majorly classified into locally-supported and globally-supported methods (Atkinson & Han, 2005). This distinction arises from the way the simulation domain and governing physical system operator are discretized. Locally-supported methods such as Finite Differences (FD) (Cassidy & Millington, 2009; Davidson & Botha, 2007; Lampe et al., 2003; Sadiku, 2009; Taflove, 1995; Warren, Pajewski, et al., 2016; Warren, Giannopoulos, & Giannakis, 2016) and Finite Elements (FE) (Butler & Zhang, 2016; F. Cui et al., 2023; Jin, 2015; Jin & Riley, 2008; Liu et al., 2019; Pelosi et al., 2009; Zarei et al., 2016) formulate their system operator with a confined local dependence of an element on its immediate neighbors. Conversely, globally-supported methods such as Integral Equations (IE) (W. Chew & Tong, 2022; Davidson & Botha, 2007; Peng et al., 2011; Sadiku, 2009; Šušnjara et al., 2016; Van den Berg, 2021; Warren, Pajewski, et al., 2016) formulate its system operator where each element of simulation domain depends on every other element in the domain. Hybrid methods that combine these principles also exist (Casati et al., 2020).

Each of these methods has its own set of use cases and limitations. Due to global support in IE methods, the system matrix is dense. However, Green's function evaluations based on homogeneous background and scattering sources in the subsurface allow fast EM field solutions using iterative solvers (Peng et al., 2011; Warren, Pajewski, et al., 2016). Local-support approaches have a large null-space in frequency domain that makes it difficult to use iterative solvers for them. However, FD approach is the most physically direct translation of Maxwell's equations (Cassidy & Millington, 2009; Lampe et al., 2003) and FE approach recasts the Maxwell's equations into a variational form and can account for incredible complexities in media with ease (F. Cui et al., 2023; Liu et al., 2019). Due to local support, their system matrix is sparse allowing for unique solving strategies (Atkinson & Han, 2005; Sadiku, 2009).

Finite Elements in Frequency and Time Domains

Each of these approaches can work in time or frequency domain. To go from one domain to another, the Partial Differential Equation (PDE) of wave equation needs only to be changed using the time-frequency duality. This simply requires replacing the PDE terms consisting of the partial derivative of time ($\frac{\partial}{\partial t}(\cdot)$) with $\pm j\omega$, or vice versa. t is time in SI unit $[s]$, $j = \sqrt{-1}$ is the imaginary unit, ω is angular frequency with unit $[rad/s]$, and the sign depends on the complex phasor convention for time dependence used for simulation. Despite this simple

change in the PDE itself, there are significant differences to each domain when implementing the program and interpreting simulation results.

Time domain GPR simulations are bounded by a time stepping limit that depends on how fast the EM waves are expected to propagate, known as the Courant-Friedrich-Levy stability criteria (Courant et al., 1928; Davidson, 2010). Moreover, to account for high-order time-varying effects, time integration schemes like Runge-Kutta, Cranck-Nicholson and others increase the computational requirements of simulations (Gottlieb & Ketcheson, 2016). These constraints are absent in frequency domain simulations, where one simulation solves for a singular frequency of the source. To account for the complete bandwidth of the radar sources would involve multiple such simulations at frequencies of key interest, whose results are then taken together as per inference requirements (Feng et al., 2020; Lavoué et al., 2014).

Implications of Time and Frequency-Domain Simulations for Wideband GPR

For wideband GPR, time-domain forward simulations have been conventionally more favoured, especially with the arrival and open-source development of `gprMax` (Warren, Giannopoulos, & Giannakis, 2016). Using FD in time-domain (FDTD), it allows computation of GPR wave fields with several broadband sources. These have such a large frequency range that they require numerous frequency-domain simulations to cover the complete bandwidth. In contrast, one FDTD simulation can model the entire spectrum, provided that the time-stepping scheme and the spatial and temporal discretization are sufficiently fine to resolve the shortest wavelength present in the signal. This does imply requiring much smaller time steps compared to the requirement according to sampling theory (Mulder et al., 2008). However, with extensive research and efficient programming of forward solver kernels, `gprMax` has made these wideband simulations in time-domain very efficient.

Nevertheless, there are many reasons to perform wideband simulations in frequency-domain. A geological region of interest can be sampled with varying spatial discretization according to frequencies of interest. This allows coarse discretization for low frequencies (Jin & Riley, 2008). On the opposite end of the spectrum, high frequencies have lower penetration depth and smaller fresnel zones (Annan, 2005). Hence, in both ends of the spectrum, different efficient meshing strategies can be performed, which cannot be implemented in time-domain. Moreover, simulations per each frequency can be done in parallel without requiring information transfer between them (Jin & Riley, 2008). In addition, a robust frequency interpolation algorithm and reduced-order modelling (Jin & Riley, 2008) would make wideband simulations in frequency-domain much more efficient and practical.

Another significant reason for choosing frequency domain forward simulations lies in the fact that they offer the possibility to apply smart inversion strategies (Feng, Wang, & Zhang, 2019; Feng et al., 2020; Lavoué et al., 2014; Sun et al., 2017). Of a wideband GPR source, not all frequencies have significant information of subsurface structure and materials, owing to their frequency-independent behavior (Annan, 2005). Using spectral analysis, inversions can be made much quicker by selecting few frequencies of high interest (Feng et al., 2020; Lavoué et al., 2014). Otherwise, multi-scale inversions exist, which use low frequency information first with coarse meshing to obtain preliminary qualitative information of regions of interest (Feng, Wang, & Zhang, 2019), after which the higher frequency data can be inverted. All of these strategies utilize the frequency-domain behavior of GPR responses effectively, making

it quite an attractive endeavour to pursue wideband forward GPR simulations in frequency domain.

2-2 Problem Statement and Research Questions

To use all aforementioned frequency-domain specific wideband GPR modelling and inversion strategies, a high-performing wave-regime EM forward solver is needed. It should be able to simulate complex subsurface model responses with high accuracy. Achieving this with optimal computational cost requires several aspects of simulation to be studied, implemented as computer code, and tested against reference solutions. Some of these aspects include: choosing a discretization approach, converting the physical problem to a system of linear equations that are suited for the approach, handling element-wise, material and truncation boundaries of the simulation model, establishing meshing constraints, and so on. How is EM wave propagation accurately modelled in a finite simulated geophysical model? What comprises an efficient discretization and truncation strategy for the GPR forward problem using first-order edge-based FEM with an unstructured mesh? What are the modelling constraints for a wide-band frequency-domain simulation? These are some of the questions I have attempted to address in this thesis.

2-3 Proposed Method of Solution and Objectives

In my thesis, I aim to develop a frequency-domain wideband-capable EM wave equation forward solver using FE in 3D. The goal is to achieve a powerful combination of the benefits of frequency-domain simulations with the ability to model complex geophysical media using 3D FE and unstructured meshing. Moreover, the resulting software is aimed to be a strong candidate for unique inversion strategies, as discussed previously.

The development for the program presented in this thesis has not been from scratch. I have worked with `elfe3D` (Rulff, 2023; Rulff et al., 2021), which is an open-source 3D FE software for low-frequency EM applications in geophysics, specifically for Controlled-Source EM (CSEM). It is written in Fortran, which takes unstructured mesh input generated by `tetgen` (Si & TetGen, 2009), solves the FE system via the parallel sparse direct solver `MUMPS` (Amestoy et al., 2000), and supports adaptive refinement and parallelization using `OpenMP`. I used this open-source code as the basis of 3D FE frequency domain simulation framework, and modified and extended parts of it to make it work for GPR simulations. I call this new program `elfe3D_GPR`, which will also be open-source. Completing this solver would not be possible without implementing an absorbing boundary, for which Perfectly Matched Layers (PML) has also been implemented and tested.

This aspect of modifying an existing low-frequency EM code to high-frequency EM is also a part of the motivation to choose to work with `elfe3D` as the basis for numerical implementation. It could provide unique insights into the differences in solving for both regimes of EM, or validate known ones.

2-4 Outline of the Thesis

This thesis is organized into chapters pertaining to specific theory and numerical aspects that I have studied and implemented. Chapter 3 discusses the forward problem in both CSEM and GPR applications, FE framework and the specific implementation in `elfe3D`, as well as the theory and development of PML. Chapter 4 covers the complete methodology that was used over the course of this project that has led to the current version of `elfe3D_GPR`. Chapter 5 presents all key tests of `elfe3D_GPR`, their results, and a discussion on capabilities of the software that can be inferred from these results. Chapter 6 concludes my work and presents future directions this line of research and scientific code development can lead to.

Chapter 3

Theory of Electromagnetic Fields and the Finite Element Method

3-1 Diffusive and Wave Regimes of Electromagnetic Fields

James Clerk Maxwell presented the complete mathematical theory of EM in his most widely known work, *"A Treatise on Electricity and Magnetism"*, in 1873 (Maxwell, 1873). Here, he presented systematically all important electromagnetic quantities and their relation to each other, in a set of 20 equations, amongst other topics. The compact vector form of these equations that we know now was worked out by Oliver Heaviside in his influential set of books, "*Electromagnetic Theory*" (Heaviside, 1893–1912). In the time-harmonic form with a complex phasor notation of $e^{+j\omega t}$, these equations are expressed in terms of the Electric and Magnetic fields ($\mathbf{E}$ of unit $[V/m]$ and $\mathbf{H}$ of unit $[A/m]$ respectively) as (Balanis, 2012):

$$\nabla \times \mathbf{E} = -j\omega\mu\mathbf{H}, \tag{3-1a}$$

$$\nabla \times \mathbf{H} = \left(\frac{1}{\rho} + j\omega\varepsilon\right)\mathbf{E} + \mathbf{J}_p, \tag{3-1b}$$

$$\nabla \cdot (\varepsilon\mathbf{E}) = q, \tag{3-1c}$$

$$\nabla \cdot (\mu\mathbf{H}) = 0, \tag{3-1d}$$

Here, μ is the magnetic permeability $[H/m]$, ε is the electric permittivity $[F/m]$, ρ is the electrical resistivity $[\Omega m]$, $\mathbf{J}_p$ is the impressed (source) current density $[A/m^2]$, and q is the volume electric charge density $[C/m^3]$ related to $\mathbf{J}_p$ by the continuity equation (Equation (3-2)).

The Right-Hand-Side (R.H.S.) of Ampere's Law (Equation (3-1b)) can be re-written as a sum of total current density in the field, namely, the displacement current density $\mathbf{J}_d = j\omega\varepsilon\mathbf{E}$, the conduction current density $\mathbf{J}_c = \frac{1}{\rho}\mathbf{E}$, and the source polarization current $\mathbf{J}_p$. The

electric charge density q is related to the conduction and polarization current densities by the continuity equation:

$$\nabla \cdot (\mathbf{J}_c + \mathbf{J}_p) = -j\omega q. \tag{3-2}$$

3-1-1 Boundary Value Problems for Electromagnetism

To solve the Maxwell's equations in complex media using FE in frequency domain, the forward problem is expressed in terms of a Boundary Value Problem (BVP) (Jin, 2015). BVPs arise when a physical system is described by a differential equation over a spatial domain Ω, subject to conditions specified on the boundary Γ of the domain. The general form of the differential equation of a BVP can be written as:

$$\mathcal{L}\phi = f \quad \text{in } \Omega. \tag{3-3}$$

Here, $\mathcal{L}$ is a linear operator consisting of derivatives and medium parameters of the system that acts on the unknown field variable ϕ, and f is a known source function. Equation (3-3) needs to be accompanied by a set of boundary conditions on Γ, along material interfaces and between the discretized elements of the simulation domain to complete the BVP. These conditions are useful to explicitly constrain how the field values are evaluated within the limits of finite truncation and finite points of evaluations in a computer, both of which do not exist in physical space. BVPs have long been established before the rise of computation by (d'Alembert, 1747) and Euler between 1747-1750. Since then, they are thoroughly researched for FE computation of EM problems (Monk, 2003; Silvester & Ferrari, 1996).

3-1-2 The CSEM Boundary Value Problem

For CSEM problems, as in `elfe3D` (Rulff, 2023), the BVP is derived from Maxwell's equations Equation (3-1) to express the problem entirely in terms of the electric field $\mathbf{E}$. This leads to a second-order partial differential equation known as the curl-curl equation solved in the simulation domain Ω. It is accompanied with a homogeneous Dirichlet Boundary Condition (DBC) on the simulation boundary Γ. Explicitly, the BVP used in `elfe3D` is:

$$\nabla \times \left(\frac{1}{\mu}\nabla \times \mathbf{E}\right) + j\omega\frac{1}{\rho}\mathbf{E} - \omega^2\varepsilon\mathbf{E} = -j\omega\mathbf{J}_p \quad \text{in } \Omega, \tag{3-4a}$$

$$\hat{\mathbf{n}} \times \mathbf{E} = 0 \quad \text{on } \Gamma, \tag{3-4b}$$

where $\hat{\mathbf{n}}$ represents the vector normal to the boundary Γ. In open space configurations, Γ is located at infinity with a radiation condition applied to it (Monk, 2003). However, in geophysical simulations with a limited region of interest, Γ is always a finite distance away from the source. Physically, Equation (3-4b) models a Perfect Electric Conductor (PEC) on the boundary of the domain of simulation (Griffiths, 2023), which ensures that all energy of the field stays in the domain. For geophysical EM problems where layers of different media exist with varying electromagnetic parameters, the continuity of the field components at interfaces

between these media also arise from the Maxwell's equations Equation (3-1). Specifically for the electric field, its tangential component must be continuous across the interface (Griffiths, 2023). This is represented by:

$$\hat{\mathbf{n}} \times (\mathbf{E}^+ - \mathbf{E}^-) = 0, \tag{3-5}$$

where the electric field right above the interface is represented by $\mathbf{E}^+$ and the electric field right below the interface is represented by $\mathbf{E}^-$, and the $\hat{\mathbf{n}}$ here represents the vector normal to the interface between the media. The normal component of the electric experiences a jump discontinuity, arising from Equation (3-1c), according to the relation:

$$\hat{\mathbf{n}} \cdot \left(\left(\frac{1}{\rho^+} + j\omega\varepsilon^+ \right) \mathbf{E}^+ - \left(\frac{1}{\rho^-} + j\omega\varepsilon^- \right) \mathbf{E}^- \right) = 0, \tag{3-6}$$

where, similar to the electric field representations, ε^+, ρ^+ represents electric permittivity and electrical resistivity right above the interface respectively, and ε^-, ρ^- represent the same material parameters right below the interface. The R.H.S. here is usually zero for the subsurface models that do not have free charges. This implies that the material interfaces are source-free.

The continuity condition of tangential electric field (Equation (3-5)) and the discontinuity in the normal electric field (Equation (3-6)) complete the description of the physical BVP of CSEM. After solving it over the domain to find the electric field distribution, the magnetic field information is extracted using Faraday's Law (Equation (3-1a)) on the electric field data at the receiver sites (Rulff, 2023), giving a complete set of measurement information.

3-1-3 Physical Considerations with CSEM

For the low frequency regime of CSEM methods, it is evident that the displacement currents-based term in the curl-curl equation ($\omega^2\varepsilon\mathbf{E}$) does not contribute to the solution of the BVP due to second-order frequency scaling to the field. Hence, this term is dropped in CSEM simulations (Ren et al., 2013; Rulff et al., 2021). This resulting PDE describes the diffusive behavior of EM fields. (Zhdanov, 2009) states that it closely resembles Fick's equation that describes diffusion of chemical species, which has given it the name of diffusion equation of EM.

It is important to note that diffusive field EM has a non-trivial attenuation factor determined by the skin depth with units [m]. At one skin depth below the subsurface, the field strength decays to $1/e \approx 0.367879$ times the field strength at the surface, and this decay repeats with multiples of skin depth till the field strength approaches zero (Zhdanov, 2009). In diffusive-field regime for non-magnetic Earth, the skin depth is approximated by the following expression:

$$\delta_e \approx 503.3\sqrt{\frac{\rho}{f}}, \tag{3-7}$$

where f is the frequency of the field emitted by the source. This parameter is useful to determine how large a CSEM simulation and/or survey domain needs to be before the natural attenuation in the subsurface medium makes the field decay to negligible values, where the domain can be truncated by the simple boundary condition (Equation (3-4b)). It also

highlights the effect of source frequency, where lower frequencies will have a larger depth of penetration and lower conductivity makes fields attenuate less.

The transition from diffusive-field behavior to wave-field behavior occurs when the displacement current contributions dominate the conduction current contributions to the field. Hence, it is determined by the ratio of $\sigma/\omega\varepsilon$ (Annan, 2005). When it is much higher than one, the field is diffusive, and when it is much lower than one, the EM field is a wave-field. As such, a transition frequency f_t can be determined for any media which indicates where the field shifts from one regime to another (Section 3-1-3).

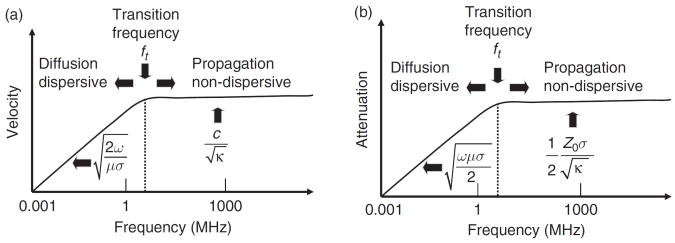

Figure 3-1: Velocity and attenuation curves over a range of frequencies, showing the transition frequency between diffusive and wave behavior.

Here, c is the speed of light, Z_0 is the electromagnetic impedance of free space, and κ is the dielectric constant of the medium, equal to relative permittivity $\kappa = \varepsilon_r = \varepsilon/\varepsilon_0$. From this figure, it is apparent that the velocity and attenuation become frequency-independent after crossing the f_t, which is a characteristic of wave propagation. The wavenumber and impedance are explained in the next section, as they are wave-regime quantities pertaining to GPR.

3-1-4 The Wave Regime Boundary Value Problem for GPR

From Section 3-1-3, it is evident that when the frequency of the source used for EM geophysical imaging exceeds that of f_t, the EM field starts behaving like a wave. This is the domain of GPR surveys, where the displacement current term $\omega^2\varepsilon\mathbf{E}$ dominates the EM-field behavior. For implementing GPR simulation in `elfe3D_GPR`, I have defined two complex parameters: effective permittivity ε_{eff} and wavenumber k. The effective permittivity is a material parameter defined by (Annan, 2005; Ding et al., 2025).:

$$\varepsilon_{\text{eff}} = \varepsilon - j\frac{\sigma}{\omega}, \tag{3-8}$$

The wavenumber is defined by $k = \omega\sqrt{\mu\varepsilon_{\text{eff}}}$ with SI units of [rad/m]. Its real component represents spatial frequency of a wave and is inversely proportional to its wavelength, while its imaginary component is proportional to the attenuation of a wave in a medium. For free space, the wavenumber evaluates to $k_0 = \omega\sqrt{\mu_0\varepsilon_0}$, where, μ_0 and ε_0 are the magnetic permeability and electrical permittivity of free space, respectively. For other media, relative material parameters are introduced, namely μ_r which is the relative magnetic permeability and $\varepsilon_{r,\text{eff}}$ which is the relative effective electric permittivity These are related to the corresponding true values of parameters by relations $\varepsilon_{\text{eff}} = \varepsilon_{r,\text{eff}}\varepsilon_0$, $\mu = \mu_r\mu_0$. Similarly, the wavenumber k can

be re-written as:

$$k = k_0\sqrt{\mu_r\varepsilon_{r,\text{eff}}} \tag{3-9}$$

$$= k_0\sqrt{\mu_r\left(\varepsilon_r - j\frac{\sigma}{\omega\varepsilon_0}\right)}. \tag{3-10}$$

Re-writing the curl-curl equation using wavenumber and effective permittivity, the BVP Equation (3-4) changes to:

$$\nabla\times\left(\frac{1}{\mu_r}\nabla\times\mathbf{E}\right) - k_0^2\varepsilon_{r,\text{eff}}\mathbf{E} = -jk_0Z_0\mathbf{J}_p \quad \text{in } \Omega, \tag{3-11a}$$

$$\hat{\mathbf{n}}\times\mathbf{E} = 0 \quad \text{on } \Gamma, \tag{3-11b}$$

where Z_0 is the impedance of free space given by $Z_0 = \sqrt{\frac{\mu_0}{\varepsilon_0}} \approx 377\Omega$, and the other terms hold the same meaning as before. Here, again, the interface conditions Equations (3-5) and (3-6) hold.

Unbounded Radiation of Wave Phenomena

In unbounded free-space, EM fields travel to infinity (Griffiths, 2023). Physically, this can be expressed as the Sommerfeld radiation condition (Jin & Riley, 2008; Monk, 2003). However, for computations within a finite region of interest, this needs careful consideration, as the homogeneous DBC applied as the boundary (Equations (3-4b) and (3-11b)) can make the field reflect from it.

For low-frequency geophysical simulations with finite space, a simple approach is to place the computational boundary sufficiently far from the source, dictated by the skin depth. After the field travels multiples of skin depths, it will effectively have zero strength, making a simple homogeneous Dirichlet BC sufficient (Zhdanov, 2009). This is also the approach with `elfe3D` (Rulff, 2023).

For computation of GPR fields in a finite region of interest, however, artificial absorption of outgoing field needs to be enforced. This is a long-researched problem for all types of wave problems. Absorbing boundary conditions (ABCs) have been implemented for domain truncation for wave problems since 1977 (Engquist & Majda, 1977). There are several ways to implement them, as given in (Jin & Riley, 2008; Monk, 2003). The most successful type of absorbing boundary is a finite-thickness artificial absorber appropriately called Perfectly Matched Layers (PML), introduced by Jean-Pierre Bérenger (Berenger, 1994). The subject of PML and their implementation has been one of the major themes of my thesis. As such, I have discussed them in complete detail in Section 3-3.

3-2 Finite Elements for Simulating Wideband GPR in Frequency-Domain

The finite element method (FEM) is one of the leading numerical methods to solve BVPs by locally-supported approximation of the unknown field (Jin, 2015). The method gets its

name from its characteristic representation of the domain of solution with a set of smaller subdomains called the finite elements. There are various approaches to convert a PDE into a linear discrete matrix-vector problem that all use different versions of FE spatial discretization, such as the Ritz method, the Galerkin method, the Discontinuous Galerkin method, etc. (Jin, 2015; Monk, 2003; Silvester & Ferrari, 1996). These methods can be classified into *variational* and *weighted residual* approaches, or combinations and derivatives from them. Depending on the physical phenomena, one method would be more tractable and efficient than the other. The derivation and analysis of the FEM framework for EM fields is covered extensively in (Hiptmair, 2002; Jin, 2015; Langer et al., 2019; Monk, 2003; Silvester & Ferrari, 1996). For `elfe3D` and hence for `elfe3D_GPR`, the main reference for the FE framework has been the work by (Jin, 2015), from which the weighted residual approach of the Galerkin method has been implemented.

3-2-1 The FEM Framework

The FEM framework for EM wave problems typically consists of the following steps:

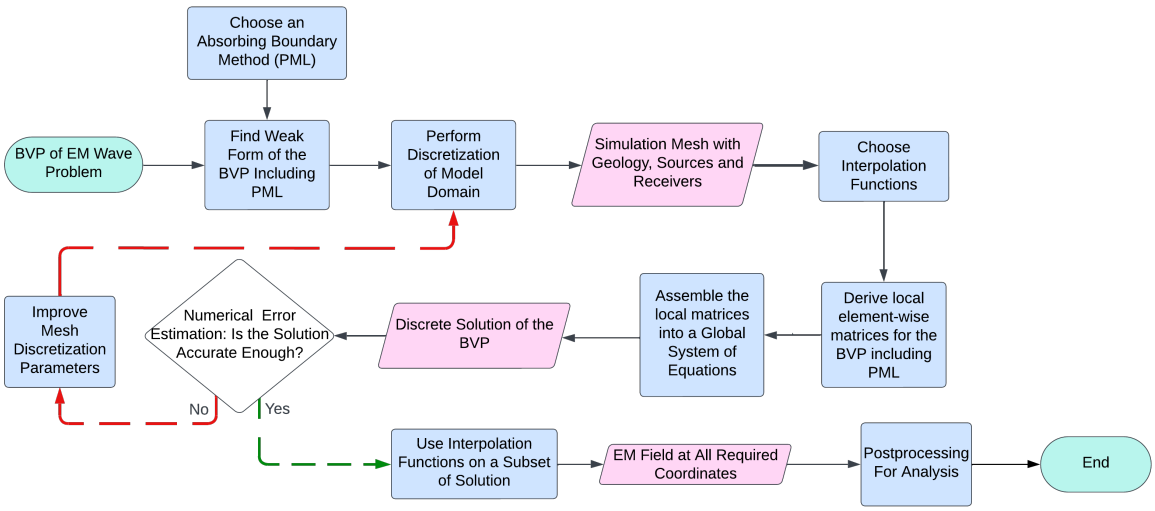

Figure 3-2: The general FEM framework for EM wave problems with adaptive refinement using error estimation from a dedicated numerical approach or comparison with a reference solution.

I will now briefly mention these steps for EM wave simulation for GPR.

Find the Weak Form of the BVP

To allow continuously defined BVPs such as Equations (3-4) and (3-11), referred as "strong-form" problems, to be evaluated over a discretized truncated simulation domain, a "weak" form of the BVP must be determined (Monk, 2003). This need arises from the fact that the curl-curl terms in the strong forms require solutions to have sufficiently smooth second derivatives. Such smooth field solutions are difficult to estimate for non-trivial EM problems,

if they exist, since the discretization creates numerous inter-element boundaries. Hence, the strong-form PDE is weakened such that its solution regularity requirements are more relaxed to conform to the piecewise description of the computational domain including the boundary.

To obtain the weak form of the GPR BVP Equation (3-11), a test vector-valued function $\mathbf{v}$, is multiplied to the governing PDE, and the resulting equation is integrated by parts formally over the computational domain Ω (Jin, 2015; Rulff et al., 2021). Using the Galerkin approximation, which is characteristic of the Galerkin method, both $\mathbf{v}$ and $\mathbf{E}$ belong to the same locally-supported Sobolev space. For the total field formulation of Maxwell's Equations (or wave equation for GPR), the Sobolev space is $\mathcal{H}^0(\text{curl}, \Omega)$ (Monk, 2003). It is defined as:

$$\mathcal{H}^0(\text{curl}, \Omega) := \{u \in \mathcal{H}(\text{curl}, \Omega) \mid \hat{n} \times u = 0 \text{ on } \Gamma\}, \tag{3-12}$$

where,

$$\mathcal{H}(\text{curl}, \Omega) := \left\{u \in [\mathcal{L}^2(\Omega)]^3 \;\middle|\; \nabla \times u \in [\mathcal{L}^2(\Omega)]^3\right\}. \tag{3-13}$$

Here, $\mathcal{L}^2(\Omega)$ represents the Hilbert vector space of square-integrable functions with defined integral L^2-norms for volumes and surfaces:

$$\|\mathbf{v}\|_{L^2,\Omega} = \sqrt{\iiint_\Omega \|\mathbf{v}\|_2^2 \, dV} \quad \text{and} \quad \|\mathbf{v}\|_{L^2,\Gamma} = \sqrt{\iint_\Gamma \|\mathbf{v}\|_2^2 \, dS}, \tag{3-14}$$

where $\|\mathbf{v}\|_2$ denotes the standard Euclidean norm of the vector field.

Now, I can write the complete weak form for the EM wave-regime BVP Equation (3-11) as: Find $\mathbf{E} \in \mathcal{H}^0(\text{curl}, \Omega)$ such that

$$\iiint_{\Omega_{\text{model}}} \frac{1}{\mu_r}(\nabla\times\mathbf{v})\cdot(\nabla\times\mathbf{E})\,\mathrm{d}V - \iint_{\Gamma_{\text{model}}} \frac{1}{\mu_r}(\mathbf{v}\times\nabla\times\mathbf{E})\cdot\hat{\mathbf{n}}\,\mathrm{d}S - k_0^2 \iiint_{\Omega_{\text{model}}} \varepsilon_{r,\text{eff}}\,\mathbf{v}\cdot\mathbf{E}\,\mathrm{d}V = -jk_0Z_0 \iiint_{\Omega_{\text{model}}} \mathbf{v}\cdot\mathbf{J}_s\,\mathrm{d}V, \tag{3-15}$$

$\forall\ \mathbf{v} \in \mathcal{H}^0(\text{curl}, \Omega)$, and satisfying the boundary condition Equation (3-11b) as well as the continuity constraints Equations (3-5) and (3-6).

This solution is sought for using the FE discretization strategy described below.

Discretize the Domain Using Finite Elements

With FEM, a region of interest bounding the physical system is divided into multiple small parts, referred to as elements. Depending on dimensions of simulation and modelling requirements, different elements are used for discretization. Even in the field of EM, a lot of variety exists (Demkowicz, 2006; Jin, 2015).

To highlight the vast variety that is possible with discretization used in FEM, I now mention the characteristics that the discretized elements posses in three dimensions:

1. **Points of an Element (Nodes)**: Each element requires a definition of coordinates of its vertices. These are the nodes of an element. Since the mesh usually consists of a set of connected elements, it is natural that a significant number of nodes are shared between elements. An element can also have more nodes than just at its vertices (Demkowicz, 2006). These are higher-order elements.

2. **Line Segments of an Element (Edges)**: Edges connect the nodes of various elements. These edges are usually shared between different elements. These should be defined such that the original geometry of the input domain is preserved. For geophysical regions, this becomes essential for describing layers of subsurface, boundaries of anomalous bodies, faces of the domain and faces of the same element, etc.

3. **Faces of an Element (Surface Area)**: Connecting the edges in a way that makes the mesh elements closely resemble a sphere as well as adhere to the material boundaries is an important factor in discretization. Faces are also interconnected between elements, which affect how the simulation system matrix is assembled. Neighbouring faces enforce boundary or interface conditions between different media and between each element, and help account for how the source field propagates through the region of interest.

4. **Volume of an Element**: Based on how the faces are defined, different 3D shapes can be used for meshing. Some classical FE shapes include triangles and quadrilaterals in 2D, tetrahedra and cuboids in 3D. Their volume is a very important parameter that defines how fine or coarse a mesh is. Different physical phenomena have different constraints that their FE mesh should satisfy. I will illustrate this in more detail in Chapter 5.

In fact, FEM modelling codes usually benefit from employing dedicated meshing software that specifically handle the discretization of a simulation region. This becomes essential especially with complex geometry or accuracy requirements, that require special algorithms based on computational geometry to calculate precise placement, size, and other aspects of these elements. FEM accuracy depends heavily on the mesh characteristics it is used on (Jin, 2015), which has also been quite apparent during the progress of this thesis.

In reasoning so, `elfe3D`, and hence, `elfe3D_GPR` depends on discretized region input from the `tetgen` software composed of tetrahedra. It uses input information of the geophysical simulation region, and outputs a set of mesh files that contains all essential information about the discretized simulation domain.

Choose Proper Interpolation Functions

Once the simulation domain is adequately discretized, the weak form is made discrete by approximating the solution $\mathbf{E}$ and test $\mathbf{v}$ vectors by utilizing a set of interpolation functions. Also referred as shape or basis functions, these interpolation functions are defined per element of the mesh (Polycarpou, 2022). Using the information from element geometry, they define a smooth continuous function within the element. Depending on the function order, element geometry, and type of BVP, a set of coefficients are assigned to each element (Jin, 2015). Per element, the number of coefficients is referred to as the degrees of freedom (DOF). When these coefficients are multiplied with the interpolation function value, at any coordinate, it gives the value of the unknown vector field $\mathbf{E}$. Hence, the continuum solution can be approximated as according to the weak form and the order of basis functions. Mathematically, in the domain Ω that has been discretized into M finite elements, each element $m \in \{1, 2, \ldots, M\}$ has d associated DOFs. The solution vector field $\mathbf{E}$ is now approximated, for each element via shape functions using edge-based vector elements as:

$$\tilde{\mathbf{E}}^m(x,y,z) = \sum_{j=1}^{d} \mathbf{N}_j^m(x,y,z) E_j^m. \tag{3-16}$$

Here, $\tilde{\mathbf{E}}^m$ denotes the FE approximation of the solution vector at any point (x,y,z) in 3D space. The functions $\mathbf{N}_j^m(x,y,z) \in \mathbb{R}^3$ are vector-valued edge-based shape functions, and the coefficients $E_j^m \in \mathbb{R}$ are scalar DOFs assigned to each edge of a tetrahedral element.

For clarity, equation (3-16) can be re-written in matrix-vector form as:

$$\begin{bmatrix} \tilde{E}_x^m(x,y,z) \\ \tilde{E}_y^m(x,y,z) \\ \tilde{E}_z^m(x,y,z) \end{bmatrix} = \begin{bmatrix} \mathbf{N}_1^m(x,y,z) & \mathbf{N}_2^m(x,y,z) & \cdots & \mathbf{N}_d^m(x,y,z) \end{bmatrix} \begin{bmatrix} E_1^m \\ E_2^m \\ \vdots \\ E_d^m \end{bmatrix}, \tag{3-17}$$

which highlights how using higher-order elements can improve the accuracy of the approximated field. Higher order of elements will have more coefficients per element and hence associated number of shape functions, making the solution capable of capturing higher order variations in the field with greater accuracy. With `elfe3D`, as in many other FEM codes using tetrahedral elements (open-source (Anderson et al., 2021; Arndt et al., 2019) and commercial (ANSYS, Inc., 2025; COMSOL AB, 2024; Dassault Systèmes, 2023)), first-order shape functions work well with correspondingly small elements to account for these field variations with sufficient accuracy.

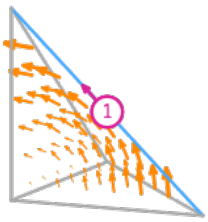

Figure 3-3: Vector field of the first-order edge-based Nédélec basis function associated with the marked edge (1).

The edge-based first-order Nédélec basis functions have been used in both `elfe3D`, `elfe3D_GPR`, which are explicitly defined for tetrahedral elements by (Jin, 2015). These basis functions are locally-supported, and designed to be constrained in $\mathcal{H}^0(\text{curl}, \Omega)$ space and comply to the continuity of tangential electric field components Equation (3-5). They are defined by finding piecewise polynomials that lie in $\mathcal{H}^0(\text{curl}, \Omega)$, extracting an even smaller subset of functions possible in the solution space that satisfy the BVP. The vector field associated with one edge is illustrated in Figure 3-3 (Scroggs et al., 2025). Similar vector fields are defined for all six edges of the tetrahedra. Mathematically, they are defined by:

$$\mathbf{N}_i^e = L_{i_1}^e \nabla L_{i_2}^e - L_{i_2}^e \nabla L_{i_1}^e l_i^e. \tag{3-18}$$

Here, subscripts i_1 and i_2 are the two end points of an edge i and element e. $L^e_{i_1}$ is a term based on linear Lagrange polynomial defined on the i_1^{th} node belonging to the i^{th} edge, and $L^e_{i_2}$ is a term based on linear Lagrange polynomial defined on the i_2^{th} node belonging to the i^{th} edge, and l^e_i is the length of the edge. Component-wise, the basis functions are defined as:

$$\mathbf{N}^e_i = \begin{pmatrix} \left(L^e_{i_1} \dfrac{\partial}{\partial x} L^e_{i_2} - L^e_{i_2} \dfrac{\partial}{\partial x} L^e_{i_1} \right) l^e_i \\ \left(L^e_{i_1} \dfrac{\partial}{\partial y} L^e_{i_2} - L^e_{i_2} \dfrac{\partial}{\partial y} L^e_{i_1} \right) l^e_i \\ \left(L^e_{i_1} \dfrac{\partial}{\partial z} L^e_{i_2} - L^e_{i_2} \dfrac{\partial}{\partial z} L^e_{i_1} \right) l^e_i \end{pmatrix} \tag{3-19}$$

Upon applying the basis functions to the weak form, it has become discrete, which now allows defining it in terms of a matrix-vector linear system of equations.

Obtain Local Element-Wise Matrices

All integrals in Equation (3-15) will be evaluated over all elements in the simulation domain. Since $\mathbf{v}, \mathbf{E} \in \mathcal{H}^0(\text{curl}, \Omega)$, the boundary integral term in Equation (3-15) vanishes on Γ. Moreover, between each element of the discretized mesh, due to the tangential continuity of the electric field (Equation (3-5)), the boundary integral term also vanishes throughout the domain. The other two terms in the Left-Hand-Side (L.H.S.) of Equation (3-15) and the R.H.S are evaluated per element. To approximate their values, the interpolation functions are used as discussed in Section 3-2-1. Upon substituting these in the weak form, the L.H.S volume integrals take the form of the characteristic stiffness and mass matrices that arise in many FEM applications. For first-order tetrahedral elements with Nédélec basis, each element has six degrees of freedom, one on each edge (Jin, 2015). Hence, the stiffness and mass matrices have six different basis functions per element, resulting in local matrices of size (6×6). For an element $m \in \{1, 2, \ldots, M\}$, they have the form:

$$K^m_{ij} = \iiint_\Omega (\nabla \times \mathbf{N}^m_i) \cdot (\nabla \times \mathbf{N}^m_j)\, dV, \tag{3-20a}$$

$$M^m_{ij} = \iiint_\Omega \mathbf{N}^m_i \cdot \mathbf{N}^m_j\, dV, \tag{3-20b}$$

where $i, j \in \{1, 2, \ldots, 6\}$ denoting the edges of the element. Combining these to form the complete local L.H.S for Equation (3-15) gives:

$$A^m_{ij} = \frac{1}{\mu_r} K^m_{ij} - k_0^2 \varepsilon_{r,\text{eff}} M^m_{ij}. \tag{3-21}$$

The source element array is now given by:

$$b^m_i = -jk_0 Z_0 \iiint_\Omega \mathbf{N}^m_i \cdot \mathbf{J}^m_s\, dV. \tag{3-22}$$

Form Global System Matrices by Assembly of All Elements

After evaluating all element-wise local matrices A^m (Equation (3-21)), they are assembled into one global system matrix A based on what index of each local matrix corresponds to

what index in the global edge index list. This is kept track of using the geometry information from `tetgen`. Just as how A^m have a size of (6×6) corresponding to six local DOFs, A has size of [DOF $\times$ DOF]. The global source vector $\mathbf{b}$ is built by concatenating Equation (3-22) together. This results in a global linear system of algebraic equations:

$$\mathsf{A}\mathbf{x} = \mathbf{b}, \tag{3-23}$$

where $\mathbf{x}$ contains all the coefficients E_j^m as in Equation (3-16). This system is complex symmetric.

Solve the System

Solving this system of equations can be done by a multitude of methods and linear system solvers. For `elfe3D` and also `elfe3D_GPR`, the software `MUMPS` is employed to find the solution vector $\mathbf{x}$. `MUMPS` is a highly efficient sparse direct solver for linear systems (Amestoy et al., 2000) written in Fortran and supports OpenMP parallelization. It uses multifrontal method to factor and solve large, distributed linear systems.

3-2-2 Error Estimation for Adaptive Refinement

Once the system is solved, numerical errors are estimated for adaptive refinement in `elfe3D`. It iteratively improves the input simulation mesh, by adding new elements in areas of high error (Rulff et al., 2021). It includes refinement based on the residual of the CSEM PDE Equation (3-4a), face jump in normal current density between elements based on Equation (3-6), and face jumps of tangential magnetic fields, since these are not ensured by the weak form of the PDE. If the errors based on these metrics cross an experimentally-determined threshold in an element of the simulation region, these specific elements are reduced in size by bisection (Rulff et al., 2021). This threshold needs to be set based on individual accuracy requirements. For `elfe3D_GPR`, I have discussed adaptive refinement implementation in Section 4-3-1.

Obtain the Results and Post-processing

Once the unknown coefficients are found, the electric and magnetic field values at the receiver sites or the entire volume can be found by multiplying the coefficients with the basis functions as in Equation (3-16). If a line of receivers of electric field are given, a radial decay plot can be obtained. Moreover, centroids of each tetrahedra can be used to get a 3D volumetric data of field distribution in the complete simulation domain. Then, multiple other post-processing procedures can be conducted based on the requirements of the users, such as field-component plotting, spectral analysis, or supplying the data to an inversion software.

With this, I completely describe th FE framework used in `elfe3D_GPR`, from minimal modifications of `elfe3D`. Now, to tackle the problem of outgoing field absorption (Section 3-1-4), I will start with describing the history and development of PML.

3-3 Perfectly Matched Layers for Wave EM

All physical phenomena described by the wave equation bounded in a finite domain need to make the boundary as transparent to the outgoing waves as possible (Bérenger, 2007). Initially, ABCs were developed for use in FE implementations that lead to localized relations to the boundary fields in terms of mixed boundary conditions (Jin, 2015). They required careful analytical treatment, and their effectiveness was limited (Engquist & Majda, 1977; Monk, 2003). This changed with the introduction of PMLs. PML literature has been enriched by the fact that wave phenomena are not limited to EM, but to fields such as hydrodynamics, oceanic sciences, elastodynamics, optics and quantum mechanics (Pled & Desceliers, 2022), and can also be studied application agnostic using the Helmholtz equation (Bermúdez et al., 2004). This allowed for a rapid comprehensive development of its theory and numerical implementation.

3-3-1 Initial Split Field PML

(Berenger, 1994) introduced the PML in time domain with a split-field formulation for absorbing waves in free space simulations in two dimensions. For the transverse electric (TE) mode of EM waves with field components E_x, E_y, H_z, he split the magnetic field H_z into two components such that the Faraday's law (Equation (3-1a)) can be written down in two equations. One equation includes H_{zx} that is responsible for creation of E_x field component, and H_{zy} that is responsible for creation of E_y field component. Each of these magnetic field components were assigned their own component of magnetic conductivity, σ_x^* and σ_y^*, respectively. This allowed Bérenger to introduce the matching condition for vacuum:

$$\frac{\sigma}{\epsilon_0} = \frac{\sigma^*}{\mu_0}. \tag{3-24}$$

This condition ensures that there is no impedance mismatch at the interface between the PML and free space. He then showed that a similar approach works with splitting the E_z component for the TM mode, giving a complete field reflection-less transmission of energy into the PML region. Using FD terminology, he also showed how the propagation of waves in the PML medium and transmission between layers of PML, corresponding to lateral points across the PML extents, is reflection-less and absorbing. This set the groundwork for perfectly matched layers.

3-3-2 Complex Stretching and Uniaxial PML Formulations

As much as the split-field PML is effective, it had its limitations. One, magnetic conductivity is not a typical material parameter used in exisiting numerical codes. Two, due to the field splitting, it creates significantly more DOFs due to the artificial field components which worsens the conditioning of the system of equations. Clearly, new methods were sought that achieve the same perfectly matching effect with minimal changes to the system. Here, two major lines of work developed, both with a view to realize the PML without the intensive field splitting methodology (Pekel & Mittra, 1995; Rappaport, 1996).

The first line of work lead to Uniaxial-PML (U-PML), or equivalently, the Anisotropic-PML (A-PML) (Pled & Desceliers, 2022; Rappaport, 1996). Here, the PDE Equation (3-11) is

preserved, only a specific frequency-dependent complex anisotropic material is introduced in the PML region. Due to the definition of this fictitious material, described in Section 4-2-1, it does not create new DOFs to solve for, other than the typical expected DOFs from introducing the PML volume. This makes it much more tractable. Introduced by (Sacks et al., 1995), its matching condition is implemented by anisotropic material matrices. It is given by:

$$\frac{\overleftrightarrow{\varepsilon}}{\epsilon_0} = \frac{\overleftrightarrow{\mu}}{\mu_0} \tag{3-25}$$

where $\overleftrightarrow{\varepsilon}$ and $\overleftrightarrow{\mu}$ are the permittivity and permeability tensors of the PML medium. This implies that both the permittivity and permeability should be modified equally to ensure impedance matching. Analysis was conducted early on to study the equivalence between the U-PML and the Bérenger PML (Wu et al., 1997), which showed that this interpretation indeed allows perfect matching as long as the parameters of the PML medium are chosen well.

The alternative line of research for the PML lead to the Stretched-Coordinate PML (SC-PML) (W. C. Chew & Jin, 1996; Levy, 2000). This involves a complex continuation of coordinates in the PML region from real coordinates in the simulation domain that it encloses. This is done via complex stretching functions that map over real coordinates in a PML region of the simulation mesh. Doing such a complex transform of coordinates and solving for the wave equation Equation (3-11) using plane wave approximation reveals that the imaginary component of the complex coordinate imposes exponential decay to the wave according to the scaling provided by the stretching functions (Bérenger, 2007; Levy, 2000). This function is required to be smooth, and monotonically increasing in the PML region. The transformation of coordinates can be expressed in many equivalent ways, one of them expressed by (Bermúdez et al., 2004) for a 1D domain as:

$$\tilde{r} = \tilde{r}(r) := r + \frac{i}{\omega}\int_0^r \gamma(\tau)d\tau \quad \text{for } r \in [\Gamma_{\text{model}}, \Gamma_{\text{total}}), \tag{3-26}$$

with a corresponding stretching function $s(r)$ for free space:

$$s(r) := 1 - j\frac{\gamma(r)}{\omega\varepsilon_0}. \tag{3-27}$$

Here, $\tilde{r}$ is the stretched complex coordinate, r is its real coordinate, γ is a decay function, Γ_{model} is the inner simulation domain-to-PML boundary, and Γ_{total} is the outer boundary of the PML region. Decay function γ serves as the primary means of controlling attenuation within the PML region such that impedance is matched at simulation domain-PML boundary. Moreover, they should provide enough cumulative decay to the waves incoming into the PML such that by the time the waves reach the end of simulation domain extents, their strength is negligible. For FE formulation, a sufficiently thick PML is the equivalent of multiple layers of PML in structured FD.

This resulting PML formulation involves complex operators, rendering the PML method usually difficult to implement along with any conventional numerical approximation method (Pled & Desceliers, 2022). This will also become apparent when I attempt implementing it during my thesis (Appendix A). However, it still saves a significant number of DOFs than the split-field PML that Bérenger introduced. Moreover, the use of a SC-PML does offer faster solution convergence speed than an U-PML (Ji et al., 2020).

3-3-3 The Exact-PML

Considerable mathematical efforts have been made to analyze the various aspects of PML formulations using the Helmholtz equation and the EM scattering problem such as their stability and convergence properties (Bermúdez et al., 2004; J. Bramble & Pasciak, 2007; J. H. Bramble & Pasciak, 2012; Galkowski et al., 2022; Harari et al., 2000). To make the PML as efficient as possible, not just in performance, but also in implementation, (Bermúdez et al., 2004) introduced the idea of an Exact-PML using Helmholtz equation with Sommerfeld radiation condition. The PML is based on CS-PML, except they choose the decay function γ such that its integral in the finite PML region reaches $+\infty$. This is different from the conventional polynomial decay functions, which have a finite integral. This difference is illustrated in Figure 3-4. This remarkable feature makes the solution of the PML problem coincide with the original problem, as potentially infinite attenuation corresponds to the physical problem in unbound space. For implementation using FEM, they prescribe Dirichlet boundary condition on the outer boundary of the PML region. This makes the entries of the FE system matrices finite on the boundary, which introduces some numerical errors. However, with the asymptotic behavior of decay function right before the boundary, it is considered that the amount of attenuation should be sufficiently high to make any outgoing wave decayed to non-significant values. This makes its accuracy remarkable. (Feng, Ding, & Wang, 2019) applies this concept to unstructured FE with adaptive meshing in frequency domain with extensive sensitivity analysis, (Ozgun et al., 2023) implements the Exact-PML for Helmholtz-like vector PDE in locally conformal mesh, and (Karperaki et al., 2019) applies this to modelling acoustic waves in the ocean. Another remarkable fact of these exact decay functions is that the resulting PML have no parameters to tune other than the PML's thickness - as the thickness determines how fine the PML region mesh is required to be to capture the gradients of high attenuation. This makes them easier to implement reliably than the conventional polynomial based functions that have multiple parameters to arbitrarily tune (Bérenger, 2007; Jin & Riley, 2008).

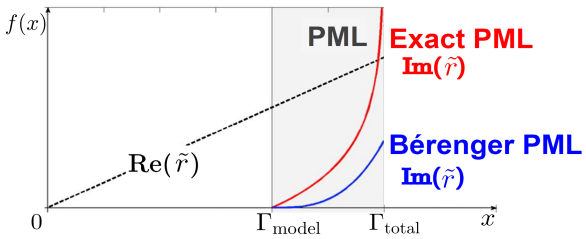

Figure 3-4: Difference between coordinate transformation applied by an exact decay function versus a conventional (Bérenger) decay function in 1D. The real component ($\mathrm{Re}(\tilde{r})$) stays the same, while the imaginary component ($\mathrm{Im}(\tilde{r})$) dictates the amount of attenuation. Modified from (Karperaki et al., 2019).

3-3-4 The Complex Frequency Shifted PML, and Other PML Formulations

There are other intensively researched types of PML formulations, such as the Complex Frequency Shifted PML (CFS-PML), the Convolutional PML for time domain (C-PML) (Bérenger, 2007), the generalization of the U-PML which is Multi-Axial PML (M-PML)

(Pled & Desceliers, 2022), PML which is locally conforming to geometry (LC-PML) (Smull et al., 2017) and the Auxiliary Differential Equation PML (ADE-PML) which uses Auxiliary Differential Equation form of the Maxwell's equations to create the PML. Out of these, I will describe the CFS-PML, as it is the most relevant to the work in this thesis, being the continuation of the SC-PML and contributing to the discussion of the completed PML (Section 4-2-5).

The CFS-PML adds a new coefficient in the stretching function compared to a typical SC-PML. This is done to alleviate stability issues of the PML with near-grazing incidence and evanescent waves (Bérenger, 2007; Pled & Desceliers, 2022). As such, the stretching function formula for CFS-PML given by (Bérenger, 2007) is:

$$s(r) = \kappa(r) + \frac{\gamma(r)}{\alpha(r) + j\omega\epsilon_0} \tag{3-28}$$

where, $\kappa(r)$ is generalization of the real part of the the stretching function in Equation (3-27), and $\alpha(r)$ is the new coefficient administering the complex frequency shift. Due to the fact that the denominator now has a non-zero real component along with a non-zero imaginary component, the resulting stretching function has a $\gamma(r)$ dependent real part as well as an imaginary part. This creates better matching and attenuation for incident near-grazing propagating waves and evanescent-waves into the PML as explained in Pled and Desceliers (2022).

3-3-5 Various PML Modifications

There have been other unique developments in applying these PML formulations in various numerical simulation cases. (Wolfe et al., 2000) used the U-PML as a means to divide the simulation domain into subdomains for parallel computing, while (Ji et al., 2020) worked on finding optimal PML parameters for the SC-PML depending on property of the medium of simulation. The PML has been applied to curvilinear coordinates (Davidson & Botha, 2007; Smull et al., 2017), for special structures like periodic waveguides and electromagnetic cavity, with unique properties (S. Cui & Weile, 2002; Schnaubelt et al., 2023; Selleri et al., 2001), and extended to higher orders (Jiao et al., 2003; Ledger et al., 2002), formulated for spectral elements (Zhang et al., 2018) and parametric finite elements (Matuszyk & Demkowicz, 2013).

3-3-6 PML with FEM and GPR

Lastly, some of earliest works for PML in the FEM framework was done by (Pekel & Mittra, 1995), implementing the SC-PML. After this, (Abenius et al., 2005; Do Nascimento & Jiao, 2024; El Kacimi et al., 2019; Feng, Ding, & Wang, 2019; Jin & Riley, 2008), among others have applied the PML for various versions of the FEM problem with EM waves. Specifically for GPR simulations, (Feng, Ding, & Wang, 2019; Feng, Wang, & Zhang, 2019; Wang et al., 2023) uses the Exact-PML in the context of GPR simulations in frequency domain. (Xue et al., 2025) gives a comprehensive GPR simulation workflow with the Discontinuous-Galerkin FEM and U-PML implemented on unstructured mesh. Moreover, (Jiang & Duan, 2022) have worked on PML for layered media in the context of GPR.

Using the combined insights from all these various PML approaches and innovations, I have implemented a PML absorbing boundary for `elfe3D_GPR`. The exact steps I have followed are described in the following chapter, Section 4-2.

Chapter 4

Implementation of GPR Forward Problem using Perfectly Matched Layers

Once the various physical and FE differences between CSEM and GPR simulations have been identified as mentioned in Chapter 3, it is next reflected in the development of `elfe3D_GPR`. For the implementation of the GPR simulation using `elfe3D` as the base code, I made a few major and minor changes in a few steps of the FEM framework of `elfe3D` (Figure 3-2).

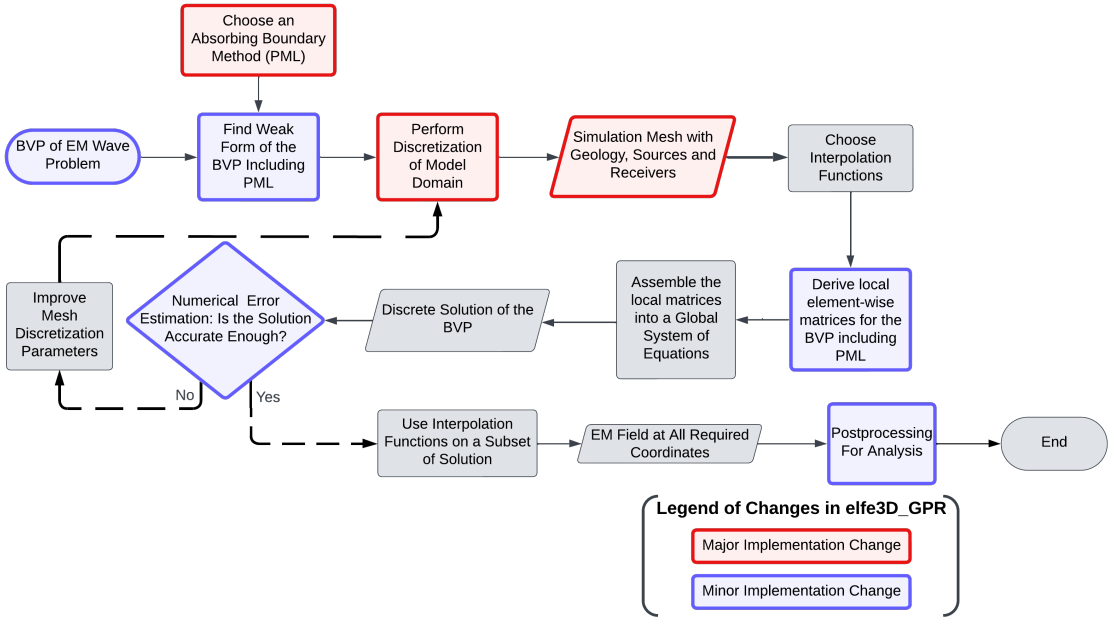

Figure 4-1: The general FEM framework for EM problems with changes made from `elfe3D` to `elfe3D_GPR`. Major changes are marked in red and minor changes in blue.

The flowchart highlights that the major changes from `elfe3D` have been in two key areas:

1. **The Absorbing PML Boundary**: This did not exist in `elfe3D`, where appropriate domain truncation was sufficient to allow using a homogeneous DBC on the simulation domain boundary (Sections 3-1-3 and 3-1-4). Due to the PML, changes occur in the BVP of the GPR problem (Equation (3-11)). This leads to changes in the problem's weak form, and hence, the FE system matrices.
2. **Discretization**: Between CSEM and GPR, the discretization methodology changes from using a skin-depth centered approach to a wavelength centered approach. Moreover, since the PML requires a finite-thickness region enveloping the actual region of interest, it adds complexity to the meshing of the total simulation region.

4-1 Discretize the Simulation Domain Using Finite Elements

There are a few essential features and requirements that a GPR simulation mesh needs to adhere to. The requirements get more complex as a PML is introduced, as discussed in Section 4-2. To ensure that the discretization is adequate for accuracy constraints while checking computational requirements, I conducted a systematic set of numerical experiments to verify and establish these constraints. The resulting `elfe3D_GPR` test models and their relevant parameters are presented and discussed in Chapter 5.

A characteristic simulation mesh that is being used produced using `tetgen` has the following essential features:

1. **Truncated Simulation Domain**: `elfe3D_GPR` works in 3D Cartesian coordinates. Hence, there will be three orthogonal axes $\{x, y, z\}$. The horizontal plane described by x and y axes, while z represents height by positive z direction, and depth by negative z direction in my simulations, though it can be made opposite as well as per the more conventional system. The simulation domain extents in each direction can be set flexibly. However, as studied by examples in Chapter 5, it is clear that there are some limitations in how small the domain has to be around the source and receivers before the PML can be placed before it.
2. **Source Antenna**: All of my `elfe3D_GPR` studies were done using a point dipole approximation. This source is defined by a single line segment in the mesh with a finite size, while the FE basis functions expand it to the elements in the mesh that are connected by the line segment. To compare my simulation results using an analytical solution with a simple test case, it becomes crucial to ensure this source length l_s is negligibly small compared to the wavelength of EM field emitted by the antenna λ. This choice of l_s as a ratio of wavelength has also been studied in my tests (Chapter 5) that would give accurate solution as compared to a point source. However, for real world use cases, the source dimensions can be made equal to the original antenna length.
3. **Receiver Location(s)**: For the purpose of testing accuracy, multiple points in the simulation domain are marked for recording field data, slightly below the air-earth interface. These were along two directions respective to the antenna on the $x - y$

plane: endfire and broadside. While generating the `tetgen` input mesh, at each of the receiver locations, a triangle is defined around the point on the air-earth interface. The triangles ensure that small tetrahedra are generated pointing above and into the subsurface. The actual receiver points have been placed within the tetrahedra generated below the interface by choice. The purpose of this sophisticated definition is to ensure that the receivers lie within elements such that no discontinuities can occur at the receiver points.

4. **Air-Earth Interface**: A GPR device, such as (pulseEKKO, Sensors & Software Inc., 2023) usually positions the antenna some small distance above the ground. As such, an air-earth interface definition needs to be established. Defining the interface properly is essential to ensure that the simulation mesh properly marks each element in the domain to correct region properties.

5. **Subsurface Layer(s)**: The near surface earth region has a rich diversity of possible electric material distributions (Annan, 2005). Materials with a difference in these properties produce interfaces that reflect GPR signals. Hence, for synthetic testing of `elfe3D_GPR`, it is essential to test the response from a layered model in addition to a whole-space and half-space simulations. These layers were defined parallel to the air-earth interface for ease of verification with analytical solution and validation against `empymod` (Werthmüller, 2017). It is a full 3D EM modeller for 1D vertically transverse isotropic media, written in Python. It computes the frequency-domain EM response using analytical solutions and fast numerical Hankel transforms. Soon after being its release, a digital linear filter was designed specifically for use in wave-field modelling for GPR (Werthmüller et al., 2019). I use this filter for validation of `elfe3D_GPR`.

6. **Subsurface Anomaly**: Similar to layered earth media, there exist a variety of cases where an electric medium with anomalous set of properties with respect to the embedding can be present, such as (Annan, 2005). Hence, I test one such synthetic case in `elfe3D_GPR`.

7. **PML**: A PML bounds the regular simulation domain with a finite thickness layer of an artificial medium that absorbs outgoing waves in all directions such that the truncated simulation domain can accurately represent the open-world limitlessness. I discuss PML meshing in Section 4-2.

For illustrating an example simulation domain mesh, consider the following set of parameters:

Table 4-1: Example simulation mesh parameters.

Model Parameter		Specification	
Category	**Variable**	**Value**	**Units**
Domain Truncation	Extents in x-axis	$[-5, 5]$	m
	Extents in y-axis	$[-5, 5]$	m
	Extents in z-axis	$[-4, 1]$	m

Table 4-1: Example simulation mesh parameters (continued).

Model Parameter		Specification	
Category	**Variable**	**Value**	**Units**
Air-Earth Interface	Extents in x-axis	$[-5, 5]$	m
	Extents in y-axis	$[-5, 5]$	m
	z-axis value	0	m
Air Layer	$\{\varepsilon_r, \sigma, \mu_r\}$	$\{1, 1e\text{-}16, 1\}$	$\{-, S/m, -\}$
	Maximum Element Volume	$3.1820e\text{-}03$	m^3
Subsurface Layer 1	Extents in x-axis	$[-5, 5]$	m
	Extents in y-axis	$[-5, 5]$	m
	Extents in z-axis	$[-2, 0]$	m
	$\{\varepsilon_r, \sigma, \mu_r\}$	$\{4, 1e\text{-}4, 1\}$	$\{-, S/m, -\}$
	Maximum Element Volume	$3.9775e\text{-}04$	m^3
Subsurface Layer 2	Extents in x-axis	$[-5, 5]$	m
	Extents in y-axis	$[-5, 5]$	m
	Extents in z-axis	$[-4, -2]$	m
	$\{\varepsilon_r, \sigma, \mu_r\}$	$\{9, 1e\text{-}3, 1\}$	$\{-, S/m, -\}$
	Maximum Element Volume	$1.1785e\text{-}04$	m^3
Source Antenna	Dipole Direction	$+x$-axis	–
	Extents in x-axis	$[-2.5, 2.5]$	mm
	Fixed y-axis value	0	m
	Height from Interface	2.5	cm
	Source Moment Magnitude I	1	$\mathrm{A/m}^2$
	Source Frequency	100	MHz
Endfire Receiver Line	Number of Receivers	256	–
	Start and End x-values	$[0.2, 4.8]$	m
	Depth from Interface	1.25	mm
Broadside Receiver Line	Number of Receivers	256	–
	Start and End y-values	$[0.2, 4.8]$	m
	Depth from Interface	1.25	mm
Oblique Receiver Line	Number of Receivers	256	–
	Start and End x-values	$[0.1414, 3.3941]$	m
	Start and End y-values	$[0.1414, 3.3941]$	m
	Depth from Interface	1.25	mm

The source moment magnitude I is given by

$$I = \left|\left| \int_{\Omega_s} J_p(\mathbf{r}) \, \mathrm{d}V \right|\right|, \tag{4-1}$$

evaluated over all volume Ω_s where the source current is non-zero, and $\mathbf{r}$ is the position vector of each integration point relative to the origin.

The example simulation has two subsurface layers extending across the domain, sharing one interface at $z = -2$ m. The resulting mesh is illustrated below:

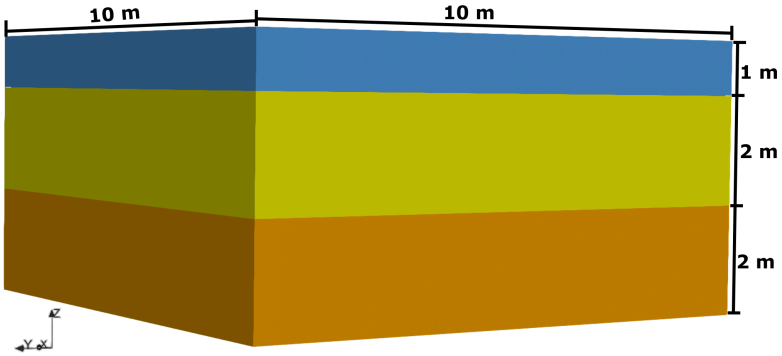

(a) The 3D simulation domain, with air layer on top, and the two earth layers below it.

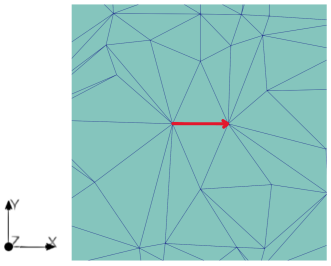

(b) Dipole source segment in mesh (marked in red)

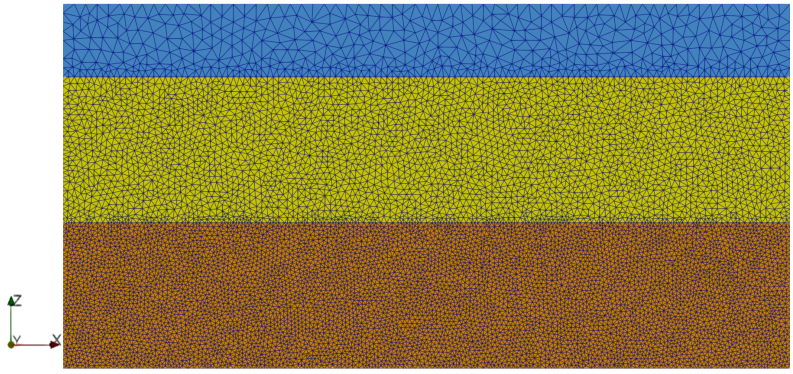

(c) Cross-section of the 3D domain, showing varying discretization for each layer.

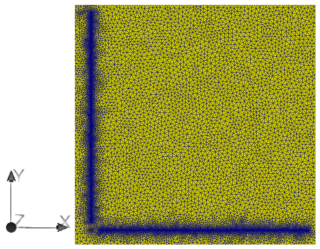

(d) Both dense receiver lines: endfire along x, broadside along y.

Figure 4-2: Example simulation mesh visualization.

Visualizing the mesh is done using `Paraview` (Ahrens et al., 2005). It clearly shows that the input files generated by tetgen do match the specifications mentioned in **??**. The domain extents and interfaces all correctly assigned Section 4-1. For the source segment visualization Section 4-1, I take a slice of the 3D file along the xy-plane, and marking the line is done programmatically in `Paraview`. Its length is 300 times smaller than the wavelength in the first subsurface layer.

In Section 4-1, I illustrate a cross-section perpendicular to the $+x$ axis. Here, it is clear that the different simulation regions have different maximum volumes. This is a requirement based on wavelength of the GPR wave in each medium. The formula for GPR's wavelength in a dielectric medium is given by (Annan, 2005):

$$\lambda_m = \frac{c}{f\sqrt{\varepsilon_r}} \tag{4-2}$$

where λ_{medium} is the wavelength in a medium, c is the speed of light, f is the frequency of the source wave. As is apparent, at any given frequency of source wave, the wavelength is

inversely proportional to $\sqrt{\varepsilon_r}$. This implies that a medium with higher relative permittivity is required to be proportionately sampled by $\sqrt{\varepsilon_r}$ times smaller edge lengths of elements.

The volumes for these media are evaluated by calculating the wavelength each region will have based on the same source frequency, and substituting the criteria of minimum edge length of a tetrahedra being $\lambda/10$. The receiver lines shown in Section 4-1 are defined by triangles of the same length as the source, making the receiver line area finely discretized as well.

This resolution does come with a cost, however, since the mesh has a total of 5.24 million tetrahedra. For a vector FEM formulation, the DOFs correspond to the number of edges in the mesh, which are 6.18 million in number. These numbers do not account for the PML region yet. Clearly, this requires considerable computational resources. To ensure efficient meshing with reasonable accuracy, and minimizing the number of DOFs, I conduct multiple numerical experiments such that future usage of `elfe3D_GPR` is as resource-optimized as possible.

4-1-1 Constructing the PML Mesh Elements

The simulation region in geophysical simulations in `elfe3D_GPR` in 3D is truncated by a cuboidal domain (Section 4-1). Hence, I choose to construct the PML by placing a set of rectangular boxes with coordinates and dimensions such that they wrap around the domain with a uniform thickness in all three dimensions. Building this set of boxes is tricky via `tetgen`, especially when the model is layered because the layer interface continuity should be maintained into the PML for accuracy (Bérenger, 2007). The PML region is also discretized using the same first-order tetrahedra as the regular simulation domain. Hence, the PML does not have multiple layers as per the FD terminology, rather, its total thickness can be perceived as equivalent to the complete set of FD PML layers.

To illustrate the various set of boxes that altogether compose my PML, I now illustrate the same example mesh as in Section 4-1 with parameters from **??**, with the addition of th PML of uniform thickness of 1.5 m in all sides:

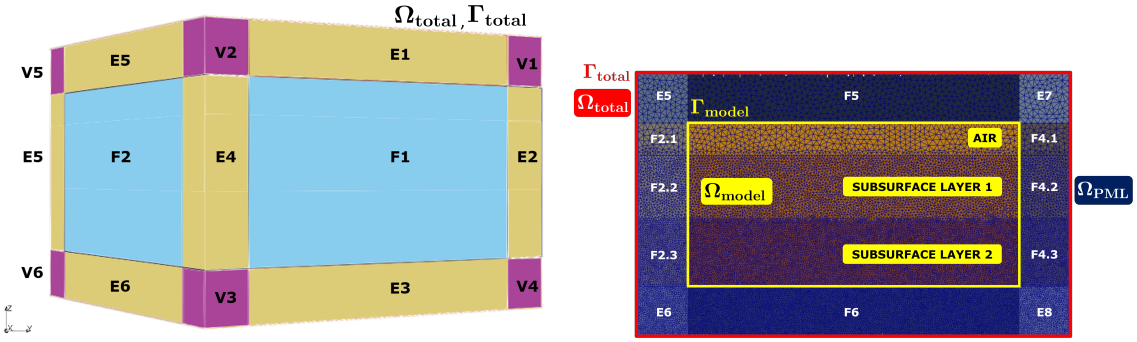

(a) The same two-layered 3D simulation domain as in Section 4-1, now with PML surrounding it.

(b) Cross-section of the 3D domain, showing varying discretization for each layer as in Section 4-1, including the PML.

Figure 4-3: Example simulation mesh with PML visualization.

Here, Ω_{total} is the total mesh volume, with mesh boundary Γ_{total} over which the DBC will now be applied. Ω_{model} is the total geophysical model volume whose region is of interest to

us, with the model boundary being Γ_{model}. The volume between Γ_{total} and Γ_{model} is the PML volume, denoted by Ω_{PML}. Thus, $\Omega_{\text{total}} = \Omega_{\text{model}} \cup \Omega_{\text{PML}}$.

From Figure 4-3a, it is clear that the rectangular boxes surrounding the simulation domain can be categorized into three types:

1. **Extending each face of the simulation domain (Marked with F in Blue)**: Per each geophysical layer and air region of the domain, there will be six new boxes corresponding to the six sides of the cuboidal domain. This is why **F1** and **F2** (Figure 4-3a) are a group of three boxes (with slightly different colors in the diagram) since the model has an air region and two subsurface layers. These boxes extend in the domain's $\pm x$, $\pm y$, $\pm z$ directions. In each of these boxes, the stretching factor (Equation (4-10)) is defined in the direction of the normal vector pointing along their respective coordinate axis.

2. **Extending each edge of the simulation domain (Marked with E in Yellow)**: Per each geophysical layer and air region of the domain, there will be 12 new boxes corresponding to the 12 edges of the cuboidal domain. This is why **E2**, **E4** and **E5** (Figure 4-3a) are a group of three boxes since the model has an air region and two subsurface layers. In each of these boxes, the stretching factor is defined in the direction of the normal vector that is a combination of the normal vectors of the two faces that meet at each edge.

3. **Extending each vertex of the simulation domain (Marked with V in Pink)**: Per each geophysical layer and air region of the domain, there will be eight new boxes corresponding to the eight edges of the cuboidal domain. In each of these boxes, the stretching factor is defined in the direction of the normal vector that is a combination of the normal vectors of the three faces meeting at that corner.

This mesh has nearly 13 million elements. That is a very huge increase in the number of elements compared to the original mesh's 5.24 million elements. It can be understood from Figure 4-3b that the lowest layer (**F2.3**, **F4.3**, **F8**, **E6** and **E8**) having a very dense meshing based on its wavelength is causing a very large increase in PML elements.

4-2 Mathematical Formulation of Perfectly Matched Layers in elfe3D_GPR

With the successful generation of this PML mesh bounding the regular simulation domain, I now apply complex stretching functions to the PML elements. To do this, there are two standard choices for simulating the GPR forward problem: the SC-PML and the U-PML (Section 3-3-2). For elfe3D_GPR, I have chosen to implement the U-PML. For first-order edge-based Nédélec basis functions, U-PML offers a direct implementation methodology which translates well to programming it into the FEM system during assembly of local matrices into the global system matrix.

I first describe the mathematical modifications that the U-PML formulation prescribes to be implemented into the general FE framework. These have been directly programmed into

`elfe3D_GPR`. Once this is tested with the assumption of a homogeneous whole-space medium (Section 5-1), I extend it for layered and arbitrary geophysical media. After testing these considerations (Sections 5-2 and 5-3), I conclude the implementation of an accurate and efficient PML strategy for GPR simulations with `elfe3D_GPR` in 3D.

4-2-1 Implementing the U-PML

U-PML formulates the PML as if it were an anisotropic absorber (Section 3-3-2). I use descriptions of U-PML from Ding et al. (2025) and Jin and Riley (2008) to implement it in `elfe3D_GPR`.

The procedure starts with changing the medium parameters in a PML region to an anisotropic medium using the following tensor representation:

$$\overleftrightarrow{\varepsilon}_{\text{eff}} = \varepsilon_{\text{eff}} \overleftrightarrow{\mathbf{\Lambda}}, \tag{4-3}$$

$$\overleftrightarrow{\mu} = \mu \overleftrightarrow{\mathbf{\Lambda}}. \tag{4-4}$$

Here, $\overleftrightarrow{\mathbf{\Lambda}}$ is the stretch factor tensor, given by:

$$\overleftrightarrow{\mathbf{\Lambda}} = \begin{bmatrix} \frac{s_y s_z}{s_x} & 0 & 0 \\ 0 & \frac{s_x s_z}{s_y} & 0 \\ 0 & 0 & \frac{s_x s_y}{s_z} \end{bmatrix}, \tag{4-5}$$

where s_x, s_y, and s_z are the usual stretching factors in the x, y, and z directions, respectively. Notice that the same tensor is multiplied to both PML material parameters, ε and μ, making it match the impedance condition Equation (3-25). With this transformation, the PDE for the wave equation in the PML region Ω_{PML} becomes:

$$\nabla \times \frac{1}{\overleftrightarrow{\mu}} \nabla \times \mathbf{E} - k_0^2 \overleftrightarrow{\varepsilon}_{r,\text{eff}} \mathbf{E} = -jk_0 Z_0 \mathbf{J}_p \quad \text{in } \Omega_{\text{PML}}. \tag{4-6}$$

Hence, the new stiffness and mass matrices become:

$$\tilde{K}^e_{lj} = \iiint_{V_e} (\nabla \times \mathbf{N}^e_l) \cdot \overleftrightarrow{\mathbf{\Lambda}}^{-1} \cdot (\nabla \times \mathbf{N}^e_j) dV, \tag{4-7}$$

$$\tilde{M}^e_{lj} = \iiint_{V_e} \mathbf{N}^e_l \cdot \overleftrightarrow{\mathbf{\Lambda}} \cdot \mathbf{N}^e_j dV, \tag{4-8}$$

where $\overleftrightarrow{\mathbf{\Lambda}}^{-1}$ is the inverse of the stretch factor tensor.

Implementing this is straightforward for the stiffness matrix, since the dot products imply that each vector component is multiplied with only one corresponding component of the tensor. Hence, the new stretched stiffness matrix can be evaluated as:

$$\tilde{K}^e_{lj} = \frac{s_x}{s_y s_z} K^e_{x,lj} + \frac{s_y}{s_x s_z} K^e_{y,lj} + \frac{s_z}{s_x s_y} K^e_{z,lj} \tag{4-9}$$

The $K^e_{x,lj}$, $K^e_{y,lj}$, and $K^e_{z,lj}$ are the original stiffness matrix terms for the x, y, and z components of the stiffness matrix from (Jin, 2015).

For the mass matrix, however, it is not as straightforward to figure out how to implement the tensor multiplication. Jin (2015) gives explicit component-wise formulas for each entry of a local mass matrix that makes it not directly clear what component of $\overleftrightarrow{\mathbf{\Lambda}}$ to multiply to which terms of the entries of mass matrix. Thankfully, Ding et al. (2025) show explicitly how to implement the stretched mass matrix using the same first-order Nédélec basis functions that (Jin, 2015) describes. This allowed me to complete the U-PML implemention in elfe3D_GPR.

4-2-2 The Stretching Factor in Use and PML Decay Functions

The stretching factor I use now is different than the one described in (Equation (3-27)), since I follow the recently introduced formulation as in (Ding et al., 2025; Feng, Ding, & Wang, 2019; Ozgun et al., 2023). The exact form of stretching factor I use at a point in the PML $p = (p_x, p_y, p_z)$ is:

$$s_i(p_i) = 1 - j\frac{\gamma_i(p_i)}{k_{\text{PML}}} \quad \text{for } i \in \{x, y, z\}, \tag{4-10}$$

where $s_i(p_i)$ is the amount of stretch applied in i^{th} direction at point p_i, k_{PML} is the complex wavenumber of a specific media of choice (see Section 4-2-3), and $\gamma_i(p_i)$ is the decay function in i^{th} direction, depending only on the coordinate p_i and thickness of the PML region.

There are a number of different functions that can be used for the decay function γ_i. The criteria it has to satisfy are Bérenger, 2007:

1. At the simulation domain to PML boundary, the value should be very small, close to no stretching, and increase with a slow variation. This is to allow un-impeded travel to the waves.
2. It should monotonically increase throughout the region.
3. The FE mesh should be able to accurately capture the gradients of the increasing value.
4. By the time any wave reaches the outer boundary of the PML, it should be attenuated enough that there is no significant strength in the wave amplitude left.

Satisfying these criteria, I used the following decay functions. Here, I am using l for the PML thickness, $d_{i,e}$ for the distance of element e in $i \in \{x, y, z\}$ coordinate axis direction from the inner PML boundary, and $\gamma_{i,e}$ for decay function in i^{th} direction for element e. Naturally, the set of elements that e belongs to lies in Ω_{PML}.

1. Exact Reciprocal Function 1: $\gamma_{i,e} = \dfrac{1}{l - d_{i,e}}$ (Ding et al., 2025; Feng, Ding, & Wang, 2019).
2. Exponential Function: $\gamma_{i,e} = \exp\left(e_f \cdot \dfrac{d_{i,e}}{l}\right)$, where e_f is a scaling factor constant of value 5. This was chosen after some testing with whole-space air model.

3. Polynomial Function (Irving & Knight, 2006): $\gamma_{i,e} = p_f \left(\frac{d_{i,e}}{l} \right)^m$, where p_f is an arbitrary scaling factor constant, and m is a positive integer, of orders usually 3 or 4. I chose $m = 4$, and p_f is chosen to be of value $\sqrt{c_0}$, where c_0 is the speed of light, after testing with whole-space model.

4. Exact Reciprocal Function 0: $\gamma_{i,e} = \frac{1}{l - d_{i,e}} - \frac{1}{l}$. This is modified from (Ding et al., 2025), with the subtraction of $1/l$ making the function start at 0 for $d_{\mathrm{i,e}} = 0$.

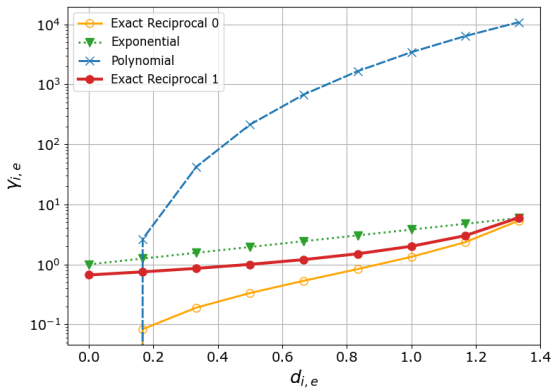

(a) γ_i in PML of $l = 1.5\,\mathrm{m}$, except the last grid point where DBC will be applied.

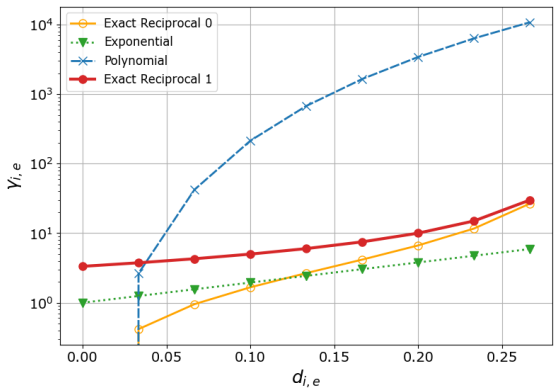

(b) γ_i in PML of $l = 0.3\,\mathrm{m}$, except the last grid point where DBC will be applied.

Figure 4-4: Decay functions γ_i that have been considered. The values are the same as that would be applied to a 1-D PML with 10 equidistant grid points. The last grid point in both subplots is removed since the DBC will be applied on Γ_{total}.

Figure 4-4 shows how the four decay functions behave using the parameters chosen above. Figure 4-4a shows a 1-D simplified representation of $\gamma_{\mathrm{i,e}}$ values as they would be applied in Table 5-1. Similarly, Figure 4-4b shows a 1-D simplified representation of $\gamma_{\mathrm{i,e}}$ values as they would be applied in the k_{min} approach (Table 5-5) of the two-layered model Table 5-4.

I choose to show two versions of the exact decay function because the default function does not start at Γ_{model} from 0, rather from $1/l$. Interestingly, even though both functions are supposed to be exact, in Figure 4-4a they do not reach very high decay values before the last point. The exponential decay function has a steady increase in values, while the polynomial function starts has the largest values owing to its scaling factor.

If the same set of parameters p_f and e_f were considered for a thinner PML, similar to Figure 4-4b, the exact reciprocal decay functions re-scale themselves, while the others provide stay the same and provide relatively lesser attenuation. Hence, the choice to use the exact reciprocal decay function 1 for my initial testing of physical accuracy of the GPR BVP (Section 5-1) arises from the fact that it does not have tunable parameters other than thickness of the PML, and it has been directly used by Feng, Ding, and Wang (2019). Between the exact decay functions, the choice of zero versus finite start has also been checked (Section 5-3-2). These functions makes PML implementation quicker with a guarantee of sufficient attenuation

as per Bermúdez et al. (2004). As long as the discretization is adequately capable to capture the gradients of the decay function without creating significant impedance mismatch at the simulation domain-to-PML interface, this decay function should work well.

4-2-3 PML for Geophysical Models

The near-Earth subsurface has considerable heterogeneity due to presence of different materials and structures, including sediments, rocks, and fluids. Since elfe3D_GPR aims to accurately simulate the forward response of a heterogeneous earth recorded by a GPR device, it is imperative that the PML that it contains should work for any assortment of geological materials with different electric properties. To that effect, I need to make the PML compatible with layered geophysical models and an anomalous half-space model.

For multi-layered geophysical models, the wavenumber of choice k_{PML} used for determining scaling of the stretch in the PML region can be done in a few ways. Bérenger (2007) says that for a PML lying perpendicular to interfaces of layered media, the simulation is perfect only when the amount of stretch in the PML above and below an interface is the same. This result, is, however, for theoretical PML who do not suffer from discretization errors, where using a constant for a decay function would also work (Jin & Riley, 2008).

With this method, a singular wavenumber is to be used across all elements in the PML to scale the stretching factors (Equation (4-10)). This could be decided arbitrarily, as long as enough stretch is applied to the PML region and the discretization being used can capture the gradients of the field decay accurately. Hence, I decided to test two wavenumber choices:

1. k_{max} approach: Wavenumber whose absolute value in the simulation domain is the maximum.
2. k_{min} approach: Wavenumber whose absolute value in the simulation domain is the minimum. This usually corresponds to air's wavenumber.

I will refer to these cases as "**Uniform Stretch**" tests. Important to note here is that the material properties of the PML region above and below the interface must still be kept the same as the material right next to the inner PML boundary in the simulation domain for physically accurate representation of boundless interfaces.

The other approach, as mentioned in (Ding et al., 2025; Feng, Ding, & Wang, 2019; Irving & Knight, 2006), is to vary not only the medium, but also the stretch factor according to the material right next to the inner PML boundary in the simulation domain. Interesting to note here is that both Ding et al. (2025) and Irving and Knight (2006) use this choice for GPR specific simulation for layered and more general media, which is not the case with the uniform stretch approach. I will refer to this case as "**Varying Stretch**" test.

Once the optimal approach is determined, I finalize it for use in elfe3D_GPR.

4-2-4 Adjusted BVP and Weak Form Including the PML

With the inclusion of the PML in elfe3D_GPR, I can finally write the complete BVP that it solves. Combining Equations (3-11) and (4-6) and redefining the meshing regions in Ω, I get

the following BVP:

$$\nabla \times \left(\frac{1}{\mu_r} \nabla \times \mathbf{E} \right) - k_0^2 \varepsilon_{r,\text{eff}} \mathbf{E} = -jk_0 Z_0 \mathbf{J}_p \quad \text{in } \Omega_{\text{model}}, \tag{4-11a}$$

$$\nabla \times \overleftrightarrow{\mu_r}^{-1} \nabla \times \mathbf{E} - k_0^2 \overleftrightarrow{\varepsilon}_{r,\text{eff}} \mathbf{E} = -jk_0 Z_0 \mathbf{J}_p \quad \text{in } \Omega_{\text{PML}}, \tag{4-11b}$$

$$\hat{\mathbf{n}} \times \mathbf{E} = 0 \quad \text{on } \Gamma_{\text{total}}, \tag{4-11c}$$

with the material interface conditions (Equations (3-5) and (3-6)). The regions and boundaries are marked in the example mesh Figure 4-3 and described right after the illustration. It is noted that due to the truncated domain boundary being placed after the PML, that the model's weak form now does not include the Dirichlet BC, rather it is shifted to Γ_{total}.

While the inclusion of PML is directly shown via the GPR wave equation, it has resulted in the PML region effectively solving a different weak form than the simulation region. This follows from the adjusted BVP Equation (4-11). The complete weak form that `elfe3D_GPR` now solves is given by:

Find $\mathbf{E} \in \mathcal{H}^0(\text{curl}, \Omega)$ such that

$$\iiint_{\Omega_{\text{model}}} \frac{1}{\mu_r} (\nabla \times \mathbf{v}) \cdot (\nabla \times \mathbf{E}) \, dV - \iint_{\Gamma_{\text{model}}} \frac{1}{\mu_r} (\mathbf{v} \times \nabla \times \mathbf{E}) \cdot \hat{\mathbf{n}} \, dS - k_0^2 \iiint_{\Omega_{\text{model}}} \varepsilon_{r,\text{eff}} \, \mathbf{E} \cdot \mathbf{v} \, dV = -jk_0 Z_0 \iiint_{\Omega_{\text{model}}} \mathbf{J}_s \cdot \mathbf{v} \, dV, \tag{4-12}$$

and,

$$\iiint_{\Omega_{\text{PML}}} \overleftrightarrow{\mu_r}^{-1} (\nabla \times \mathbf{v}) \cdot (\nabla \times \mathbf{E}) \, dV - \iint_{\Gamma_{\text{total}}} \overleftrightarrow{\mu_r}^{-1} (\mathbf{v} \times \nabla \times \mathbf{E}) \cdot \hat{\mathbf{n}} \, dS - k_0^2 \iiint_{\Omega_{\text{PML}}} \overleftrightarrow{\varepsilon}_{r,\text{eff}} \, \mathbf{E} \cdot \mathbf{v} \, dV = 0, \tag{4-13}$$

$\forall \, \mathbf{v} \in \mathcal{H}^0(\text{curl}, \Omega)$, and satisfying the boundary condition (Equation (3-11b)) on Γ_{total} now as well as the continuity constraints Equations (3-5) and (3-6). Here, the integrals over Γ_{model} and Γ_{PML} evaluate to zero due to continuity constraint Equation (3-5) in the total volume of integration as well as the choice of the vector space $\mathcal{H}^0(\text{curl}, \Omega)$.

4-2-5 Discussion on the Implemented PML

Before I present the testing that was conducted, I must make certain aspects of the PML implementation clearer such that there is no ambiguity.

Implications of the Finalized Stretching Function

From Equations (3-9) and (4-10), it is clear that the denominator of the stretching factor is a complex number. This is unlike the usual definitions of the coordinate stretched PML, where the stretching factor is of the form:

$$s_i = 1 + \frac{\gamma_i}{j\omega\varepsilon} \quad \text{for } i = x, y, z, \tag{4-14}$$

Since only the angular frequency and the permittivity are generally used, the real part of the stretch is usually 1 and does not play a role in stretching, while the imaginary part

stretches the propagating waves. However, in my current implementation, the stretching factor Equation (4-10) can be re-written as:

$$s_i = 1 - \frac{\gamma_i}{k' + jk''} \quad \text{for } i = x, y, z, \tag{4-15}$$

where k' and k'' are the real and imaginary components of the wavenumber, respectively.

This is equivalent to the CFS-PML formulation, whose general form for cartesian PML is:

$$s_i = \kappa_i + \frac{\gamma_i}{\alpha_i + j\omega\epsilon_i}, \quad \text{for } i = x, y, z, \tag{4-16}$$

where κ_i and α_i are arbitrarily defined parameters. This is a natural effect of using the wavenumber definition. The CFS-PML is meant to help absorb evanescent waves and propagating waves that are incident at grazing angles (Bérenger, 2007). Usually the parameters κ_i and α_i are determined parametrically. However, with using the complex wavenumber for scaling the decay function, as per (Ding et al., 2025; Ozgun et al., 2023), I indirectly use a CFS-PML-like expression with exact decay function. Moreover, using wavenumber directly for scaling allows for easier implementation using the BVP for GPR (Equation (4-11)). Combining the PML formulation I have implemented with the FE framework in frequency domain gives it unique characteristics that have been, as of the date of submission of this thesis, previously un-tested.

Complexities with the SC-PML

Before concluding the methodology, I want to describe why the SC-PML could not be implemented in `elfe3D_GPR`. It's complete derivation for the FE local matrix is given in Appendix A. From this derivation, it becomes evident that there are a few sources of inaccuracies.

One, since I evaluate the stretched derivatives on all edges of the elements separately, using the coordinate of the midpoint of each edge to determine the stretch, it may have resulted in non-smooth stretching of the local stiffness matrices of the elements. Two, the stretched volume factor is evaluated using the centroid of the element. This discrepancy in quadrature of evaluation caused non-uniform stretch between the stiffness matrix and the mass matrix.

To fix this, a more sophisticated quadrature rule needs to be established that bridges the evaluation of both stretching terms within the stiffness and mass matrices to equal points of evaluation. It should also account for the smooth variation of stretching for edge-based FEM that the formulation I attempted cannot satisfy. Both of these point to higher order Nédélec basis functions. However, implementing this would be quite intensive, as `elfe3D_GPR`'s entire framework is set up with first-order elements. This is not to forget a new meshing approach will need to be determined with `tetgen`. Hence, I have finalized the U-PML implementation for `elfe3D_GPR`.

4-3 Completing the elfe3D_GPR Forward Solver

In this section, I describe the remaining minor implementation changes that I implemented to complete `elfe3D_GPR` as a forward solver.

4-3-1 Adjusting the Error Estimation for Adaptive Refinement

Adaptive refinement in `elfe3D` iteratively improves the mesh given as an input, by adding new elements in areas of high error (Rulff et al., 2021). It includes refinement based on the residual of the PDE, face jump in normal current density between elements, and face jumps of tangential magnetic fields. Since the magnetic field is computed using Faraday's law on first-order accurate electric field data, the magnetic field becomes a zero-order field. This means that the tangential components of the magnetic field will always jump across the face of an element. This makes it a good criterion to check if the mesh elements are small enough. If the errors based on these metrics cross a user-defined threshold in an element, these specific elements are reduced in size (Rulff et al., 2021). This threshold needs to be set based on individual accuracy requirements.

For `elfe3D_GPR`, I modified `elfe3D`'s implementation to account for the new BVP. First, error estimation is excluded for the PML region, because the PML is not the region of interest and its curl-curl equation is different from the physical curl-curl equation of the simulation domain. For this modification, I refer the implementation in Ren et al. (2013), which was also used for Rulff et al. (2021) for `elfe3D` that have general expressions for the complete Maxwell's equations. Keeping the algorithm the same as in `elfe3D`, I only modify the error estimation expressions to include the effect of permittivity. After implementation, I have, as of yet, been unable to test its accuracy and adjust its thresholds.

4-3-2 Improving the Dirichlet Boundary Condition Implementation

`elfe3D` has an accurate implementation of the Dirichlet BCs Equation (3-4b), which I could have left as is for `elfe3D_GPR`. Unfortunately, as problem sizes grew with the wavelength constraints and layered media with high permittivity, it became essential to optimize computation time. Hence, I have made programming optimization adjustments to the subroutine that applies Dirichlet BC such that it is now much quicker, without requiring parallelization.

After all these adjustments, `elfe3D_GPR` is now capable of simulating general GPR problems in frequency domain. Its complete capabilities are tested and presented in Chapter 5.

Chapter 5

Synthetic Testing and Validation of elfe3D_GPR

In this chapter, I present all significant tests that I have conducted during and after the development of the current version of `elfe3D_GPR`. These serve to verify the accuracy of `elfe3D_GPR` simulation results as well as estimate discretization and truncation limitations using the 3D unstructured mesh along with the PML. Testing of `elfe3D_GPR` is done incrementally from the implementation of the first working version of the PML (Section 3-3), to subsequent changes that completed the software (Section 4-3). These tests are done on four synthetic models: a whole-space model, a half-space model, a two-layered model, and a half-space with anomaly model. I start by presenting these models with a base set of parameters, and their simulation results. Then, I change one or few parameters at a time as required to test various important aspects of the forward simulation code of `elfe3D_GPR` and its modelling constraints. Using these results, I discuss the capabilities of `elfe3D_GPR` and hence the outcomes of this thesis.

5-1 Whole-Space Model: Air

This is a homogeneous air model with a dipole source antenna placed at the center of the simulation domain and receivers near it. Its purpose is to verify if `elfe_GPR` and its PML is able to simulate wave propagation without significant reflections from the truncated simulation domain boundary.

Table 5-1: Simulation parameters for the base whole-space model.

Model Parameter		**Specification**	
Category	**Variable**	**Value**	**Units**
Domain Truncation	Extents in x-axis	$[-5, 5]$	m
	Extents in y-axis	$[-5, 5]$	m
	Extents in z-axis	$[-5, 5]$	m

Table 5-1: Simulation parameters for the base whole-space model (continued).

Model Parameter		Specification	
Category	**Variable**	**Value**	**Units**
Air Medium	$\{\varepsilon_r, \sigma, \mu_r\}$	$\{1, 1e\text{-}8, 1\}$	$\{-, S/m, -\}$
	Maximum Element Volume	3.1820e-03	m^3
	Maximum Edge Length	$\lambda_{air}/10$	m
Source Antenna	Dipole Direction	$+x$-axis	–
	Extents in x-axis	$[-2.5, 2.5]$	mm
	Fixed y-axis value	0	m
	Height from Interface	2.5	cm
	Source Moment I	1	A/m^2
	Source Frequency	100	MHz

In this table and in subsequent usage, λ_{air} corresponds to the wavelength of the electric field at the given source antenna frequency in air. Results from simulating this model are compared against the analytical solution of wave propagation in air with the same source configuration.

The first successful wave-regime simulation using `elfe3D_GPR` used the whole-space air model of Table 5-1. The PML here uses the Exact reciprocal decay function 1 from Section 4-2-2. All six components of the EM field $E_x, E_y, E_z, H_x, H_y, H_z$ are obtained. For inference of the results, I compare the E_x field component with the analytical solution for a homogeneous medium, which can be found in David (2009) and Wait (2013).

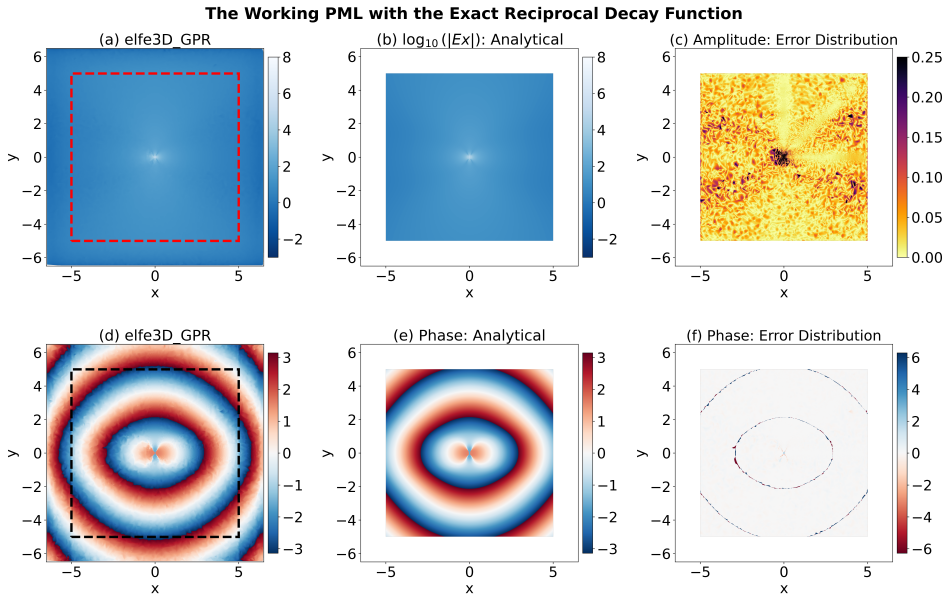

Figure 5-1: Whole-Space Air Model: Amplitude and phase of the E_x component of EM field in whole-space air from an x-directed dipole source. Cross-sections of the 3D domain are taken at 0.01 m below the source, in $x-y$ plane. (a) and (d) is from `elfe3D_GPR`, (b) and (e) shows the analytical solution, and (c) and (f) is the error of `elfe3D_GPR`.

Figure 5-1 shows a 2-D cross-section of $x - y$ plane located at 0.01 m below the source.

The analytical solution is also evaluated in the same plane. The field values of `elfe3D_GPR` simulation are taken at centroids of each tetrahedra in the plane, and interpolated linearly for plotting.

In the cross-sections of amplitude (Figure 5-1 (a)) and phase (Figure 5-1 (d)) belonging to my simulation results, I have marked the inner PML boundary Γ_{model} using dotted lines, hence I do not show that region in the analytical solution. Qualitatively, my simulation results look reflection free and smoothly decaying in the simulation region. Moreover, the amplitude field continues varying smoothly within the PML region as well, whereas the phase plot shows a slight shift at $x = \pm 5$ where the PML starts, showing slight impedance error.

The evaluation of differences between `elfe3D_GPR` results and the analytic results is done using these specific measures:

1. **Normalized Amplitude Error**: $\frac{|E_{x,\text{elfe3D\_GPR}} - E_{x,\text{analytical}}|}{|E_{x,\text{analytical}}|}$, where $|(\cdot)|$ denotes taking the magnitude of a complex number.
2. **Phase Error**: $\angle(E_{x,\text{elfe3D\_GPR}}) - \angle(E_{x,\text{analytical}})$, where $\angle(\cdot)$ denotes taking the phase of the complex number in radians.

In the amplitude error distribution (Figure 5-1 (c)), and for all subsequent results, a normalized error of 1.0 corresponds to 100% error with respect to the analytical solution. Figure 5-1 (c) shows that error in the simulation domain is quite randomly scattered throughout the domain, except for lines in the positive $x - y$ region that correspond to receiver lines. This near-random scattering indicates that the volume constraint used in this experiment discretizes the domain with large unstructured tetrahedra that have significant inter-element discontinuities.

There is a region of high error near the source (in the center of the cross-section). This is expected due to the fact that the model source is a finite length antenna (Table 5-1). On the other hand, the analytical solution is evaluated with a Dirac delta source assumption. Most importantly, an important factor to note is that there are no bands of high error near the edges of the domain. This gives an indication that the PML is able to absorb outgoing waves despite significant error in the complete domain of simulation.

The phase error plot (Figure 5-1 (f)) is also interesting. It shows that there are rings of high error at regular spatial intervals. These correspond to areas where phase jumps from $+\pi$ to $-\pi$, which are expected from any finite discretization. From statistical analysis of the distribution, the mean of phase error is at zero with a standard deviation of 0.53. This shows that, just like amplitude error, the phase also suffers from insufficient discretization.

With this test, I demonstrate that `elfe3D_GPR` can simulate wave propagation even with insufficient discretization in homogeneous media.

5-1-1 Testing Decay Functions

After the success of the exact reciprocal decay function, I tested how well other decay functions can perform with the same PML formulation. Figure 5-2 shows the same $x - y$ plane cross sections as in previous section, now with the first three alternative decay functions from

(Section 4-2-2). I present the result of comparison between the two exact reciprocal decay functions in Section 5-3-2, due to finer discretization used in the two-layered model. Before Section 5-3-2, the Exact reciprocal decay function 0 is omitted, and hence, the exact reciprocal decay function 1 is referred in this test and subsequent tests without its number.

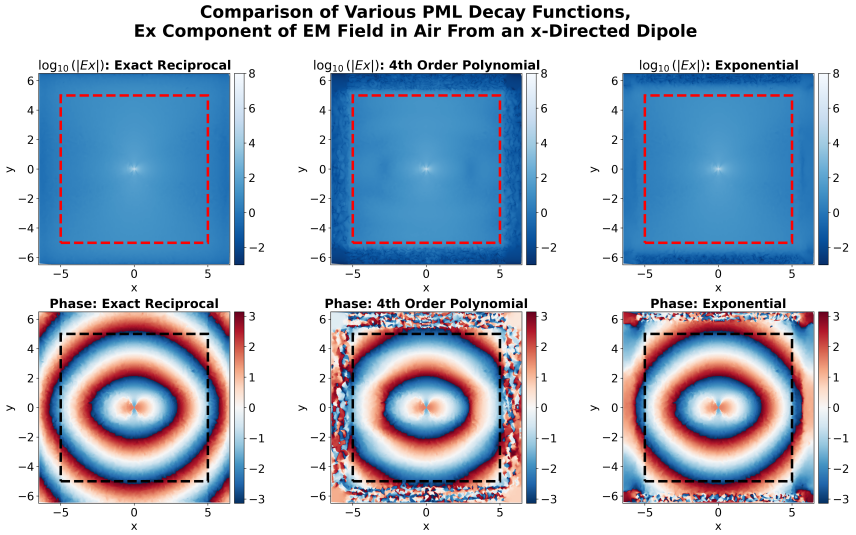

Figure 5-2: Whole-Space Air Model: $x-y$ plane cross-section at the origin, E_x field component comparison of various PML decay functions γ.

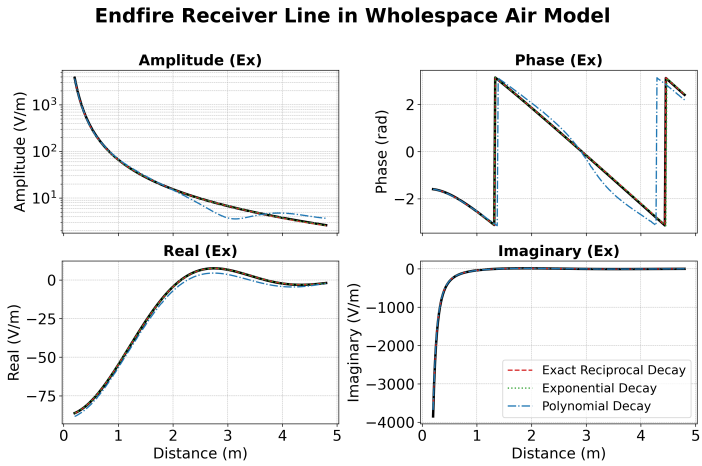

Figure 5-3: Whole-Space Air Model: E_x field component along the endfire receiver line for various PML decay functions γ.

Qualitatively, the exponential and the exact reciprocal decay functions are able to evaluate wave propagation with a smooth decay without noticeable reflections. Out of all three of simulated test cases, the polynomial decay function struggles to effectively eliminate reflections from the inner PML boundary, as is observable from the increased phase mismatch closer to the inline boundary of the simulation domain (along $\pm x$ axis). Its phase cross-section also shows that there is a lot of phase noise within the PML region, while the other two have less.

This makes it clear that more tuning is required if the PML is to be used with the polynomial decay function, while the Exact Reciprocal decay function required no tuning of parameters.

To quantitatively understand how well each decay function is performing, Figure 5-3 shows the x component of the electric field over a line of receivers in the endfire direction, while Figure 5-4 shows the exact error values in each field component. These receivers located between 0.2 m to 4.8 m from the source, at 0.001 m below the source. There are 256 total receivers, with equal spacing between them. The analytical solution is also evaluated at the same coordinates such that no interpolation is required.

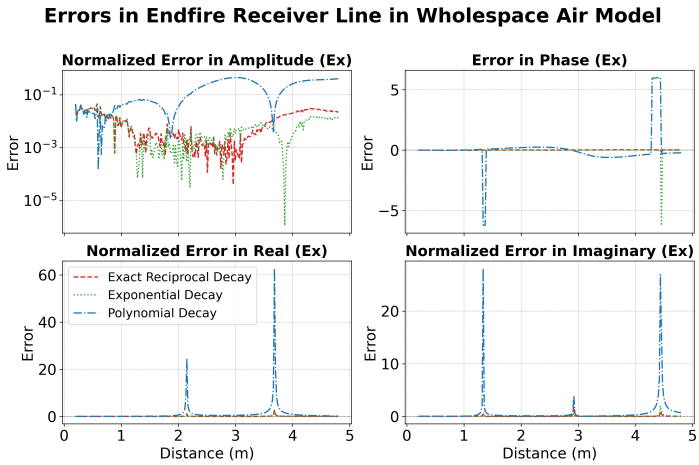

Figure 5-4: Whole-Space Air Model: Error in E_x field component along the endfire receiver line for various PML decay functions γ.

Inspecting Figure 5-3 makes it clearer that the polynomial decay function gives the most erroneous field values, while the others generally follow the same curve as the analytical solution. This could be attributed to the fact that the polynomial decay function as mentioned in Section 4-2-2 is orders of magnitude above the other two decay functions. This could cause high impedance mismatch not only at Γ_{model}, but also within the PML, as is apparent in Figure 5-2. For the real and imaginary components of E_x field, I use the following error formulas:

1. **Normalized Real Component Error**: $\left|\frac{\text{Re}(E_{x,\text{elfe3D\_GPR}} - E_{x,\text{analytical}})}{\text{Re}(E_{x,\text{analytical}})}\right|$, where $\text{Re}(\cdot)$ denotes taking the real component of a complex number.
2. **Normalized Imaginary Component Error**: $\left|\frac{\text{Im}(E_{x,\text{elfe3D\_GPR}} - E_{x,\text{analytical}})}{\text{Im}(E_{x,\text{analytical}})}\right|$, where $\text{Im}(\cdot)$ denotes taking the imaginary component of a complex number.

The error in amplitudes for all decay function cases are higher near the end of the receiver line, potentially from the increased unstructured meshing at the Γ_{model} interface. Otherwise, between 1 and 3 metres, the magnitude of error in amplitude for exact reciprocal and exponential functions stay below $1e$-2, or 1%. The phase, real and imaginary error plots all show huge spikes in error at certain individual receiver sites. These can be likely attributed

to the sharp phase discontinuities as seen before in Figure 5-1. Even still, the errors at these sites are lower for exact reciprocal and exponential decays compared to the polynomial decay function.

Concluding the testing with the whole-space air model, elfe3D_GPR shows potential for promising accuracy using the exact reciprocal decay or the exponential decays. For the polynomial decay function, more tuning is necessary. For the exponential decay as well, tuning was performed specifically for this whole-space model. Hence, further tuning is required for geologically complex models. Consequently, the exact reciprocal decay function is used in all subsequent simulations. This is to ensure I address the critical parts of the work with sufficient rigor without over-engaging with PML tuning, when it is not necessary using the exact reciprocal decay function.

5-2 Half-Space Model

The half-space model introduces the interface between air and earth. The source is kept slightly above the air-earth interface, while the receiver points are slightly below it. It serves as a simplistic geological test that introduces the effects from direct air-wave, direct ground-wave, head-wave and propagating waves in air and earth. This model is insightful for initial testing of various theoretical PML configurations for GPR models as well (Section 4-3).

Table 5-2: Simulation parameters for the base half-space model.

Model Parameter		**Specification**	
Category	**Variable**	**Value**	**Units**
Domain Truncation	Extents in x-axis	$[-3, 3]$	m
	Extents in y-axis	$[-3, 3]$	m
	Extents in z-axis	$[-1.5, 3]$	m
Air-Earth Interface	Extents in x-axis	$[-3, 3]$	m
	Extents in y-axis	$[-3, 3]$	m
	z-axis value	0	m
Air Layer	$\{\varepsilon_r, \sigma, \mu_r\}$	$\{1, 1e\text{-}16, 1\}$	$\{-, S/m, -\}$
	Maximum Element Volume	$3.1820e\text{-}03$	m^3
	Maximum Edge Length	$\lambda_{\text{air}}/10$	m
Half-Space Layer	Extents in x-axis	$[-3, 3]$	m
	Extents in y-axis	$[-3, 3]$	m
	Extents in z-axis	$[-1.5, 0]$	m
	$\{\varepsilon_r, \sigma, \mu_r\}$	$\{4, 1e\text{-}4, 1\}$	$\{-, S/m, -\}$
	Maximum Element Volume	$3.9775e\text{-}04$	m^3
	Maximum Edge Length	$\lambda_1/10$	m
Source Antenna	Dipole Direction	$+x$-axis	–
	Extents in x-axis	$[-2.5, 2.5]$	mm
	Fixed y-axis value	0	m
	Height from Interface	2.5	cm
	Source Moment Magnitude I	1	A/m^2
	Source Frequency	100	MHz

Table 5-2: Simulation parameters for the base half-space model (continued).

Model Parameter		Specification	
Category	**Variable**	**Value**	**Units**
Endfire Receiver Line	Number of Receivers	256	–
	Start and End x-values	$[0.2, 4.8]$	m
	Depth from Interface	1.25	mm
Broadside Receiver Line	Number of Receivers	256	–
	Start and End y-values	$[0.2, 4.8]$	m
	Depth from Interface	1.25	mm
Oblique Receiver Line	Number of Receivers	256	–
	Start and End x-values	$[0.1414, 3.3941]$	m
	Start and End y-values	$[0.1414, 3.3941]$	m
	Depth from Interface	1.25	mm

Here, λ_1 corresponds to wavelength of the electric field at the given source antenna frequency in the half-space medium. As mentioned before, to check the accuracy of `elfe3D_GPR`'s results, I am using two semi-analytical approaches, one since they evaluate the solutions using numerical integration (Wait, 2013; Werthmüller, 2017). The quadrature approach was implemented in `MATLAB`, and for `empymod` I used their 2001-point filter designed for high frequency EM (Werthmüller et al., 2019).

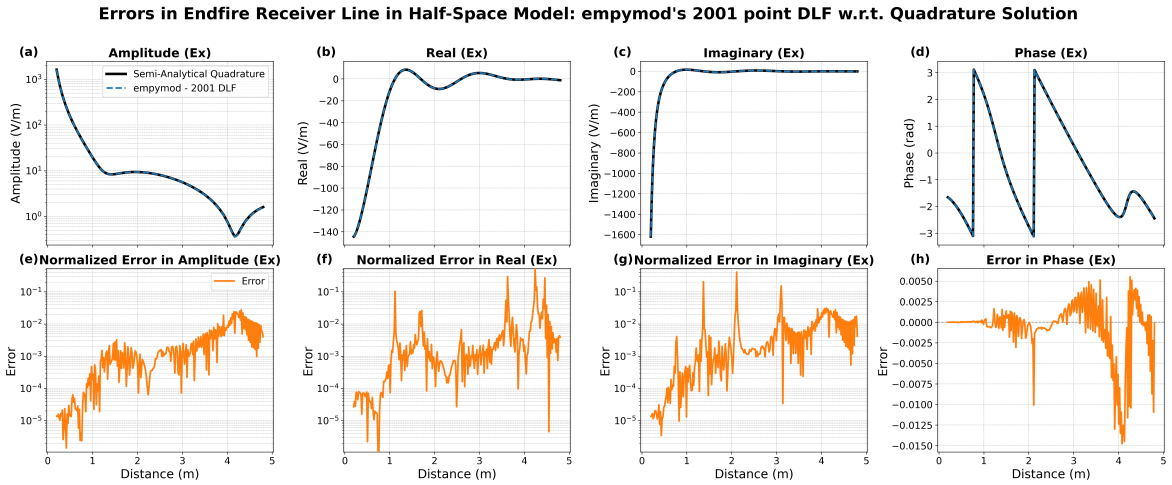

Figure 5-5: Half-Space Model: Comparison of E_x field along CMP-like receiver line of `empymod` with analytical solution. The data components are plotted in the first row and `empymod`'s error with respect to analytical solution are plotted in the second row.

Both solutions in Figure 5-5 give very close estimates. The maximum errors in real and imaginary components in `empymod`'s solution (Figure 5-5 (f,g)) are about 2 orders of magnitude higher than the maximum error in amplitude (Figure 5-5 (e)). The maximum amplitude is located near 4 m, where the absolute value is the lowest in the complete receiver line. Even then, it is close to 1%. The phase values are also very accurate. This comparison between two semi-analytical approaches is insightful to understand the numerical limits of estimating field values. For further comparisons, I choose the quadrature method as the reference solution.

5-2-1 Testing PML Wavenumber Approaches

Testing for the half-space model needs to begin with what wavenumber to use for scaling the decay function (Section 4-2-3). Each different PML wavenumber scaling approach as mentioned in Section 4-2-3 requires a unique combination of material parameters, discretization and scaling factor, as illustrated in Figure 5-6. These considerations are given in the table below:

Table 5-3: Description of PML approaches for the base half-space model.

Approach	$k_{\mathbf{PML}}$ **Used**	**PML Thickness**	**Max PML Element Edge Length**
Uniform $k_{\min}$ Stretch	$k_{\text{air}} := k$ of Air	$\lambda_{\text{air}}/2 = 1.5$ m	$\lambda_{\text{air}}/10$
Uniform $k_{\max}$ Stretch	$k_{\text{hs}} := k$ of Half-Space	$\lambda_1/2 = 0.75$ m	$\lambda_1/10$
Varying Stretch	k_{air} Above Air-Earth Interface, k_{hs} Below it	$\lambda_1/2 = 0.75$ m	$\lambda_{\text{air}}/10$ Above Air-Earth Interface, $\lambda_1/10$ Below

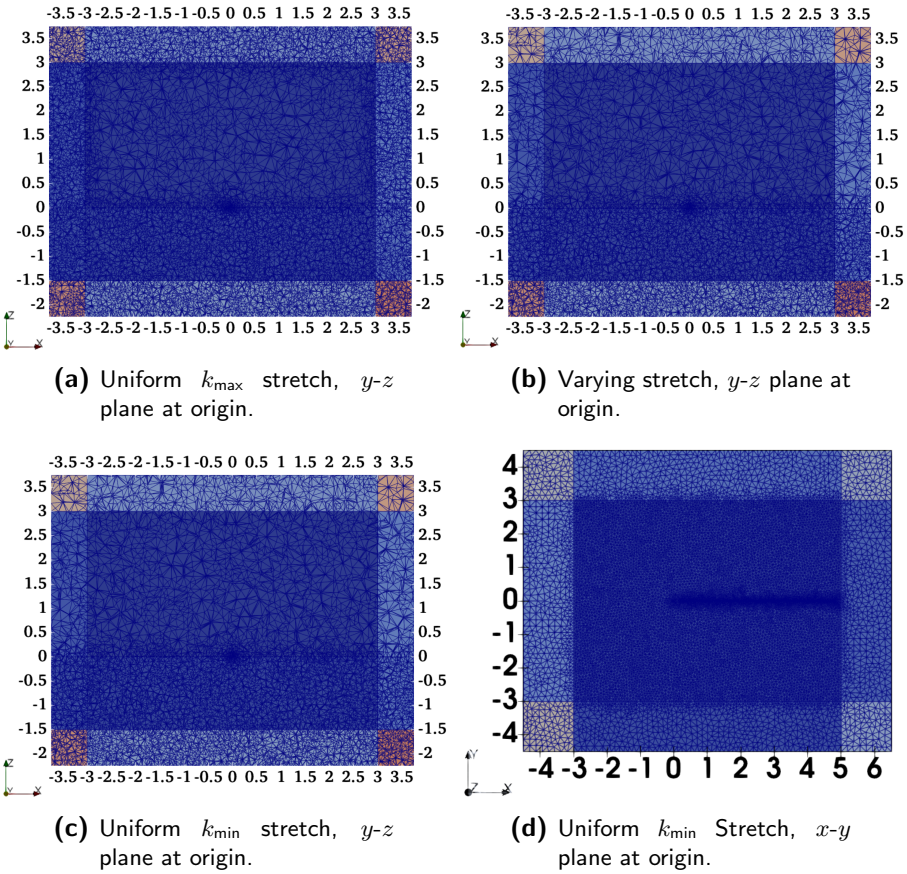

(a) Uniform $k_{\max}$ stretch, y-z plane at origin.

(b) Varying stretch, y-z plane at origin.

(c) Uniform $k_{\min}$ stretch, y-z plane at origin.

(d) Uniform $k_{\min}$ Stretch, x-y plane at origin.

Figure 5-6: Cross-sections of the half-space model for three PML wavenumber approaches.

As specified in Table 5-3, the uniform $k_{\min}$ stretch PML is the thickest one of the three (Figure 5-6c). However, since it is also the coarsest, it has the lowest number of degrees of

freedom of the three cases. The uniform $k_{\max}$ stretch approach (Figure 5-6a) has the most dense PML, due to the transition between coarse air region and dense uniform PML. The varying stretch PML has the same thickness as the uniform $k_{\max}$ PML (Figure 5-6b), and its tetrahedra volumes are constrained depending on the layer next to the PML. I did not choose a greater thickness for the varying stretch as with Figure 5-6c, due to its mesh having a prohibitively high number of DOFs in the PML relative to the other two wavenumber scaling approaches.

After simulating all test cases using the half-space model described in Table 5-2, the corresponding semi-analytical analytical solutions were generated. The endfire receiver-line curves for the E_x field data from the different approaches is shown in Figure 5-7. In Figure 5-8, the corresponding `elfe3D_GPR` errors are illustrated with respect to the semi-analytical reference. The receiver line is restricted to a length of 1 m to emphasize the region of interest near the source antenna, which is characteristic of common-offset (CO) ground-penetrating radar (GPR) acquisition at 100 MHz.

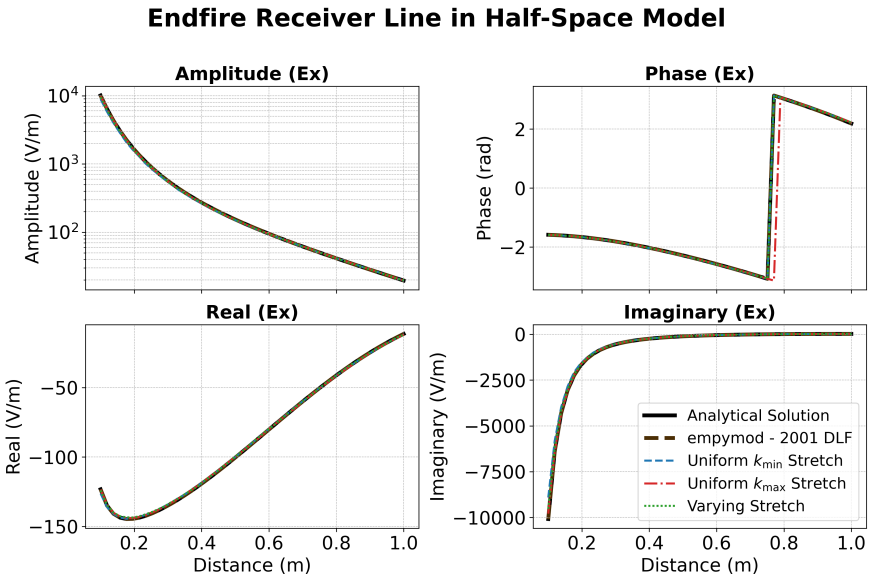

Figure 5-7: Half-Space Model: Testing Wavenumber approaches, within CO-like distances. Comparison of E_x field along with the two semi-analytical solutions.

It is clear that none of the approaches produce outright outliers compared to the semi-analytical solutions, except a phase shift at one receiver site by the uniform $k_{\max}$ stretch solution. Moreover, `empymod`'s solution matches the analytical solution very well and they are essentially overlapping.

Figure 5-8 shows that the best performing wavenumber approach appears to be uniform stretch with $k_{\max}$ being used as the scaling factor with the decay function. Its maximum error for the amplitude is at 0.1 m, of value 2.9%. It's average amplitude error is quite low, at 0.96%, with a standard deviation of 0.68%. While it is also the only one with a noticeable phase shift compared to analytical solution, it is only one receiver out of the 48 where the arbitrarily high phase error exists which I have clipped out for easier inference. As in Figure 5-1, this is due to an error in the sharp jump in phase, which is acceptable due to the finite

sizes of the field evaluations. The second best results are from the varying stretch approach, with a maximum of 5.46% error, mean of 1.16% error and standard deviation of 1.07% error. The uniform stretch with $k_{\min}$ has a maximum of 11.65% error, with a mean error of 2.56% and a standard deviation of 2.68%.

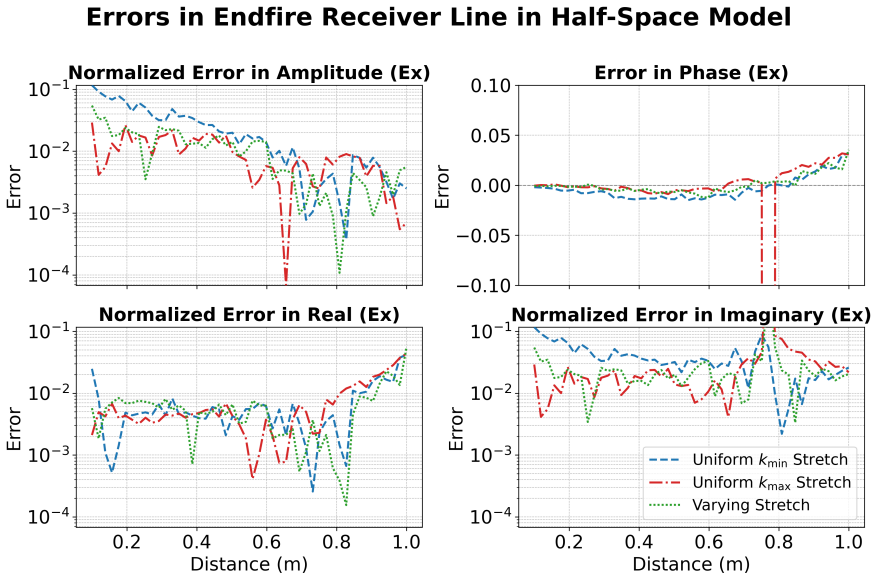

Figure 5-8: Half-Space Model: Error for Wavenumber approaches in the E_x field data, within CO-like distances.

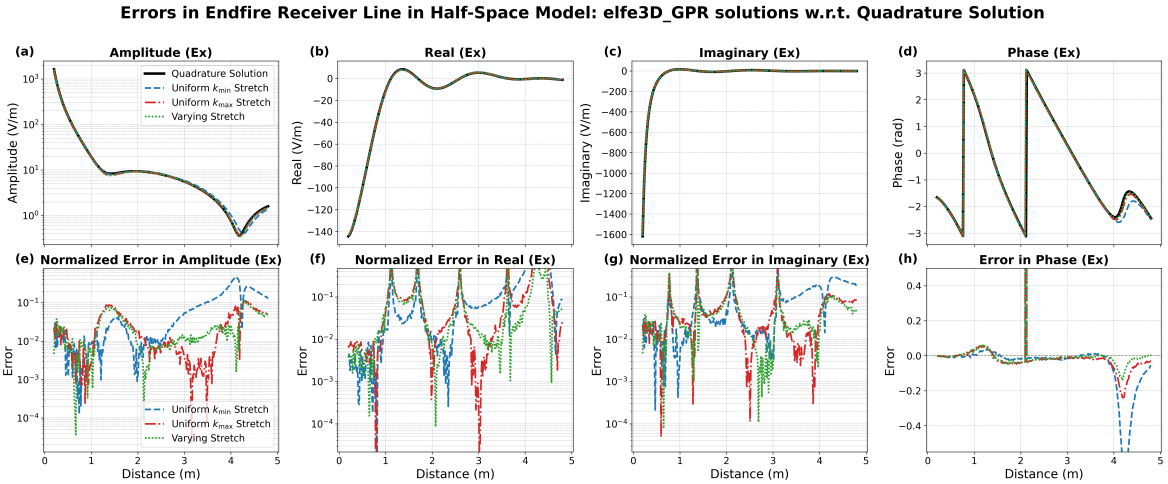

Figure 5-9: Half-Space Model: Testing Wavenumber approaches, with CMP-like distances. Comparison of E_x field along with the two semi-analytical solutions.

It is also worth noting that except for numerical percent advantages in amplitude, there is no clear best performing approach for the complete receiver line. In an attempt to identify this with a more extreme simulation domain, I repeat the same experiment with a longer receiver line corresponding to Common Midpoint (CMP) like acquisition distances, with its

result shown in Figure 5-9. This corresponds to longer extent in the x-axis direction, now going from -3 to 5 m, while 256 receivers lie between 0.2 and 4.8 m.

The error at distances greater than one meter are very high for the uniform air-like stretch, with a maximum amplitude error of 47.81%. The other two methods maximize at close to 11% amplitude error with average error of around 2.75 %. The uniform earth-like stretch approach performs the best here as well, with quite low errors around 2.5 to 3.5 metres. All combined, these results particularly indicate that numerical dispersion is affecting the simulation results, intensifying more the longer the wave propagates as it travels away from the source.

It should also be noted here that several different configurations of PML thickness, source length and receiver depths, x, y, z extents were tested here before the base model was decided upon. A box of much finer discretization around the source and receiver line was also tested in effort to improve the solution accuracy without considerable improvements. However, that method failed due to worsening of mesh quality from the box bringing worse structure to the mesh. Ultimately, the base model represents the best set of parameters that I found when the mesh elements were constrained to a maximum edge length of $\lambda_{medium}/10$, as per the medium in the simulation domain and the PML approach (Table 5-3).

With the half-space model, it is made clear that the wave propagation from all various air-earth interface effects can be captured effectively with uniform $k_{\max}$ stretch PML approach. However, comparing my PML thickness to ones implemented by (Ozgun et al., 2023; Warren, Giannopoulos, & Giannakis, 2016), it is clear that my PML is much thicker in terms of wavelength of the wave at centre frequency in air. Since no iteration of this model has allowed me to have a similarly thin PML, for testing with two layered model below, I use a finer discretization of $\lambda_{\text{medium}}/20$. Since an adequate performance has been achieved with the half-space model using the uniform $k_{\max}$ approach, it is not necessary to test it further.

5-3 Two-Layered Model

To make `elfe3D_GPR` truly applicable for all GPR problems where multiple geophysical layers and anomalies exist, this two-layered model is extensively tested. It helps identify more subtle considerations that must be made for accurate results with more general geological models. The model's parameters are described in Table 5-4.

Table 5-4: Simulation parameters for the base two-layered model.

Model Parameter		Specification	
Category	**Variable**	**Value**	**Units**
Domain Truncation	Extents in x-axis	$[-0.3, 1.3]$	m
	Extents in y-axis	$[-0.3, 0.3]$	m
	Extents in z-axis	$[-1.1, 0.3]$	m
Air-Earth Interface	Extents in x-axis	$[-0.3, 1.3]$	m
	Extents in y-axis	$[-0.3, 0.3]$	m
	z-axis value	0	m

Table 5-4: Simulation parameters for the base two-layered model (continued).

Model Parameter		Specification	
Category	**Variable**	**Value**	**Units**
Air Layer	$\{\varepsilon_r, \sigma, \mu_r\}$	$\{1, 1e\text{-}16, 1\}$	$\{-, S/m, -\}$
	Maximum Element Volume	$3.1820e\text{-}03$	m^3
	Maximum Edge Length	$\lambda_{air}/20$	m
Subsurface Layer 1	Extents in x-axis	$[-0.3, 1.3]$	m
	Extents in y-axis	$[-0.3, 0.3]$	m
	Extents in z-axis	$[-1.0, 0.0]$	m
	$\{\varepsilon_r, \sigma, \mu_r\}$	$\{4, 1e\text{-}4, 1\}$	$\{-, S/m, -\}$
	Maximum Element Volume	$3.9775e\text{-}04$	m^3
	Maximum Edge Length	$\lambda_1/20$	m
Subsurface Layer 2	Extents in x-axis	$[-0.3, 1.3]$	m
	Extents in y-axis	$[-0.3, 0.3]$	m
	Extents in z-axis	$[-1.1, -1.0]$	m
	$\{\varepsilon_r, \sigma, \mu_r\}$	$\{9, 1e\text{-}3, 1\}$	$\{-, S/m, -\}$
	Maximum Element Volume	$1.1785e\text{-}04$	m^3
	Maximum Edge Length	$\lambda_2/20$	m^3
Source Antenna	Dipole Direction	$+x$-axis	–
	Extents in x-axis	$[-2.5, 2.5]$	mm
	Fixed y-axis value	0	m
	Height from Interface	2.5	cm
	Source Moment Magnitude I	1	A/m^2
	Source Frequency	100	MHz
Endfire Receiver Line	Number of Receivers	256	–
	Start and End x-values	$[0.2, 4.8]$	m
	Depth from Interface	1.25	mm

Here, λ_2 corresponds to wavelength of the electric field at the given source antenna frequency in the second subsurface layer. Similar to half-space model validation, for this two-layered model, I use the semi-analytical quadrature solution for reference.

The most interesting aspect to test with this model is how well reflections at material boundaries in the subsurface is captured by `elfe3D_GPR`, and how thick should the second layer be before the PML can be safely placed. Since the two layered model is closer to general subsurface conditions for GPR than the half-space model, I am also presenting more of the testing around truncation and source-receiver sizes.

5-3-1 Re-Testing PML Wavenumber Approaches

With the now smaller domain and much finer discretization of maximum edge length of $\lambda_{medium}/20$, I re-tested the different PML approaches for the base two-layered model, with the adjusted parameters described in Table 5-5, and their resulting simulation mesh illustrated in Figure 5-10.

Table 5-5: Description of PML wavenumber approaches for the base two-layered model.

Approach	**k_{PML} Used**	**PML Thickness**	**Max PML Element Edge Length**
Uniform $k_{\min}$ Stretch	k_{air}	$\lambda_{\text{air}}/10 = 0.3$ m	$\lambda_{\text{air}}/20$
Uniform $k_{\max}$ Stretch	$k_2 := k$ of Subsurface Layer 2	$\lambda_2/10 = 0.1$ m	$\lambda_2/20$
Varying Stretch	k_{air} Above Air-Earth Interface, k_1 Laterally Around the first subsurface layer, and k_2 below it.	$\lambda_2/10 = 0.1$ m	$\lambda_{\text{medium}}/20$ depending on medium of the PML element

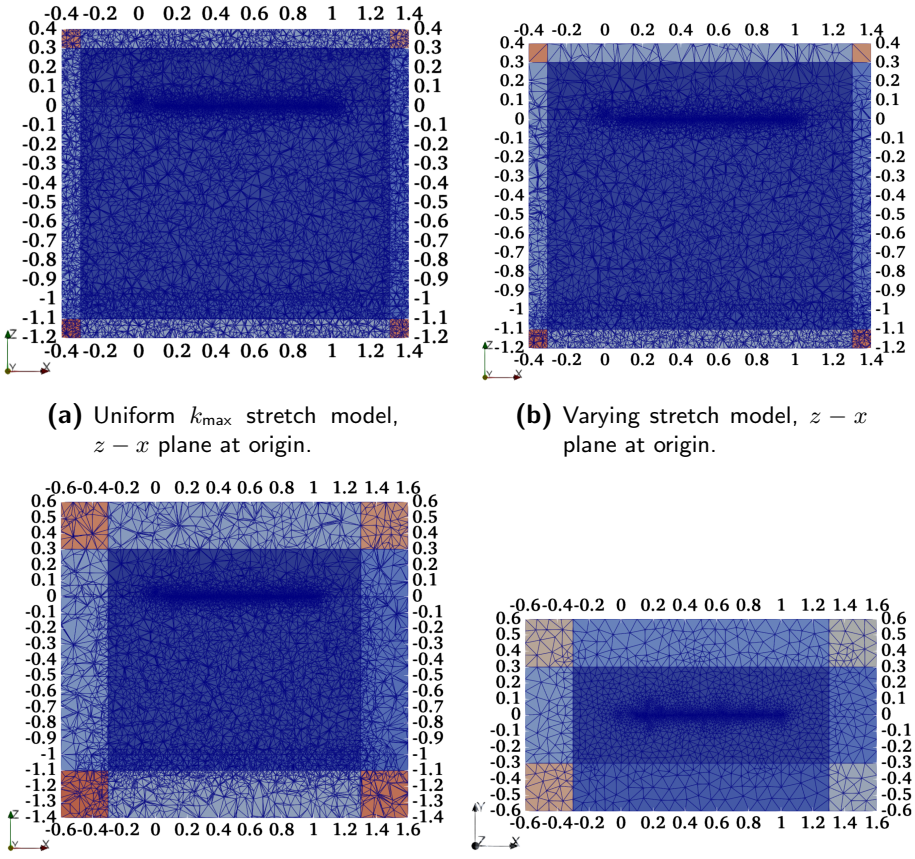

(a) Uniform $k_{\max}$ stretch model, $z-x$ plane at origin.

(b) Varying stretch model, $z-x$ plane at origin.

(c) Uniform $k_{\min}$ stretch model, $z-x$ plane at origin.

(d) Uniform $k_{\min}$ stretch model, $y-x$ plane at origin.

Figure 5-10: Cross-sections of two-layered models with different wavenumber approaches as described in Tables 5-4 and 5-5.

With the new finer discretization, there are significantly more elements per wavelength of the field. All of Figures 5-10a to 5-10c models are much smaller now compared to the models in haf-space (Figure 5-6), even in z-axis extents. Laterally, the model now is now not much more

than a strip of receiver line surrounded by the PML, as seen in Figure 5-10d and compared with Figure 5-6d. Hence, this allows to lower the degrees of freedom by a factor of around 9 times compared to the half-space model even though the subsurface layer 2 is included which has finer discretization than the discretization in the half-space (Tables 5-2 and 5-4).

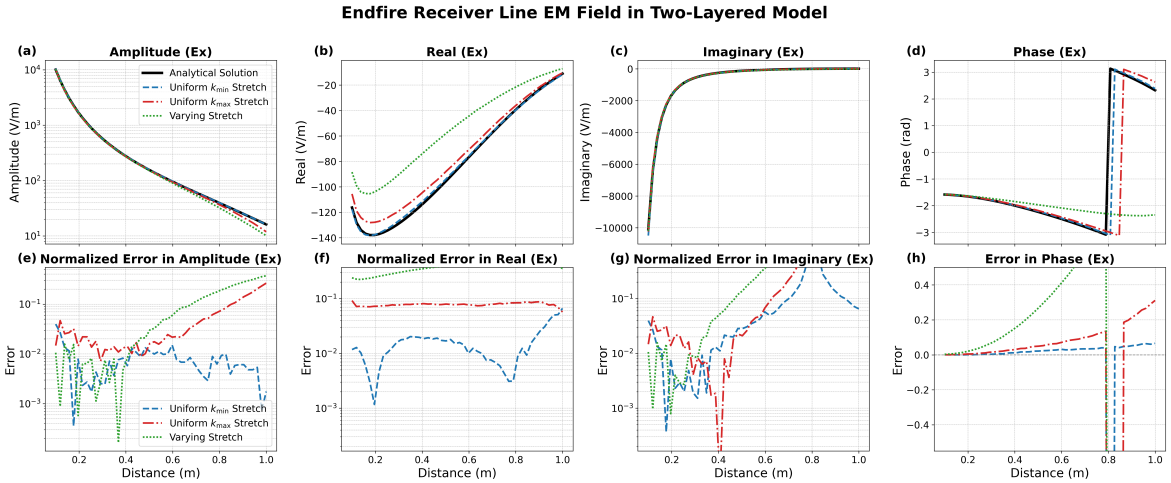

Figure 5-11: Two-Layered Model: Testing Wavenumber approaches, with CO-like distances. Comparison of E_x field along with the reference semi-analytical solution with field values in the top row and error in each approach in the bottom row.

Figure 5-11 shows the with this two-layered model, the uniform $k_{\min}$ stretch approach works better than the uniform $k_{\max}$ stretch approach, where the $k_{\max}$ approach is more inaccurate in amplitude plot (Figure 5-11 (e)), but significantly more so in real (Figure 5-11 (g)) and phase (Figure 5-11 (g)) plots. The clear worst performing approach here is with the varying stretch approach. Its real error plot is more than one order of magnitude worse (Figure 5-11 (f)), and its phase plots (Figure 5-11 (d,h)) show that it is unable to capture the wave propagation at all. This model proves clearly what Bérenger (2007) said about layered model PML (Section 4-2-3).

The PML approach with uniform stretching using $k_{\min}$ indeed shows great performance, with maximum amplitude error of 3.96%, an average of 0.80% along the receiver line, and standard deviation of just 0.65%. The discrepancy between $k_{\max}$'s superior results in the half-space model and $k_{\min}$'s results in the two-layered model can be attributed to the lower discretization used in the half-space model. The $k_{\max}$ approach makes sure that the entire PML domain is finer in discretization compared to wavelength in air, like in Figure 5-6. Moreover it has smoother gradients since the larger denominator makes the amount of stretch lesser. The increase in sampling from finer discretization is also more beneficial for impedance matching compared to a relatively coarse discretization. It also allows the higher gradient scaling of $k_{\min}$ to be accurately captured.

With this finer discretization, even though the discretization of PML region itself is coarser with larger domain in the $k_{\min}$ approach, the improvement between $\lambda_{\text{medium}}/20$ versus $\lambda_{\text{medium}}/10$ sampling allows more physically accurate wave propagation and absorption. This is further proven by how much smaller the domain and PML are now compared to the half-space model (Tables 5-3 and 5-5). Now, I can safely keep the PML at $\lambda_{air}/10 \approx 0.3$ m away

from the source. It is, therefore, absorbing the near field as well as the the propagating wavefront.

5-3-2 Testing the Two Exact Reciprocal Decay Functions

The question still remains whether the exact reciprocal decay function should start with zero at Γ_{model}, or if a start from a finite value works (Section 4-2-2). To address this, I simulate both options of the exact reciprocal decay function using the two-layered model of Table 5-4 with uniform k_{min} scaling.

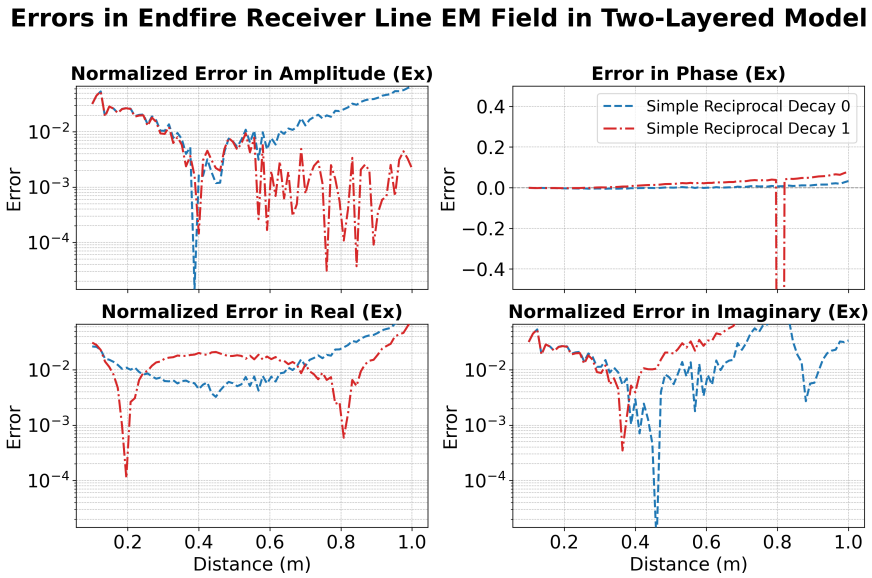

Figure 5-12: Comparing the error between the two exact decay functions.

It is interesting to note from Figure 5-12 that the exact reciprocal decay function starting with a finite value shows better agreement to the analytical solution, than the decay function starting with zero at Γ_{model}. This is unexpected behavior, because an abrupt increase in complex stretching could create numerical reflections. Yet, the result from Figure 5-11 clearly shows that using the exact decay function with finite start performs well. One possible explanation could be that due to function 1's larger attenuation values versus function 0 from the absence of $1/l$ term (Section 4-2-2), it effectively decays outgoing waves within the PML region without creating numerical reflections back into the model domain. Whereas, due to the lower attenuation values in function 0, even if the impedance is better matched at the start of PML region, non-trivial numerical reflections happen at Γ_{total} and reach the model domain to create errors.

Moving forward with the tests, I choose to continue using the un-modified exact decay function as used by Ding et al. (2025) and Feng, Ding, and Wang (2019).

5-3-3 Testing Broadside Response

Most of my tests in this thesis considered the endfire response. However, broadside response is a crucial component of GPR imaging. Hence, in this test, I model the broadside response in Figure 5-13 using the same two-layered model of Table 5-4, with the exception that the dipole is oriented in $+y$-axis direction. This required re-meshing the domain to align the elements near the source region as per the new dipole direction.

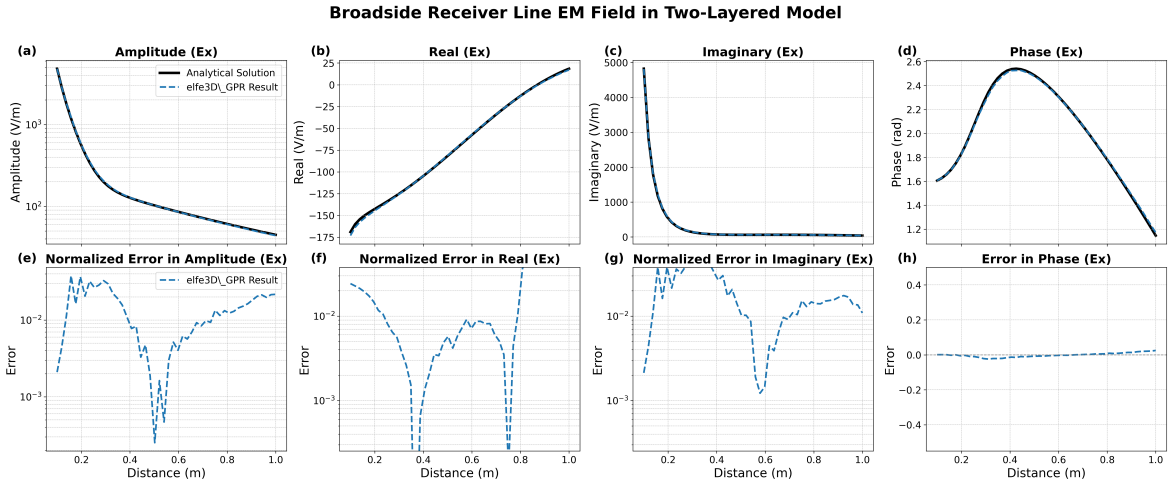

Figure 5-13: The two-layered model broadside E_x field.

As expected, the broadside field is also being captured well by the same parameters as the uniform stretch $k_{\min}$ approach (Table 5-5). The error range in amplitude and phase (Figure 5-13 (e,h)) are comparable to the range of error obtained in the corresponding endfire response (Figure 5-11(e,h)) with the uniform $k_{\min}$ approach. Hence, it is be inferred that the PML designed and discretization approach is not specific to angular orientation.

With the combination of tests in Sections 5-3-1 to 5-3-3, I have illustrated how well the exact PML implementation with $k_{\min}$ performs for layered media, with a very small domain and $\lambda/20$ maximum tetrahedral edge lengths. Now, I conduct parametric testing of key modelling parameters to check their influence on accuracy.

5-3-4 Testing PML Thickness

This set of tests uses the same base two-layered model (Table 5-4), while varying only the PML's thickness defined as λ_{air}/f_t, where f_t is a thickness factor number in range $[10, 25]$. Figure 5-14 shows error statistics of these simulations as a function of PML thickness.

From all four field components in Figure 5-14, it is apparent that the general trend is of increasing error with reducing PML thickness. Interestingly, the minimum of amplitude error is not at PML of thickness $\lambda/5$, rather at $\lambda/10$, albeit the difference is small. Such differences could be attributed how `tetgen` generated mesh are not simply adding more structured blocks to the existing PML, rather the elements are re-defined for each new PML. Therefore, the mesh quality is not linearly increasing with more elements.

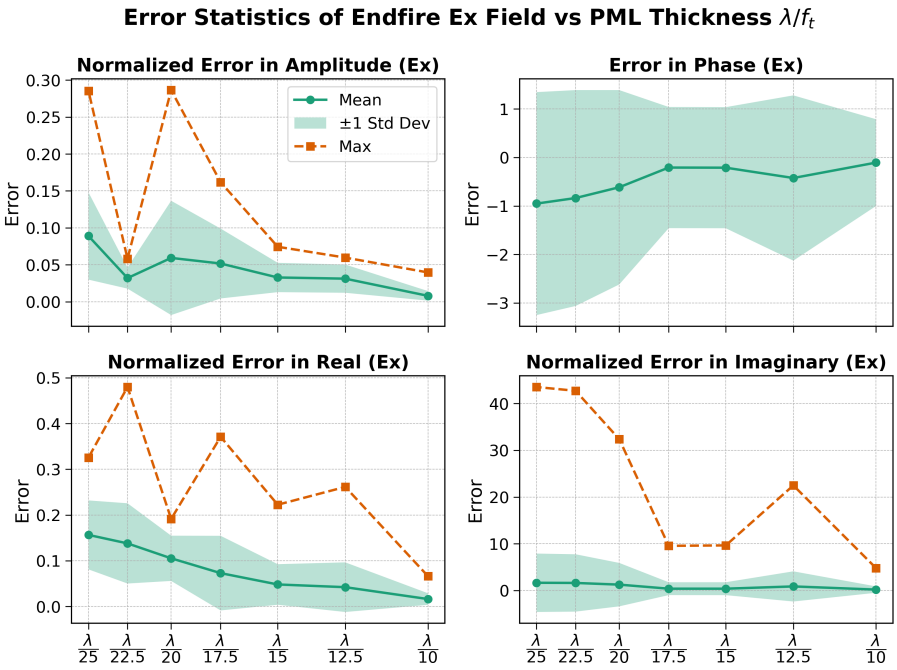

Figure 5-14: Two-Layered Model: Errors in Various PML Thicknesses λ_{air}/f_t.

In PML thinner than $\lambda/10$, the error in all four plots increases, until it reaches $\lambda/22.5$. It is possible that numerical dispersion or improper absorption experienced in the thinner PMLs somehow got destructively interfered using the $\lambda/22.5$ thick PML. Unfortunately, this is an outlier to the general trend, and hence, should not be used as a good choice for PML thickness. Moreover, plotting the maximum error in phase is not needed because it will always be a value close to 6 owing to the sharp phase shifts from $-\pi$ to π or vice versa as was the case in Figure 5-4.

5-3-5 Testing Source Discretization

This set of tests uses the same base two-layered model (Table 5-4), while varying only the source length and the receiver triangle edge lengths by the same factor f_{sr}, where f_{sr} is a discretization factor in the range $[100, 500]$. Figure 5-15 shows error statistics of these simulations as a function of source and receiver discretization.

Most source and receiver discretization options appear to have good agreement with the analytical solution, as is apparent from the mean and standard deviations in all four aspects of field values. However, the maximum error in amplitude follows a nearly steady decline, with close minima at $\lambda/250$ (4.43%) and $\lambda/500$ (3.96%). However, the real and imaginary maximum error trends do not follow any apparent pattern. This implies that any discretization factor higher than 250 could be a valid choice if modelling a point source. The mesh quality a and hence the simulation accuracy could vary differently for different geological models.

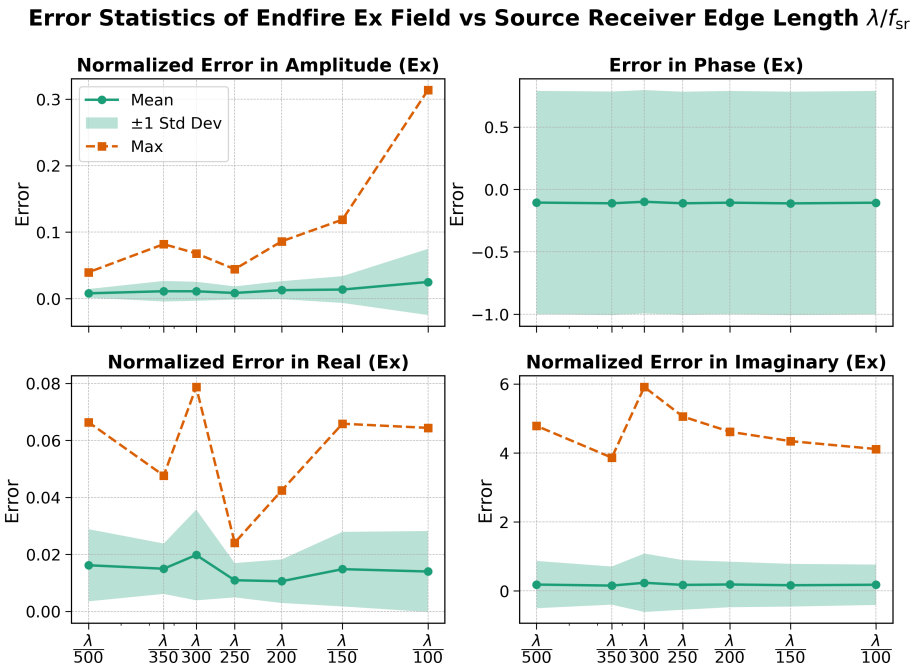

Figure 5-15: Two-Layered Model: errors in various source and receiver discretization, varied by factor f_{sr}.

5-3-6 Testing Domain Truncation

This set of tests uses the same base two-layered model (Table 5-4), while varying only the x and y axes extents, which define the distance from the source antenna's midpoint and the farthest receiver to the PML boundary. The truncation distance is set as $\lambda_{\text{air}}/f_{\text{xy}}$, where f_{xy} is a truncation factor varied in the range $[10, 25]$. For each value of f_{xy}, the x-axis extent is adjusted so that the space between the source midpoint and the nearest PML boundary, as well as the space between the farthest receiver and its nearest PML boundary, is $\lambda_{\text{air}}/f_{\text{xy}}$. The y-axis extents are changed proportionally using the same factor. All other parameters are kept the same as in Table 5-4. Figure 5-16 shows error statistics of these simulations as a function of the domain truncation factor.

The amplitude, phase and real component plots show closely linear increase in error as the domain is shrunk around the source and receivers. This could imply that making the domain too thin makes it lose valuable wave propagation information. Hence, for usage with different models, it should be tested parametrically how much extent is required for sufficient accuracy.

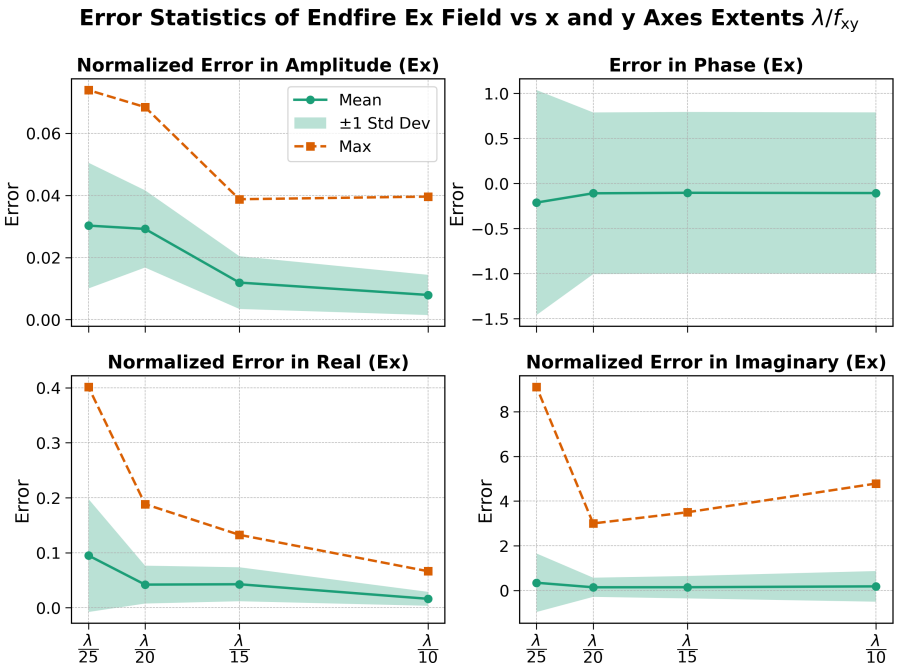

Figure 5-16: Two-Layered Model: errors in domain truncation options, varied by factor f_{xy}.

5-3-7 Testing Thickness of Second Layer

This set of tests uses the same base two-layered model (Table 5-4), while varying only the thickness of the second subsurface layer, defined as λ_2/f_z, where f_z is a thickness factor varied in the range $[1, 20]$. Knowing this could be very useful for limiting DOFs, since the region below the lowest geological interface is not of significant interest. Figure 5-17 shows error statistics of these simulations as a function of the second layer's thickness.

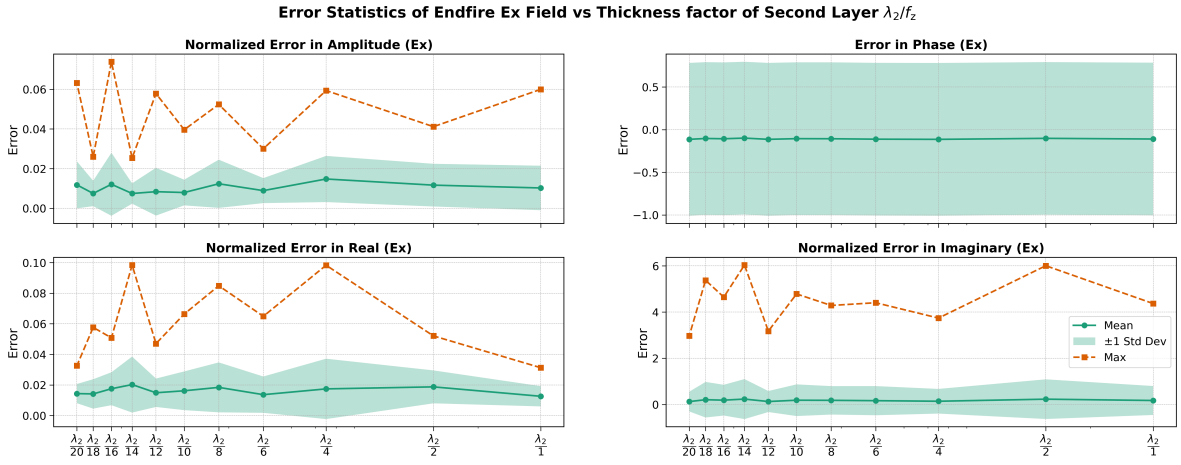

Figure 5-17: Two-Layered Model: Errors from Varying Thickness of Second Layer, varied by factor f_z.

Upon inspection, there seems to be no apparent pattern to how thin the second layer can be. Amplitude errors are nearly oscillating from low error to high error between each thickness option. Phase and imaginary component errors are nearly constant, and real component error is at its lowest at the thickest and the thinnest options. With such ambiguity, factor f_z should be carefully chosen by testing a few different options before finalizing the accuracy of elfe3D_GPR's results.

5-3-8 Testing Wideband Capability

elfe3D was designed to simulate multiple frequencies with the same mesh. This could be inconvenient for wideband simulation if the sampling factor of $\lambda_{\text{medium}}/x$, $\forall x > 10$ is not satisfied for any frequency in the band of frequencies with a sufficiently thick PML. Hence, to test how accurately the wideband simulations could be conducted, I simulate the two layered model response for frequencies 50 MHz and 150 MHz. This choice comes from the choice of -3dB bandwidth from a centre frequency of 100 MHz. I simulate these frequencies using two different simulation mesh each. One, the **Base Mesh** (Table 5-4) only changing the source frequency. Two, a **Frequency Specific Mesh** scaled in mesh volume constraint, source length, buffer space around source and receiver line before reaching PML, and PML thickness based on the frequency.

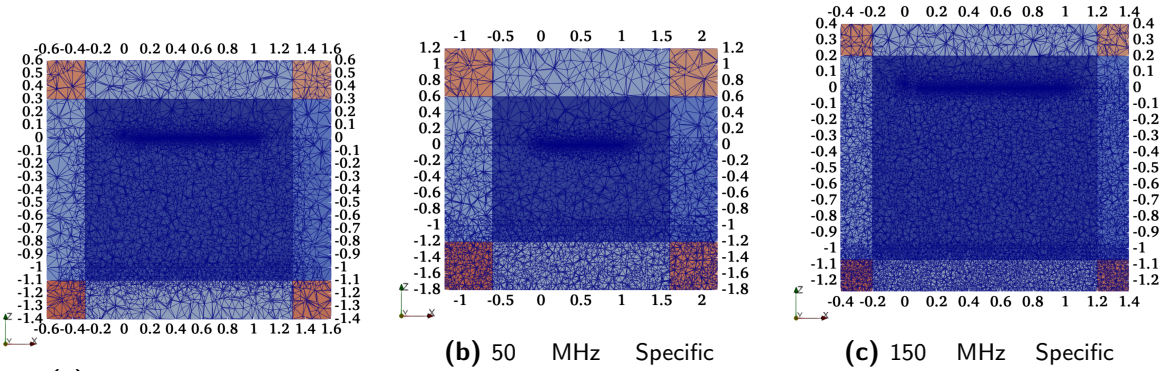

(a) 100 MHz Base Mesh

(b) 50 MHz Specific Mesh

(c) 150 MHz Specific Mesh

Figure 5-18: Two-layered models for different frequencies, $y - z$ cross-sections.

From the cross-section images of the models in Figure 5-18, it is clear that the 50 MHz specific mesh has a biggest domain and PML mesh, due to larger wavelength (Figure 5-18b). However, the wavelength allows us to correspondingly relax mesh element volumes compared to 100 MHz (Figure 5-18a). For 150 MHz, it is the exact opposite, with a thinner domain and PML, but denser mesh (Figure 5-18c). All three mesh illustrated here have nearly the same order of number of DOFs, ranging between $3e5$ and $4.5e5$.

From the 50 MHz endfire simulation results in Figure 5-19, it is evident that the base mesh that originally worked well for 100 MHz produces inaccuracies in the simulation for 50 MHz. On the other hand, the custom mesh follows the analytical curve well, which is expected. While this is contrary to what should be observed with oversampling from the base mesh, the PML is simply not thick enough for 50 MHz which was sufficient for 100 MHz. This is

similar in effect to what I observed in Figure 5-14, where PML of thickness less than $\lambda_2/15$ give much higher errors, except the outlier.

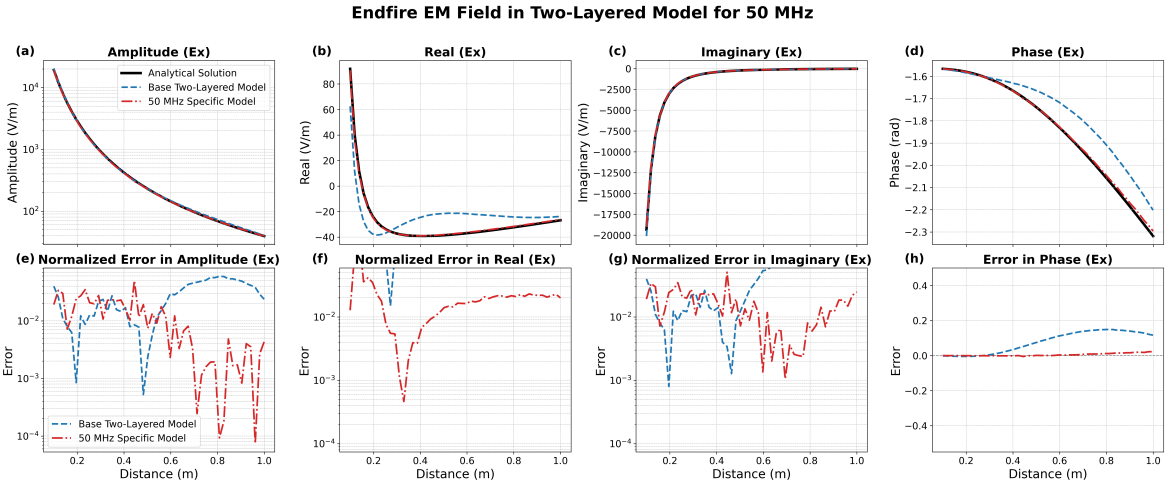

Figure 5-19: Two-Layered Model: 50 MHz endfire response of the E_x field and its error with respect to the semi-analytical quadrature solution.

The errors in field components along the receiver line give a clearer insight. The amplitude error for the custom mesh has a much lower average, especially in the second half of receiver line. Its maximum, mean and standard deviation of error are 5.00%, 1.23% and 1.13% respectively. Compared to this, the base mesh shows higher error along the receiver line overall, even though at the beginning it is not the case. Its maximum, mean and standard deviation of error are 5.92%, 2.76% and 1.81& respectively. More importantly, the custom mesh has much lower error in all of phase, real and imaginary components of the x component of the electric field.

I now repeat the experiment with 150 MHz using the base mesh (Figure 5-18a) and the 150 MHz-specific mesh (Figure 5-18c). From inspecting Figure 5-18c it appears that both simulations follow the analytical solution well. The base mesh does seem to generate a noticeable phase error at one receiver value, otherwise the solution for base mesh is not as clearly worse as it was for 50 MHz.

Here, the difference in amplitude error is not significantly different for both mesh. The custom mesh has maximum error of 4.15% with a mean of 2.82% while the base mesh has a maximum of 6.13 percent error with a mean of 1.90%. Hence, the custom mesh is still better, due to better discretization and a thinner but denser PML that is adjusted to its frequency. There are few high error locations in real and imaginary components that cause the phase errors, but otherwise, the remaining receivers do not have significant difference from analytical solution. This lower difference in error could be attributed to the thicker PML that is used in 100 MHz, even with coarser discretization.

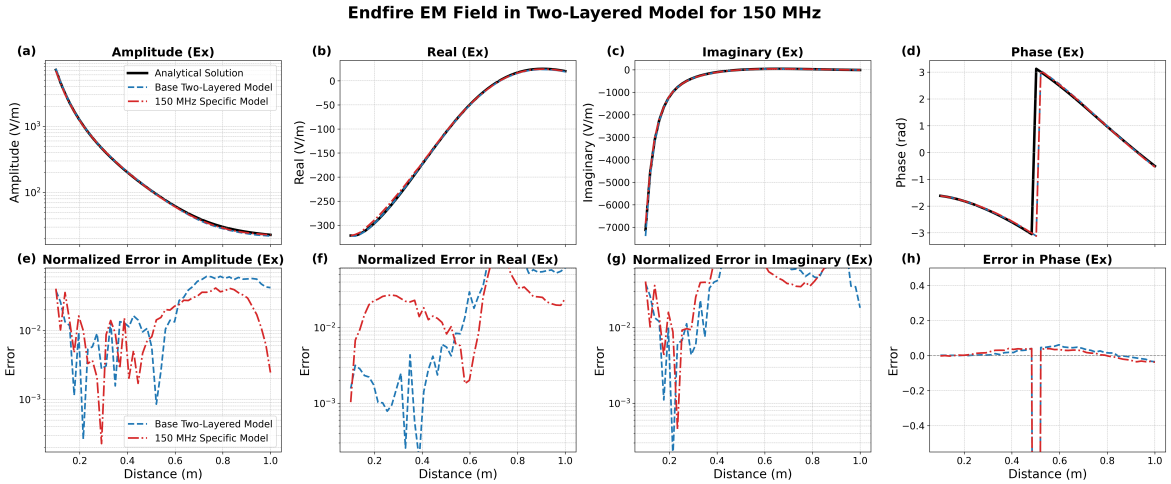

Figure 5-20: Two-Layered Model: 150 MHz endfire response of the E_x field and its error with respect to the semi-analytical quadrature solution.

Overall, wideband simulation with `elfe3D_GPR` is clearly possible. Understandably, for the limits of a wide band of frequencies, error with only one mesh designed for centre frequency of the band gives higher error than re-meshing the domain. However, errors from this base mesh is not exceedingly high such that completely new mesh will need to be generated for each individual frequency of interest in the wide band. Similar to my approach, three or so different mesh could be generated for across the spectrum, and the complete band could be divided into corresponding range of frequencies that are simulated using these mesh. Another approach could be to perform a few refinement steps with a PML thick enough that can accommodate the complete frequency band, if re-sized and re-meshed domains are not feasible due to memory constraints.

5-3-9 Testing Anomaly Detection

For an anomaly detection test, a slightly simplistic approach has been chosen. An anomalous box is embedded into the two-layered medium itself. The choice to choose a two-layered medium instead of half-space for the anomaly simulation is due to the fact that significantly higher amount of testing has been done on the two-layered model which would assure me of good accuracy of the model discretization and PML choices to compare against.

The anomaly has a relative permittivity of 20, and resistivity of $1e$-4. It is embedded into the first layer, between depths 0.5 m and 0.9 m from the air-earth interface, and x-extents of $(0, 0.375)$ m and y-extents of $(-0.15, 0.15)$ m. Since I did not have access to an alternative 3D frequency-domain solver, the receiver line plot is directly shown relative to the semi-analytical solution of the two-layered medium in Figure 5-21.

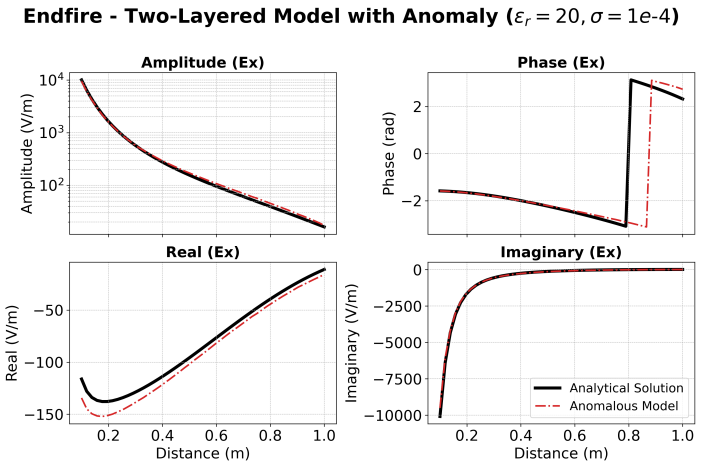

Figure 5-21: Comparing the anomaly E_x field with respect to the base two-layered model E_x field in endfire orientation.

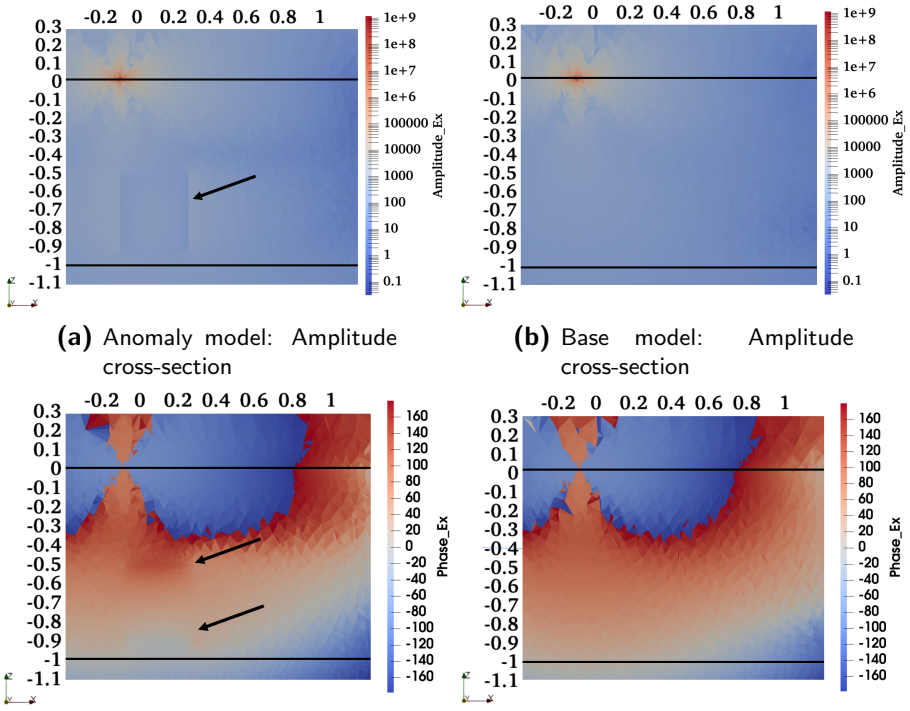

(a) Anomaly model: Amplitude cross-section

(b) Base model: Amplitude cross-section

(c) Anomaly model: Phase cross-section

(d) Base model: Phase cross-section

Figure 5-22: Comparison of cross-sections between the anomalous and normal two-layered models: (a) amplitude with anomaly, (b) amplitude without anomaly, (c) phase with anomaly, (d) phase without anomaly. The horizontal black lines are marked to show the air-earth interface and the subsurface layer interface, and the black arrows point to the field distribution around the anomaly.

The amplitude and imaginary components of the anomalous subsurface response in Figure 5-21 deviate very slightly compared to the base two-layered model response. The real and

the phase components of the E_x field show the most apparent change in comparison to the analytical solution.

To visually inspect what the field distribution looks like and if the anomaly produces reflections, I have taken $x-z$ plane cross-sections at origin of two simulations: the base two-layered model response from Figure 5-11 and table 5-4, and the anomalous subsurface model response. They have the same uniform $k_{\min}$ scaling of the exact decay function. Between Figure 5-22a and Figure 5-22b, the anomalous body is clearly visible with a sharp change in amplitude of the field around it at the exact coordinates of the anomalous box placement. Similarly, between Figure 5-22c and Figure 5-22d, the phase shift is observable along the vertical of the anomalous body. Both of these changes in Figure 5-22 indicate that the presence of the anomalous body has been captured well. Moreover, there is no observable numerical dispersion here.

5-4 Discussion on Capabilities of elfe3D_GPR

5-4-1 Establishing a Working PML

The first step towards a successful GPR simulation has been to establish a working PML implementation in the code of elfe3D_GPR. From whole-space air tests (Section 5-1-1), I established that the U-PML with the exact reciprocal decay function to be the best performing PML that requires no tuning at all to work well for homogeneous models. The exponential decay function gives a similar performance as the exact reciprocal decay function, but it requires tuning of the parameter a (Section 4-2-2). For all subsequent tests, I used the exact decay function using the U-PML. Comparison between the zero and non-zero iterations of the exact decay function (Section 4-2-2) using the two-layered model (Section 5-3-2) show interesting implications of the scaling factor and the amount of attenuation. Apart from Section 5-3-2, the exact reciprocal decay with non-zero minimum attenuation has been used throughout the thesis.

5-4-2 Half-Space Model and Element Edge and Volume Constraints

With the working PML, I have tested the influence of presence of synthetic subsurface layers in the simulation model. Here, the strategy has been to simulate various alternate choices of the wavenumber that are required to scale the decay function (Equation (4-10)). Starting with the half-space model and a maximum tetrahedral edge length of $\lambda_{\text{medium}}/10$, I concluded that this discretization factor was insufficient in accurately determining the right wavenumber choice.

One, due to the discretization factor, it was essential to use a very large domain, equal to at least one wavelength of the source frequency in both media of the model in all three dimensions (Table 5-2). This, I attribute to the need for coarser discretization to have minimum near-field effects such as evanescent waves before reaching the inner PML boundary. This misled me to infer that the best wavenumber approach to be of uniform $k_{\max}$ to efficiently absorb the outgoing waves. It is the thinner PML compared to the $k_{\min}$ approach (Table 5-3), but has uniformly halved edge length constraint. This success of $k_{\max}$ is due the fact that the

decay functions γ_i are inversely proportional to wavenumber, and that $k_{\max} > k_{\min}$. This means $k_{\max}$ causes lower attention compared to $k_{\min}$ per meter. Combined with the fact that the higher wavenumber requires finer mesh to discretize, the PML was more capable of absorbing outgoing waves compared to the other two approaches due to $k_{\max}$ approach having the smoothest gradients for capturing the decay function in the PML region.

Two, it also became necessary to use a very thick PML of $\lambda_{\text{air}}/2$ to get sufficient absorption. With the successful reported use of exact decay functions (Ding et al., 2025; Feng, Ding, & Wang, 2019; Ozgun et al., 2023), the PML have been extremely thin, of order $\lambda_{\text{air}}/10$, it was an insightful indication of the requirement for finer discretization.

5-4-3 Two-Layered Media Simulation and Wavenumber Scaling Approaches

This is established concretely from the test performed of the two-layered model and a maximum tetrahedra edge length of $\lambda_{\text{medium}}/20$. With the Section 5-3-1 group of simulations, I have been able to use a much thinner PML ($\lambda_{\text{air}}/10$) and much smaller domain compared to the half-space model (Table 5-4 and fig. 5-10). Here, it is evident that the wavenumber approach of uniform $k_{\min}$ stretch is the best performing PML, while the uniform $k_{\max}$ approach performs relatively worse. Even though the PML thickness used for $k_{\min}$ approach is larger than that of $k_{\max}$ approach (Table 5-5), due to coarser discretization required for sampling air-like stretch, the number of DOFs in $k_{\min}$ PML is smaller than that of $k_{\max}$ PML, making it more resource-efficient. The varying wavenumber approach performs the worst out of the three approaches, which is expected due to the mismatch in stretching that this enforces between the layers within the PML. Hence, the requirement of same stretch scaling as mentioned by (Bérenger, 2007) holds true.

5-4-4 Parametric Testing of Modelling Choices for Unstructured 3D Domains

Using this complete version of PML - with a combination of U-PML implementation in 3-D cartesian coordinates using the exact reciprocal decay function and a uniform wavenumber scaling of $k_{\min}$ - I conduct parametric tests of various simulation parameters. Testing for PML thicknesses (Section 5-3-4) progressively smaller than $\lambda_{air}/10$ indeed proved that it is unable to sufficiently capture the high gradients of the exact decay function to absorb all outgoing waves. Testing the source and receiver edge lengths progressively smaller (Section 5-3-5) also proved that for a point source approximation, the smaller edge lengths would estimate the field values with higher accuracy. Testing how thin the x and y extents can be before the PML is placed (Section 5-3-6) showed that a length of $\lambda_{\text{air}}/10$ is sufficient between the source and the inner PML boundary, and that a smaller simulation domain is not able to capture wave propagation in the near field well. Testing of the depth of the last layer below the lowest interface is more interesting (Section 5-3-7). It shows that there is no simple relationship between this thickness, and accuracy of the results, hinting at the limitations of the unstructured nature of mesh. Hence, different models will require different thicknesses of the final subsurface layer for good accuracy.

5-4-5 Wideband Simulation Capability and Constraint

For wideband testing, I simulated 50 MHz and 150 MHz using two approaches (Section 5-3-8). Here, I am able to prove that with a proper mesh directly designed for their specific frequencies, the simulation produces accurate results. With the same mesh as I used for 100 MHz, I get worse results for both ends of the spectrum (Figures 5-19 and 5-20). However, the difference between the custom mesh and the base mesh estimates for amplitude is not very high. With 150 MHz, the discretization of the base 100 MHz mesh limits accuracy. On the other hand, for 50 MHz, the PML thickness, more than discretization, is the limiting factor. These are both expected, as I have also established from the parametric testing of the 100 MHz mesh.

5-4-6 Anomaly Simulation

Finally, for anomaly detection characteristics, I simulated the base two-layered model with an embedding of an anomalous box of higher permittivity relative to the first subsurface layer. It is placed in the first subsurface layer, hence the contrast in material parameters is only in relative permittivity. From comparison with the semi-analytical solution of two-layered medium along endfire receiver line and 2D cross-sections of field distributions (Figures 5-21 and 5-22), it is apparent that the anomaly does produce reflections in the domain. However, for quantitative understanding of accuracy of the solution, a more comprehensive approach needs to be made.

5-4-7 Overall Capability of elfe3D_GPR

All considered, elfe3D_GPR is able to successfully simulate GPR forward problems of layered media, with an indication that anomalous subsurface models should be accurately modelled as well. The parametric testing shows that efficient domain truncation is also possible. This proves the effectiveness of my implementation of the PML using the exact decay function and the complex wavenumber scaling. The domain truncation and other parametric results, and the specific wideband tests show good potential for efficient frequency-domain wideband GPR simulations in 3D. Especially considering the parallelization that comes with frequency-independent simulations, and frequency-specific meshing strategies that exist, elfe3D_GPR is ready for simulating complex GPR forward and inverse problems.

Chapter 6

Conclusions and Future Work

In this thesis, I have worked on the development of `elfe3D_GPR` for modelling the 3D wide-band GPR forward problem in frequency-domain. This has been motivated by the fact that there are several frequency-domain specific forward modelling and inversion strategies that uniquely make use of frequency-domain characteristics of EM wave data. Throughout the development of `elfe3D_GPR`, I worked on modification of a CSEM diffusive-regime simulation program, `elfe3D`, to a GPR wave-regime simulation program. I used `elfe3D`'s implementation of first-order edge-based Nédélec basis 3D FEM on unstructured mesh as the foundation on which I developed `elfe3D_GPR`. Hence, relevant differences between CSEM and GPR modelling schemes using local methods such as FEM were first highlighted, which allowed me to implement the proper BVP for GPR wave simulation.

To efficiently truncate the GPR simulation domain, an absorbing PML boundary has been studied and implemented. The U-PML formulation has been implemented into `elfe3D_GPR` using an exact decay function, and tested for layered and anomalous subsurface. The use of U-PML and exact reciprocal decay function proved to be the most efficient method for absorbing boundary implementation, requiring no tuning of hyper-parameters that are characteristic of conventional decay functions. Moreover, key parameters of discretization and truncation have been parametrically studied for their effect on accuracy of results. It is found that using $\lambda_{\text{medium}}/20$ large elements edge length is a must for accurate GPR modelling in 3D, with the added advantage of being able to use a very thin PML of $\lambda_{\text{air}}/10$ and possibly thinner. The exact decay function allows a very remarkable absorption profile, even with the PML placed very close ($\lambda_{\text{air}}/10$) to the source and receivers. This has allowed very efficient modelling of 2.5D layered models, and an anomalous synthetic test case, using the $k_{\min}$ scaling approach to PML definition.

For wide-band capability testing, testing with 50 MHz and 150 MHz sources was conducted on two meshes. One was the same two-layered model as used for 100 MHz, as well as a custom model re-scaled and re-meshed for each frequency. While the custom mesh performed very well, the base two-layered model still gave reasonable accuracy. This implies that wide-band simulations in frequency-domain should not require extensively prohibitive re-scaling and re-meshing for each sampled frequency in the complete spectrum of frequencies. Only a few well-

chosen frequencies to design the mesh will be needed. During my work on converting `elfe3D` into `elfe3D_GPR`, few difficulties were encountered during PML implementation. Primarily, there were difficulties in implementing a SC-PML with first-order tetrahedral edge-based FE which has been mentioned.

In conclusion, the wide-band capable 3D GPR forward simulation code of `elfe3D_GPR` in frequency-domain with U-PML and exact decay function will serve as a strong foundation for advancing wide-band GPR modeling in frequency-domain. Hence, a large scope of future work exists. First and foremost, more realistic geophysical model tests should be performed for benchmarking performance along with adaptive refinement. In terms of user-friendliness of `elfe3D_GPR`, its high-performance Fortran forward solver can be wrapped into a Python or Julia environment along with mesh generation from `tetgen`, or possibly other software, for seamless GPR modelling experience for users. Extending `elfe3D_GPR` to include a dedicated wide-band re-meshing algorithm would be the first step in improving its usability for more realistic wide-band GPR simulations. Moreover, domain decomposition strategies designed for different bands of frequency in the wide-band can be implemented in `elfe3D_GPR` to further reduce computational cost. More significantly, `elfe3D_GPR`'s workflow needs only to be coupled with an optimization code for performing inversions. Hence, frequency-domain full-waveform inversions in 3D for wide-band GPR is now possible to implement using `elfe3D_GPR`.

References

Abenius, E., Edelvik, F., & Johansson, C. (2005). Waveguide truncation using upml in the finite-element time-domain method.

Ahrens, J., Geveci, B., & Law, C. (2005). Paraview: An end-user tool for large data visualization. *The visualization handbook*, *717*(8). https://api.semanticscholar.org/CorpusID:56558637

Amestoy, P. R., Duff, I. S., L'Excellent, J.-Y., & Koster, J. (2000). Mumps: A general purpose distributed memory sparse solver. *International Workshop on Applied Parallel Computing*, 121–130. https://dl.acm.org/doi/abs/10.5555/645782.666826

Anderson, R., Andrej, J., Barker, A., Bramwell, J., Camier, J.-S., Cerveny, J., Dobrev, V., Dudouit, Y., Akkerman, I., Kolev, T., Pazner, W., Stowell, M., Tomov, V., & ... (2021). MFEM: A modular finite element methods library. *Computers & Mathematics with Applications*, *81*, 42–74. https://doi.org/10.1016/j.camwa.2020.06.009

Annan, A. (2002). Gpr—history, trends, and future developments. *Subsurface sensing technologies and applications*, *3*(4), 253–270. https://doi.org/https://doi.org/10.1023/A:1020657129590

Annan, A. (2005). Ground-penetrating radar.

ANSYS, Inc. (2025). *Ansys hfss* (Version 2025 R1). https://www.ansys.com/products/electronics/ansys-hfss

Arndt, D., Bangerth, W., Davydov, D., Heister, T., Heltai, L., Kronbichler, M., Maier, M., Pelteret, J.-P., Turcksin, B., & Wells, D. (2019). The deal.ii finite element library: Design, features, and insights. *arXiv preprint arXiv:1910.13247*. https://doi.org/http://dx.doi.org/10.1016/j.camwa.2020.02.022

Atkinson, K., & Han, W. (2005). *Theoretical numerical analysis: A functional analysis framework*. Springer. https://doi.org/https://doi.org/10.1007/978-1-4419-0458-4

Balanis, C. A. (2012). *Advanced engineering electromagnetics*. John Wiley & Sons.

Benedetto, A., Tosti, F., Ciampoli, L. B., & D'Amico, F. (2016). Gpr applications across engineering and geosciences disciplines in italy: A review. *IEEE Journal of Selected Topics in Applied Earth Observations and Remote Sensing*, *9*(7), 2952–2965. https://doi.org/http://dx.doi.org/10.1109/JSTARS.2016.2554106

Berenger, J.-P. (1994). A perfectly matched layer for the absorption of electromagnetic waves. *Journal of computational physics*, *114*(2), 185–200. https://doi.org/https://doi.org/10.1006/jcph.1994.1159

Bérenger, J.-P. (2007). *Perfectly matched layer (pml) for computational electromagnetics* (Vol. 8). Springer. https://doi.org/https://doi.org/10.1007/978-3-031-74450-1

Bermúdez, A., Hervella-Nieto, L., Prieto, A., & Rodríguez, R. (2004). An exact bounded pml for the helmholtz equation. *Comptes Rendus Mathematique*, *339*(11), 803–808. https://doi.org/http://dx.doi.org/10.1016/j.crma.2004.10.006

Bramble, J., & Pasciak, J. (2007). Analysis of a finite pml approximation for the three dimensional time-harmonic maxwell and acoustic scattering problems. *Mathematics of Computation*, *76*(258), 597–614. https://doi.org/http://dx.doi.org/10.1090/S0025-5718-07-02037-6

Bramble, J. H., & Pasciak, J. E. (2012). Analysis of a cartesian pml approximation to the three dimensional electromagnetic wave scattering problem. *International Journal of Numerical Analysis and Modeling*, *9*(3), 543–561. https://doi.org/https://doi.org/2012-IJNAM-646

Butler, S. L., & Zhang, Z. (2016). Forward modeling of geophysical electromagnetic methods using comsol. *Computers & Geosciences*, *87*, 1–10. https://doi.org/http://dx.doi.org/10.1016/j.cageo.2015.11.004

Casati, D., Hiptmair, R., & Smajic, J. (2020). Coupling finite elements and auxiliary sources for maxwell's equations. *International Journal of Numerical Modelling: Electronic Networks, Devices and Fields*, *33*(5), e2534. https://doi.org/http://dx.doi.org/10.1002/jnm.2534

Cassidy, N. J., & Millington, T. M. (2009). The application of finite-difference time-domain modelling for the assessment of gpr in magnetically lossy materials. *Journal of Applied Geophysics*, *67*(4), 296–308. https://doi.org/https://doi.org/10.1016/j.jappgeo.2008.09.009

Chew, W. C., & Jin, J. M. (1996). Perfectly matched layers in the discretized space: An analysis and optimization. *Electromagnetics*, *16*(4), 325–340. https://doi.org/10.1080/02726349608908483

Chew, W., & Tong, M.-S. (2022). *Integral equation methods for electromagnetic and elastic waves*. Springer Nature. https://doi.org/https://doi.org/10.1007/978-3-031-01707-0

COMSOL AB. (2024). *Comsol multiphysics® reference manual*. Version 6.3. https://www.comsol.com

Courant, R., Friedrichs, K., & Lewy, H. (1928). Über die partiellen differenzengleichungen der mathematischen physik. *Mathematische annalen*, *100*(1), 32–74.

Cui, F., Dong, G., Chen, Y., Wang, C., Teng, D., & Wang, R. (2023). Numerical modeling and data signal analysis of gpr array based on dual-field domain-decomposition time-domain finite element method. *Journal of Applied Geophysics*, *208*, 104876. https://doi.org/http://dx.doi.org/10.1016/j.jappgeo.2022.104876

Cui, S., & Weile, D. S. (2002). Analysis of electromagnetic scattering from periodic structures by fem truncated by anisotropic pml boundary condition. *Microwave and Optical Technology Letters*, *35*(2), 106–110. https://doi.org/http://dx.doi.org/10.1090/S0025-5718-10-02355-0

d'Alembert, J. l. R. (1747). Recherches sur la courbe que forme une corde tendue mise en vibration.

Dassault Systèmes. (2023). *Cst studio suite®*. https://www.3ds.com/products/simulia/cst-studio-suite

David, H. S. (2009). Chapter 10: Antennas and radiation [https://ocw.mit.edu/courses/6-007-electromagnetics-and-applications-spring-2011/resources/chap-10-antennas/]. In *Electromagnetics and applications*. Massachusetts Institute of Technology.

Davidson, D. B. (2010). *Computational electromagnetics for rf and microwave engineering*. Cambridge University Press. https://doi.org/https://doi.org/10.1017/CBO9780511778117

Davidson, D. B., & Botha, M. M. (2007). Evaluation of a spherical pml for vector fem applications. *IEEE transactions on antennas and propagation*, *55*(2), 494–498. https://search.ricest.ac.ir/dl/search/defaultta.aspx?DTC=49&DC=1088204

Demkowicz, L. (2006). *Computing with hp-adaptive finite elements: Volume 1 one and two dimensional elliptic and maxwell problems*. Chapman; Hall/CRC.

Ding, S., Wang, X., Feng, D., Xu, L., Irving, J., & Holliger, K. (2025). Frequency-domain vector finite element forward modeling of 3d gpr data using exact pml absorbing boundary conditions. *Computational Geosciences*, *29*(3), 1–30. https://doi.org/http://dx.doi.org/10.1007/s10596-025-10357-7

Do Nascimento, V. C., & Jiao, D. (2024). Patch-based matrix-free time-domain method and pml-truncation in unstructured 3-d meshes. *IEEE Transactions on Antennas and Propagation*.

El Kacimi, A., Laghrouche, O., Ouazar, D., Mohamed, M. S., Seaid, M., & Trevelyan, J. (2019). Enhanced conformal perfectly matched layers for bernstein–bézier finite element modelling of short wave scattering. *Computer Methods in Applied Mechanics and Engineering*, *355*, 614–638. https://doi.org/http://dx.doi.org/10.1016/j.cma.2019.06.032

Engquist, B., & Majda, A. (1977). Absorbing boundary conditions for the numerical simulation of waves. *Mathematics of computation*, *31*(139), 629–651. https://doi.org/https://doi.org/10.1073/pnas.74.5.1765

Feng, D., Ding, S., & Wang, X. (2019). An exact pml to truncate lattices with unstructured-mesh-based adaptive finite element method in frequency domain for ground penetrating radar simulation. *Journal of Applied Geophysics*, *170*, 103836. https://doi.org/https://doi.org/10.1016/j.jappgeo.2019.103836

Feng, D., Wang, X., & Zhang, B. (2019). Improving reconstruction of tunnel lining defects from ground-penetrating radar profiles by multi-scale inversion and bi-parametric full-waveform inversion. *Advanced Engineering Informatics*, *41*, 100931. https://doi.org/https://doi.org/10.1016/j.aei.2019.100931

Feng, D., Wang, X., & Zhang, B. (2020). A frequency-domain quasi-newton-based biparameter synchronous imaging scheme for ground-penetrating radar with applications in full waveform inversion. *IEEE Transactions on Geoscience and Remote Sensing*, *59*(3), 1949–1966. https://doi.org/http://dx.doi.org/10.1109/TGRS.2020.3004465

Forte, E., & Pipan, M. (2017). Review of multi-offset gpr applications: Data acquisition, processing and analysis. *Signal Processing*, *132*, 210–220. https://doi.org/https://doi.org/10.1016/j.sigpro.2016.04.011

Galkowski, J., Lafontaine, D., Spence, E. A., & Wunsch, J. (2022). The *hp*-fem applied to the helmholtz equation with pml truncation does not suffer from the pollution effect. *arXiv preprint arXiv:2207.05542*. https://doi.org/https://doi.org/10.48550/arXiv.2207.05542

Gottlieb, S., & Ketcheson, D. (2016). Chapter 21 - time discretization techniques. In R. Abgrall & C.-W. Shu (Eds.), *Handbook of numerical methods for hyperbolic problems* (pp. 549–583, Vol. 17). Elsevier. https://doi.org/https://doi.org/10.1016/bs.hna.2016.08.001

Griffiths, D. J. (2023). *Introduction to electrodynamics*. Cambridge University Press. https://doi.org/https://doi.org/10.1017/9781108333511

Harari, I., Slavutin, M., & Turkel, E. (2000). Analytical and numerical studies of a finite element pml for the helmholtz equation. *Journal of Computational Acoustics*, *8*(01), 121–137. https://doi.org/http://dx.doi.org/10.1142/S0218396X0000008X

Heaviside, O. (1893–1912). *Electromagnetic theory, volumes 1-3*. The Electrician Printing; Publishing Company.

Hiptmair, R. (2002). Finite elements in computational electromagnetism. *Acta Numerica*, *11*, 237–339. https://doi.org/https://doi.org/10.1017/S0962492902000041

Huber, E., & Hans, G. (2018). Rgpr—an open-source package to process and visualize gpr data. *2018 17th International Conference on Ground Penetrating Radar (GPR)*, 1–4. https://doi.org/https://doi.org/10.1109/ICGPR.2018.8441658

Irving, J., & Knight, R. (2006). Numerical modeling of ground-penetrating radar in 2-d using matlab. *Computers & Geosciences*, *32*(9), 1247–1258. https://doi.org/http://dx.doi.org/10.1016/j.cageo.2005.11.006

Ji, D., Wang, Q., Chen, Z., Harding, T. G., Dong, M., Ge, C., Li, Z., & Lai, F. (2020). A property-dependent perfectly matched layer with a single additional layer for maxwell's equations in finite difference frequency domains. *Computer Methods in Applied Mechanics and Engineering*, *372*, 113355. https://doi.org/http://dx.doi.org/10.1016/j.cma.2020.113355

Jiang, X., & Duan, X. (2022). A pml finite element method for electromagnetic scattering problems in a two-layer medium. *Journal of Scientific Computing*, *90*(1), 34. https://doi.org/http://dx.doi.org/10.1137/16M1091757

Jiao, D., Jin, J.-M., Michielssen, E., & Riley, D. J. (2003). Time-domain finite-element simulation of three-dimensional scattering and radiation problems using perfectly matched layers. *IEEE transactions on antennas and propagation*, *51*(2), 296–305. https://doi.org/http://dx.doi.org/10.1109/TAP.2003.809096

Jin, J.-M. (2015). *The finite element method in electromagnetics*. John Wiley & Sons.

Jin, J.-M., & Riley, D. J. (2008). *Finite element analysis of antennas and arrays*. John Wiley & Sons.

Karperaki, A., Papathanasiou, T., & Belibassakis, K. (2019). An optimized, parameter-free pml-fem for wave scattering problems in the ocean and coastal environment. *Ocean Engineering*, *179*, 307–324. https://doi.org/https://doi.org/10.1016/j.oceaneng.2019.03.036

Lampe, B., Holliger, K., & Green, A. G. (2003). A finite-difference time-domain simulation tool for ground-penetrating radar antennas. *Geophysics*, *68*(3), 971–987. https://doi.org/https://doi.org/10.1190/1.1581069

Langer, U., Pauly, D., & Repin, S. (2019). *Maxwell's equations: Analysis and numerics* (Vol. 24). Walter de Gruyter GmbH & Co KG. https://doi.org/https://doi.org/10.1515/9783110543612-201

Lavoué, F., Brossier, R., Métivier, L., Garambois, S., & Virieux, J. (2014). Two-dimensional permittivity and conductivity imaging by full waveform inversion of multioffset gpr

data: A frequency-domain quasi-newton approach. *Geophysical Journal International*, *197*(1), 248–268. https://doi.org/https://dx.doi.org/10.1093/gji/ggt528

Ledger, P., Morgan, K., Hassan, O., & Weatherill, N. (2002). Arbitrary order edge elements for electromagnetic scattering simulations using hybrid meshes and a pml. *International Journal for Numerical Methods in Engineering*, *55*(3), 339–358. https://doi.org/https://doi.org/10.1002/nme.501

Levy, M. (2000). *Parabolic equation methods for electromagnetic wave propagation*. IET. https://doi.org/http://dx.doi.org/10.1049/PBEW045E

Liu, H., Xing, B., Wang, H., Cui, J., & Spencer, B. F. (2019). Simulation of ground penetrating radar on dispersive media by a finite element time domain algorithm. *Journal of applied geophysics*, *170*, 103821. https://doi.org/https://doi.org/10.1016/j.jappgeo.2019.103821

Lombardi, F., Podd, F., & Solla, M. (2022). From its core to the niche: Insights from gpr applications. *Remote Sensing*, *14*(13), 3033. https://doi.org/http://dx.doi.org/10.3390/rs14133033

Matuszyk, P. J., & Demkowicz, L. F. (2013). Parametric finite elements, exact sequences and perfectly matched layers. *Computational Mechanics*, *51*, 35–45. https://doi.org/https://doi.org/10.1007/s00466-012-0702-1

Maxwell, J. C. (1873). *A treatise on electricity and magnetism* (Vol. 1). Clarendon press.

Monk, P. (2003). *Finite element methods for maxwell's equations*. Oxford university press. https://doi.org/http://dx.doi.org/10.1093/acprof:oso/9780198508885.001.0001

Mulder, W. A., Wirianto, M., & Slob, E. C. (2008). Time-domain modeling of electromagnetic diffusion with a frequency-domain code. *Geophysics*, *73*(1), F1–F8. https://doi.org/https://doi.org/doi:10.1190/1.2799093

Ozgun, O., Kuzuoglu, M., & Mittra, R. (2023). Self-tuning locally conformal pml mesh truncation for 3-d vector finite element method. *IEEE Transactions on Antennas and Propagation*, *72*(2), 2036–2040. https://doi.org/http://dx.doi.org/10.1109/TAP.2023.3333929

Pekel, Ü., & Mittra, R. (1995). A finite-element-method frequency-domain application of the perfectly matched layer (pml) concept. *Microwave and optical technology letters*, *9*(3), 117–122.

Pelosi, G., Coccioli, R., & Selleri, S. (2009). *Quick finite elements for electromagnetic waves*. Artech House.

Peng, Z., Wang, X.-c., & Lee, J.-F. (2011). Integral equation based domain decomposition method for solving electromagnetic wave scattering from non-penetrable objects. *IEEE Transactions on Antennas and Propagation*, *59*(9), 3328–3338. https://doi.org/http://dx.doi.org/10.1109/TAP.2011.2161542

Pled, F., & Desceliers, C. (2022). Review and recent developments on the perfectly matched layer (pml) method for the numerical modeling and simulation of elastic wave propagation in unbounded domains. *Archives of Computational Methods in Engineering*, *29*(1), 471–518. https://doi.org/http://dx.doi.org/10.1007/s11831-021-09581-y

Polycarpou, A. C. (2022). *Introduction to the finite element method in electromagnetics*. Springer Nature. https://doi.org/https://doi.org/10.1007/978-3-031-01689-9

pulseEKKO, Sensors & Software Inc. (2023). *Pulseekko® user's guide with ultra receiver and dvl 500*. https://kdjonesinstruments.com/wp-content/uploads/sites/15/2023/03/pulseEKKO-Users-Guide-with-Ultra-Receiver-and-DVL-500.pdf

Rappaport, C. M. (1996). Interpreting and improving the pml absorbing boundary condition using anisotropic lossy mapping of space. *IEEE Transactions on Magnetics*, *32*(3), 968–974.

Ren, Z., Kalscheuer, T., Greenhalgh, S., & Maurer, H. (2013). A goal-oriented adaptive finite-element approach for plane wave 3-d electromagnetic modelling. *Geophysical Journal International*, *194*(2), 700–718. https://doi.org/http://dx.doi.org/10.1093/gji/ggt154

Rulff, P. (2023). *Three-dimensional forward modelling and inversion of controlled-source electromagnetic data using the edge-based finite-element method* [Doctoral dissertation, Acta Universitatis Upsaliensis]. https://doi.org/https://doi.org/10.1111/1365-2478.13660

Rulff, P., Buntin, L. M., & Kalscheuer, T. (2021). Efficient goal-oriented mesh refinement in 3-d finite-element modelling adapted for controlled source electromagnetic surveys. *Geophysical Journal International*, *227*(3), 1624–1645. https://doi.org/https://doi.org/10.1093/gji/ggab264

Sacks, Z. S., Kingsland, D. M., Lee, R., & Lee, J.-F. (1995). A perfectly matched anisotropic absorber for use as an absorbing boundary condition. *IEEE transactions on Antennas and Propagation*, *43*(12), 1460–1463. https://doi.org/http://dx.doi.org/10.1109/8.477075

Sadiku, M. N. (2009). *Numerical techniques in electromagnetics (3rd edition)*. CRC press. https://doi.org/https://doi.org/10.1201/9781315222622

Schnaubelt, E., De Gersem, H., & Marsic, N. (2023). Comparison of 2. 5d finite element formulations with perfectly matched layers for solving open axisymmetric electromagnetic cavity problems. *International Journal of Numerical Modelling: Electronic Networks, Devices and Fields*, *36*(3), e3073. https://doi.org/https://doi.org/10.1002/jnm.3073

Scroggs, M. W., Brubeck, P. D., Dean, J. P., Dokken, J. S., Marsden, I., Nobre, N., et al. (2025). DefElement: An encyclopedia of finite element definitions [[Online; accessed 01-August-2025]].

Selleri, S., Vincetti, L., Cucinotta, A., & Zoboli, M. (2001). Complex fem modal solver of optical waveguides with pml boundary conditions. *Optical and Quantum Electronics*, *33*, 359–371. https://doi.org/http://dx.doi.org/10.1023/A:1010886632146

Si, H., & TetGen, A. (2009). A quality tetrahedral mesh generator and a 3d delaunay triangulator. *Cited on*, *61*. https://api.semanticscholar.org/CorpusID:125677786

Silvester, P. P., & Ferrari, R. L. (1996). *Finite elements for electrical engineers*. Cambridge university press. https://doi.org/https://doi.org/10.1017/CBO9781139170611

Smull, A. P., Manić, A. B., Manić, S. B., & Notaroš, B. M. (2017). Anisotropic locally conformal perfectly matched layer for higher order curvilinear finite-element modeling. *IEEE Transactions on Antennas and Propagation*, *65*(12), 7157–7165. https://doi.org/http://dx.doi.org/10.1109/TAP.2017.2759839

Sun, S., Kooij, B. J., Jin, T., & Yarovoy, A. G. (2017). Cross-correlated contrast source inversion. *IEEE Transactions on Antennas and Propagation*, *65*(5), 2592–2603. https://doi.org/http://dx.doi.org/10.48550/arXiv.1906.10864

Šušnjara, A., Poljak, D., Šesnić, S., & Dorić, V. (2016). Time domain and frequency domain integral equation method for the analysis of ground penetrating radar (gpr) antenna. *2016 24th International Conference on Software, Telecommunications and Computer Networks (SoftCOM)*, 1–4. https://doi.org/10.1109/SOFTCOM.2016.7772184

Taflove, A. (1995). The finite difference time domain method. *Computational electromagnetics*.

Van den Berg, P. M. (2021). *Forward and inverse scattering algorithms based on contrast source integral equations*. John Wiley & Sons. https://doi.org/https://www.wiley.com/en-us/Forward+and+Inverse+Scattering+Algorithms+Based+on+Contrast+Source+Integral+Equations-p-9781119741541

Wait, J. R. (2013). *Electromagnetic waves in stratified media: Revised edition including supplemented material* (Vol. 3). Elsevier. https://doi.org/https://doi.org/10.1016/C2013-0-05239-5

Wang, X., ZHU, L., FENG, D., XU, D., DING, S., & LIU, S. (2023). Frequency domain forward modeling of gpr in dispersive media with optimal coefficient finite element method. *Chinese Journal of Geophysics*, *66*(12), 5173–5186. https://doi.org/https://doi.org/10.6038/cjg2022Q0814

Warren, C., Pajewski, L., Poljak, D., Ventura, A., Giannopoulos, A., & Sesnic, S. (2016). A comparison of finite-difference, finite-integration, and integral-equation methods in the time-domain for modelling ground penetrating radar antennas. *2016 16th International Conference on Ground Penetrating Radar (GPR)*, 1–5. https://doi.org/10.1109/ICGPR.2016.7572676

Warren, C., Giannopoulos, A., & Giannakis, I. (2016). Gprmax: Open source software to simulate electromagnetic wave propagation for ground penetrating radar. *Computer Physics Communications*, *209*, 163–170. https://doi.org/https://doi.org/10.1016/j.cpc.2016.08.020

Werthmüller, D. (2017). An open-source full 3d electromagnetic modeler for 1d vti media in python: Empymod. *Geophysics*, *82*(6), WB9–WB19. https://doi.org/https://doi.org/10.1190/geo2016-0626.1

Werthmüller, D., Key, K., & Slob, E. C. (2019). A tool for designing digital filters for the hankel and fourier transforms in potential, diffusive, and wavefield modeling. *Geophysics*, *84*(2), F47–F56. https://doi.org/https://doi.org/10.1190/GEO2018-0069.1

Wolfe, C., Navsariwala, U., & Gedney, S. D. (2000). A parallel finite-element tearing and interconnecting algorithm for solution of the vector wave equation with pml absorbing medium. *IEEE Transactions on Antennas and Propagation*, *48*(2), 278–284. https://doi.org/http://dx.doi.org/10.1109/8.833077

Wu, J.-Y., Kingsland, D. M., Lee, J.-F., & Lee, R. (1997). A comparison of anisotropic pml to berenger's pml and its application to the finite-element method for em scattering. *IEEE Transactions on Antennas and Propagation*, *45*(1), 40–50. https://doi.org/http://dx.doi.org/10.1109/8.554239

Xue, S., Yin, C., Li, J., Zhu, J., & Liu, W. (2025). A high efficiency discontinuous galerkin method for 3d ground-penetrating radar simulation. *Remote Sensing*, *17*(2), 228. https://doi.org/https://doi.org/10.3390/rs17020228

Zarei, S., Oskooi, B., Amini, N., & Dalkhani, A. R. (2016). 2d spectral element modeling of gpr wave propagation in inhomogeneous media. *Journal of Applied Geophysics*, *133*, 92–97. https://doi.org/https://doi.org/10.1016/j.jappgeo.2016.07.027

Zhang, R., Sun, Q., Zhuang, M., Huang, W.-F., Zhan, Q., Wang, D., & Liu, Q. H. (2018). Optimization of the periodic pml for sem. *IEEE Transactions on Electromagnetic Compatibility*, *61*(5), 1578–1585. https://doi.org/https://doi.org/10.1109/TEMC.2018.2866441

Zhdanov, M. S. (2009). *Geophysical electromagnetic theory and methods* (Vol. 43). Elsevier. https://doi.org/https://doi.org/10.1016/S0076-6895(09)70001-0

Appendix A

Attempted Implementation of the CS-PML

To attempt implementation of the CS-PML, I derived the altered stiffness and mass matrices of `elfe3D_GPR` that apply in the PML region only, considering the choice of first-order Nédélec basis functions.

I used the works from (Jin, 2015; Jin & Riley, 2008; Ozgun et al., 2023) to derive the changes I need to implement for this. From (Jin & Riley, 2008), the coordinate stretching manifests as a change in the differential operator ∇ to $\tilde{\nabla}$, where $\tilde{\nabla}$ is defined as:

$$\tilde{\nabla} = \frac{1}{s_x}\frac{\partial}{\partial x}\hat{x} + \frac{1}{s_y}\frac{\partial}{\partial y}\hat{y} + \frac{1}{s_z}\frac{\partial}{\partial z}\hat{z}. \tag{A-1}$$

Here, $s_i \; \forall \; i \in \{x, y, z\}$ are stretching factors in the direction of the respective coordinate axis. These are defined by the expression:

$$s_i = 1 - j\frac{\gamma(i)}{\omega\varepsilon} \quad i = x, y, z; \quad \gamma(i) > 0 \tag{A-2}$$

where $\gamma(i)$ defines the amount of stretch, ω is the angular frequency of simulation, and ε here is the permittivity of the background medium. This form is specifically chosen to ensure:

1. The imaginary component of s_i is always negative, which ensures for the $e^{+j\omega t}$ convention that the wave is attenuated in the PML region (Jin & Riley, 2008).
2. The scaling by $\omega\varepsilon$ ensures that the decay factor (not the stretching function) is frequency independent.

It is to be noted that I was implementing this version of PML before considering the changed PDE Equation (3-11). This PML was designed to work with the original PDE in Equation (3-4a).

To define $\gamma(i)$, I used a modification of the formulation from (Ozgun et al., 2023). Their original formulation is designed for a spherical PML in non-geological context. Their stretched coordinates looks like:

$$\tilde{\mathbf{r}} = \mathbf{r} - j\frac{\gamma(\delta)}{k}\hat{\mathbf{n}}(\delta), \tag{A-3}$$

where $\mathbf{r}$ is the original position vector of any node in the mesh, $\tilde{\mathbf{r}}$ is the new position vector that is stretched, k is the complex wavenumber, $\gamma(\delta)$ is the decay function they choose, equivalent to $\gamma(i)$ in the previous interpretation except $\gamma(\delta)$ applies to spherical coordinates, and $\hat{\mathbf{n}}$ is the unit normal vector to the boundary. $\gamma(\delta)$ is defined as:

$$\gamma(\delta) = -\log(1-\delta), \tag{A-4}$$

$$\delta = \frac{||\mathbf{r} - \mathbf{r_{in}}||}{||\mathbf{r_{out}} - \mathbf{r_{in}}||}, \tag{A-5}$$

where $\mathbf{r_{in}}$ and $\mathbf{r_{out}}$ are the position vectors to the inner and outer boundaries of the PML region from origin, respectively. The position factor δ has a range of $[0, 1]$; zero at the inner PML boundary and one at the outer PML boundary. This ensures that the stretching $\gamma(\delta)$ is maximum at the outer PML boundary, tending to $+\infty$ and minimum at the inner PML boundary starting from zero. Doing this ensures matching the impedance at the inner PML boundary to the medium. Due to $\gamma(\delta)$ having a range of $[0, +\infty)$ in any given thickness of the PML, it corresponds to an Exact PML, with continuously varying attenuation for the PML region effectively acting as a perfect absorber effectively simulating an infinitely large medium.

For my application of this stretching function in a PML built using a combination of rectangular prisms surrounding the face, edges and corners, Figure 4-3, I have to account for where each finite element in the mesh is located in the PML region. This is to provide correct direction vector to the decay of outgoing waves perpendicular to the plane of PML.

For evaluating the stretching function $\gamma(\delta)$, I evaluate it axis-wise based on which of the 3 coordinate axes apply. For each coordinate axis $i \in \{x, y, z\}$, I define the following:

1. r_i: The value of the coordinate of the midpoint of each edge in the PML region, along the relevant axis, as per edge-based FEM DOFs.
2. $r_{in,i}$: The value of the coordinate of the inner boundary of the PML region, along the relevant axis.
3. $r_{out,i}$: The value of the coordinate of the outer boundary of the PML region, along the relevant axis.
4. $||r_{out,i} - r_{in,i}||$ evaluates to the thickness of the PML region for each axis.

This ensures that each coordinate axis is evaluated independently, and the stretching function $\gamma(\delta)$ reduces to $\gamma(i)$ for each axis, since (Jin & Riley, 2008) says the stretching function applied in one coordinate axis is independent of the other axes.

Once I evaluate $\gamma(i)$, I can evaluate the stretching factor s_i for each axis using the equation Equation (A-2). The stretching factor is then used to modify the differential operator ∇ to

∇_s as defined in Equation (A-1). This converts the original finite element stiffness and mass matrices Equations (3-20a) and (3-20b) to:

$$\tilde{K}^e_{lj} = \iiint_{V_e} \frac{1}{\mu_e} (\tilde{\nabla} \times \mathbf{N}^e_l) \cdot (\tilde{\nabla} \times \mathbf{N}^e_j) d\tilde{V} \tag{A-6}$$

$$\tilde{M}^e_{lj} = \iiint_{V_e} \mathbf{N}^e_l \cdot \mathbf{N}^e_j d\tilde{V} \tag{A-7}$$

where $\mathbf{N}^e_l$ and $\mathbf{N}^e_j$ are the shape functions for the lth and jth edges of the element, respectively, and V_e is the volume of the element.

Since `elfe3D`'s implementation of the basis functions and differential operators is based on (Jin, 2015), I refer to them to derive the stretched stiffness and mass matrices. From the stretched local matrices Equation (A-6), it is evident that I need to evaluate the following terms for the PML region differently:

1. $(\tilde{\nabla} \times \mathbf{N}^e_l) \cdot (\tilde{\nabla} \times \mathbf{N}^e_j)$
2. $d\tilde{V}$

Using the definition of Nedelec basis functions Equation (3-18) the differential operator $\tilde{\nabla}$ as defined in Equation (A-1), I get its stretched-curl as follows:

$$\tilde{\nabla} \times \mathbf{N}^e_l = \begin{vmatrix} \hat{x} & \hat{y} & \hat{z} \\ \frac{1}{s_{x_l}} \frac{\partial}{\partial x} & \frac{1}{s_{y_l}} \frac{\partial}{\partial y} & \frac{1}{s_{z_l}} \frac{\partial}{\partial z} \\ \left(L^e_{i_1} \frac{\partial}{\partial x} L^e_{i_2} - L^e_{i_2} \frac{\partial}{\partial x} L^e_{i_1} \right) l^e_i & \left(L^e_{i_1} \frac{\partial}{\partial y} L^e_{i_2} - L^e_{i_2} \frac{\partial}{\partial y} L^e_{i_1} \right) l^e_i & \left(L^e_{i_1} \frac{\partial}{\partial z} L^e_{i_2} - L^e_{i_2} \frac{\partial}{\partial z} L^e_{i_1} \right) l^e_i \end{vmatrix} \tag{A-8}$$

Upon evaluating the determinant for the stretched-curl, I get, for component $\hat{x}$:

$$(\tilde{\nabla} \times \mathbf{N}^e_l) \cdot \hat{x} = \frac{1}{s_{y_l}} \frac{\partial}{\partial y} \left(\left(L^e_{i_1} \frac{\partial}{\partial z} L^e_{i_2} - L^e_{i_2} \frac{\partial}{\partial z} L^e_{i_1} \right) l^e_i \right) - \frac{1}{s_{z_l}} \frac{\partial}{\partial z} \left(\left(L^e_{i_1} \frac{\partial}{\partial y} L^e_{i_2} - L^e_{i_2} \frac{\partial}{\partial y} L^e_{i_1} \right) l^e_i \right) \tag{A-9}$$

Applying the product rule, all mixed second derivative terms are zero since both L^e are linear, leaving only the cross products of their first derivatives:

$$(\tilde{\nabla} \times \mathbf{N}^e_l) \cdot \hat{x} = \frac{1}{s_{y_l}} \left(\frac{\partial L^e_{i_1}}{\partial y} \frac{\partial L^e_{i_2}}{\partial z} - \frac{\partial L^e_{i_2}}{\partial y} \frac{\partial L^e_{i_1}}{\partial z} \right) l^e_i - \frac{1}{s_{z_l}} \left(\frac{\partial L^e_{i_1}}{\partial z} \frac{\partial L^e_{i_2}}{\partial y} - \frac{\partial L^e_{i_2}}{\partial z} \frac{\partial L^e_{i_1}}{\partial y} \right) l^e_i \tag{A-10}$$

Rearranging per the same differential terms, I get:

$$(\tilde{\nabla} \times \mathbf{N}^e_l) \cdot \hat{x} = \left(\frac{1}{s_{y_l}} + \frac{1}{s_{z_l}} \right) \frac{\partial L^e_{i_1}}{\partial y} \frac{\partial L^e_{i_2}}{\partial z} l^e_i - \left(\frac{1}{s_{y_l}} + \frac{1}{s_{z_l}} \right) \frac{\partial L^e_{i_2}}{\partial y} \frac{\partial L^e_{i_1}}{\partial z} l^e_i \tag{A-11}$$

or,

$$(\tilde{\nabla} \times \mathbf{N}^e_l) \cdot \hat{x} = \left(\frac{1}{s_{y_l}} + \frac{1}{s_{z_l}} \right) \left(\frac{\partial L^e_{i_1}}{\partial y} \frac{\partial L^e_{i_2}}{\partial z} - \frac{\partial L^e_{i_2}}{\partial y} \frac{\partial L^e_{i_1}}{\partial z} \right) l^e_i \tag{A-12}$$

If the stretching functions were not to be applied, in the normal simulation domain, the x component of the original curl would have been:

$$(\nabla \times \mathbf{N}_l^e) \cdot \hat{x} = 2 \left(\frac{\partial L_{i_1}^e}{\partial y} \frac{\partial L_{i_2}^e}{\partial z} - \frac{\partial L_{i_2}^e}{\partial y} \frac{\partial L_{i_1}^e}{\partial z} \right) l_i^e \tag{A-13}$$

Hence, it is apparent that the application of the stretching functions in the PML region applies a scaling of the factor of $\frac{1}{2}\left(\frac{1}{s_{y_l}} + \frac{1}{s_{z_l}}\right)$ to the original curl.

Using this now to determine the the dot product $(\tilde{\nabla} \times \mathbf{N}_l^e) \cdot (\tilde{\nabla} \times \mathbf{N}_j^e)$ is straightforward. From the $\hat{x}$ component of both $(\tilde{\nabla} \times \mathbf{N}_l^e)$ and $(\tilde{\nabla} \times \mathbf{N}_j^e)$, I get the first term of the dot product as:

$$\left(\left(\frac{1}{s_{y_l}} + \frac{1}{s_{z_l}} \right) \left(\frac{\partial L_{i_1}^e}{\partial y} \frac{\partial L_{i_2}^e}{\partial z} - \frac{\partial L_{i_2}^e}{\partial y} \frac{\partial L_{i_1}^e}{\partial z} \right) l_i^e \right) \cdot \left(\left(\frac{1}{s_{y_j}} + \frac{1}{s_{z_j}} \right) \left(\frac{\partial L_{j_1}^e}{\partial y} \frac{\partial L_{j_2}^e}{\partial z} - \frac{\partial L_{j_2}^e}{\partial y} \frac{\partial L_{j_1}^e}{\partial z} \right) l_j^e \right) \tag{A-14}$$

Hence, the first term of the dot product is re-written as:

$$\left(\frac{1}{s_{y_l}} + \frac{1}{s_{z_l}} \right) \left(\frac{1}{s_{y_j}} + \frac{1}{s_{z_j}} \right) \left(\frac{\partial L_{i_1}^e}{\partial y} \frac{\partial L_{i_2}^e}{\partial z} - \frac{\partial L_{i_2}^e}{\partial y} \frac{\partial L_{i_1}^e}{\partial z} \right) \left(\frac{\partial L_{j_1}^e}{\partial y} \frac{\partial L_{j_2}^e}{\partial z} - \frac{\partial L_{j_2}^e}{\partial y} \frac{\partial L_{j_1}^e}{\partial z} \right) l_j^e l_i^e \tag{A-15}$$

This essentially means that for the $\hat{x}$ component of the stiffness matrix, I have to multiply the following term to the original stiffness matrix expression:

$$\frac{1}{4} \left(\frac{1}{s_{y_l}} + \frac{1}{s_{z_l}} \right) \left(\frac{1}{s_{y_j}} + \frac{1}{s_{z_j}} \right) \tag{A-16}$$

For the other two components, similar process is applied. Hence, the stretched stiffness matrix would look like:

$$\tilde{K}_{lj}^e = \frac{1}{4} \left(\frac{1}{s_{y_l}} + \frac{1}{s_{z_l}} \right) \left(\frac{1}{s_{y_j}} + \frac{1}{s_{z_j}} \right) K_{x,lj}^e \tag{A-17}$$

$$+ \frac{1}{4} \left(\frac{1}{s_{x_l}} + \frac{1}{s_{z_l}} \right) \left(\frac{1}{s_{x_j}} + \frac{1}{s_{z_j}} \right) K_{y,lj}^e \tag{A-18}$$

$$+ \frac{1}{4} \left(\frac{1}{s_{x_l}} + \frac{1}{s_{y_l}} \right) \left(\frac{1}{s_{x_j}} + \frac{1}{s_{y_j}} \right) K_{z,lj}^e \tag{A-19}$$

The $K_{x,lj}^e$, $K_{y,lj}^e$, and $K_{z,lj}^e$ are the original stiffness matrix terms for the $\hat{x}$, $\hat{y}$, and $\hat{z}$ components of the stiffness matrix from (Jin, 2015).

To evaluate the $d\tilde{V}$ term, I evaluate the stretching factors at the centroid of each element in the PML region. Since dV is defined as $dxdydz$, the stretch makes it $d\tilde{x}d\tilde{y}d\tilde{z}$, where $d\tilde{x} = s_x dx$, $d\tilde{y} = s_y dy$, and $d\tilde{z} = s_z dz$.